Long Distance Entanglement Distribution

Stuart Graham Broadfoot

St. John's College, Oxford

Thesis submitted in fulfilment of the requirements for the degree of Doctor of Philosophy

Trinity Term, 2012

Atomic and Laser Physics,

University of Oxford

Long Distance Entanglement Distribution

Stuart Graham Broadfoot, St. John's College, Oxford

Trinity Term, 2012

DPhil Abstract

Developments in the interdisciplinary field of quantum information open up previously impossible abilities in the realms of information processing and communication. Quantum entanglement has emerged as one property of quantum systems that acts as a resource for quantum information processing and, in particular, enables teleportation and secure cryptography. Therefore, the creation of entangled resources is of key importance for the application of these technologies. Despite a great deal of research the efficient creation of entanglement over long distances is limited by inevitable noise. This problem can be overcome by creating entanglement between nodes in a network and then performing operations to distribute the entanglement over a long distance.

This thesis contributes to the field of entanglement distribution within such quantum networks. Entanglement distribution has been extensively studied for one-dimensional networks resulting in "quantum repeater" protocols. However, little work has been done on higher dimensional networks. In these networks a fundamentally different scaling, called "long distance entanglement distribution", can appear between the resources and the distance separating the systems to be entangled. I reveal protocols that enable long distance entanglement distribution for quantum networks composed of mixed state and give a few limitations to the capabilities of entanglement distribution.

To aid in the implementation of all entanglement distribution protocols I finish by introducing a new system, composed of an optical nanofibre coupled to a carbon nanotube, that may enable new forms of photo-detectors and quantum memories.

Contents

List of Figures

Chapter 1

Introduction

The aim of this introductory chapter is to highlight the problem of entanglement distribution and how a satisfactory solution to this problem is key to a variety of important future technologies. Various approaches have been taken to solving this problem in different contexts. Previous results that inspired this work are surveyed to put this thesis in context and I outline the structure of the thesis.

Any scientific breakthrough, that challenges our view of the world, will always be greeted by questions regarding its validity. No modern theory challenges our everyday view of reality more than quantum theory. Today, this theory has revolutionized our daily lives and yet even many of its creators believed it to be incomplete. The most famous example of this belief is given by the Einstein-Podolsky-Rosen paradox [1]. This paradox had inadvertently outlined a "spooky" action at a distance that we now know as "entanglement" [2]. This property comes about from the superposition of compound systems, allowing nonclassical correlations, and forces a holistic description of nature. Despite the scepticism, John Bell introduced his famous statistical inequality [3] that, ignoring a few possible experimental loop-holes, has validated the existence of these nonclassical correlations experimentally [4, 5, 6, 7, 8]. Greenberger, Horne and Zeilinger later went beyond these statistical correlations and showed that nonstatistical predictions can be influenced by quantum entanglement [9, 10].

It was clear that the existence of quantum entanglement had great implications on our world view and yet it was only considered a curiosity. This radically changed when it was realized that these nonclassical correlations can be used for a collection of quantum communication applications, including quantum teleportation [11], distributed quantum computing [11, 12] and dense coding [13]. Quantum teleportation actually allows an entangled state to act as a distribution channel to transport a quantum state between locations. Hence, teleportation can be used as the channels in perfectly secure quantum key distribution [14, 15] and later quantum crytography protcols were found that require initial entangled states [16]. Together with advances in quantum computing these finding have helped to form the interdisciplinary field of quantum information processing [17].

Unfortunately, quantum entanglement is a complex property and is still not fully understood. For a thorough review please see Ref. [18]. Various attempts have been made to quantify it with limited success. For two-qubit pure states it is well understood and a collection of entanglement measures have been devised for mixed states. As a resource it is now known that it can be manipulated and aid with various tasks including frequency standard improvement [19, 20] and reducing classical communication complexity [21, 22]. The general role of entanglement in quantum computation is unknown [23], although it clearly plays a necessary role in measurement-based quantum computing [24, 25, 26, 27, 28]

An interaction is required for the initial creation of entangled states. This is mediated by a Hamiltonian acting on a system. Once created the entangled systems can be separated. This can be achieved by having a Hamiltonian interaction acting on a network of subsystems to transport a part of the entangled state. For various spin networks quantum transport has been thoroughly studied to reveal conditions on the Hamiltonian for perfect state transport [29]. For small systems this method of engineering a Hamiltonian may be suitable but for quantum cryptography appli-

cations other methods are required.

To take advantage of quantum information processing it is of fundamental importance to find means to create and distribute entanglement over long distances. The most direct approach to entanglement distribution is to allow parts of the entangled state to move to the required locations. This direct "transmission" of entangled states is best accomplished via entangled photons due to their tolerance to decoherence, speed and the state of optical technologies. The downside to this tolerance is the difficulty in performing two qubit photonic quantum processing. Typically such processing is achieved with nonlinear Kerr interactions and these are weak and generally accompanied by absorption. With photonic qubits a great deal of progress has been made in using transmission for entanglement distribution over limited distances [30, 31]. In free-space transmission between two of the Canary Islands has created entanglement over a distance of 144km [32]. Applications of quantum key distribution, that make use of direct transmission, are already commercially available. Examples of this include uses of quantum cryptography for protecting ballots in Geneva during parliamentary elections (2007), connecting numerous locations around Vienna with entangled states [33] and in Tokyo [34]. All of these only transmit quantum systems between pairs of locations and many do not involve entangled states. However, entanglement is crucial to extending these schemes. Proposals are now being made to test the possibility of creating entanglement between ground and satellite stations [35, 36, 37]. These high quality entangled states are of great importance in the construction of quantum networks, where entangled states are created between pairs of nodes in a network. However, the generation of these entangled states faces a severe obstacle. Quantum channels such as free-space transmission or optical fibres are prone to loss and decoherence. This causes the desired maximally entangled states to degrade into mixtures and limits the distance over which the quantum information can be sent directly. For quantum key distribution the nodes

can act classically to create a key over an extended distance but this compromises security. Other methods must be found to enable quantum information processing over these extended distances.

In order to reduce the effect of decoherence for quantum information processing quantum error correcting codes were developed [38, 39, 40, 41]. Unlike classical information, quantum information can not be cloned, but extra redundancy can still be included in the Hilbert space allowing errors to be corrected. This principle can be applied to allow part of an entangled state to be sent with the extra redundancy to correct for the effect of decoherence. The extra redundancy here needs more channels or, with teleportation, entangled states to be initially created. These extra resources are used to send a quantum state and correct for errors. A related procedure "purifies" a number of entangled states into fewer states with higher concentrated entanglement using local operations and classical communication. These methods are called either "purification" or "distillation", with the latter usually used to refer to concentrating the entanglement in pure states [42, 43].

The purification and error-correction procedures can only purify entangled states if the initial states have a certain level of entanglement. This means that even with the aid of these procedures the distance over which entanglement can be generated is limited. The solution to this problem is to split the distance up and connect these states to form one state over the entire distance. A scheme, called entanglement "swapping" [44, 45, 46], accomplishes this connection task and results in entanglement between systems that had never directly interacted. I begin my thesis in chapter 2 by giving a summary of entanglement and the operations that can be performed to manipulate it. Quantum networks will then be introduced together with examples of these networks.

By using purification and swapping, methods began to emerge to the problem of entanglement distribution. These methods are for a one-dimensional array of

locations between which initial entanglement is created between neighbouring locations via transmission. The goal is to generate a highly entangled state between two distant locations and typically one uses the state's fidelity, *i. e.* overlap with a maximally entangled state, as a measure of success in achieving this. Such methods are collectively called "quantum repeaters" [47, 48]. Many such procedures have now been developed on these one-dimensional networks [49, 50, 51, 52, 53]. The building blocks of such repeaters have also been experimentally verified. In chapter 3 I will briefly review the current state of entanglement distribution using these methods. To date no procedure has experimentally outperformed direct transmission. The difficulty in performing effective purification and swapping operations currently limit their application.

Although one dimensional network structures have been extensively studied there has been relatively little research into the problem of entanglement distribution in higher-dimensional networks. There have been a few fascinating applications of embedding one-dimensional entanglement distribution in complex networks. However, most of the work has considered the theoretical limits to the capacity of a network when huge numbers of resources are available and quantum interactions can be performed between multiple qubits without any errors. The study in this direction is known as "assisted entanglement" [54]. A related field is that of "localisable entanglement" [55, 56] but here the focus is on spin systems and the operations allowed are usually restricted such that classical communication is excluded.

In 2007 Acín et al discovered that a fundamentally different scaling of required local resources can be obtained in higher-dimensional quantum networks [57]. An entangled state could be distributed over an arbitrary distance with the number of local resources fixed [57, 58, 59, 60, 61, 62]. I refer to this as "long distance entanglement distribution". Acín's procedure made use of the threshold phenomenon known as percolation and is now called classical entanglement percolation. Results

from mathematical percolation have actually revealed themselves to be important in other areas of quantum information processing. These include the generation of cluster states [62] and calculating entanglement thresholds for universal quantum computation with cluster states [63]. Classical entanglement percolation revealed that the extra connectivity of networks could be employed for entanglement distribution. Unfortunately, all of these higher-dimensional procedures had only been demonstrated for networks composed of pure states.

In chapter 4, I look at some fundamental restrictions on entanglement distribution within an arbitrary network. These general restrictions can then be taken into account when considering protocols.

In chapter 5 I study the application of entanglement percolation to mixed states and demonstrate that long distance entanglement distribution can be accomplished. Chapter 6 follows by introducing a different method I generalized from Ref. [64], that also allows long distance entanglement distribution with mixed states. By combining the methods I have found a scheme that works with a greater variety of states. These percolation procedures have previously been shown not to be optimal. I show in chapter 7 that this is also the case for my mixed state protocols.

The physical implementations of all quantum distribution schemes still pose various problems. The main difficulty comes from the mapping of flying photonic states to quantum states that can be processed. To aid in possible future implementation I introduce a completely new system in chapter 8.

Finally, I conclude with an overview of my findings and the recent work of others that has contributed to the field. I also highlight promising topics for further research. The bulk of this work has been previously published in the four papers [65, 66, 67, 68].

Chapter 2

Quantum Entanglement and its Manipulation

In this introductory chapter I present my notation and network descriptions. I begin by giving a short introduction to entanglement and some manipulations that can be performed using entangled resources. These methods demonstrate entanglement distribution on the simplest quantum networks. The chapter concludes by presenting various quantum network structures and their network properties.

2.1 An Introduction to Quantum Entanglement

Since the development of quantum physics it has been revealed that quantum systems can accomplish tasks that are impossible classically. A great deal of research has attempted to find the key differences that enable these abilities in quantum systems. Unfortunately, these are complicated systems and a variety of properties have emerged from quantum information theory as important. Included in these properties are quantum discord [69, 70], nonlocality [71] and primarily quantum entanglement. A complete understanding of these properties is still lacking, yet quantum entanglement has been found to be a sufficient resource for many quantum information processing tasks. Here I will introduce some basic concepts and proce-

dures to manipulate entanglement. Entanglement and nonlocality are both closely linked and indeed many of the applications of entanglement follow from its nonlocal properties. I refer to systems that can interact as local to each other and allow quantum operations to be performed on local systems. These form distinct "locations" that are sets of local systems. If classical communication is allowed between every system the set of allowed operations are classified as being local operations with classical communication (LOCC). Once restricted to LOCC the total entanglement between nonlocal systems cannot increase. This monotonic property is actually key to quantifying entanglement using "entanglement monotones" [72]. However, local operations can manipulate entanglement to generate entanglement between systems that are not local to each other. The initial short range entanglement becomes our resource.

Quantum entanglement comes about, in compound systems, because quantum mechanics describes these systems in a completely different manner to classical physics. Instead of using a classical configuration space we must describe the system in a Hilbert space. The state can then be in a superposition. This superposition is not described by its individual elements and forces us into a holistic approach. When we can not construct a pure state as a tensor product of its individual elements the state is formally defined to be entangled. For mixed states an entangled state can not be written as a convex combination of product states, *i. e.*

$$\rho \neq \sum p_i \rho_1^i \otimes ... \otimes \rho_n^i, \tag{2.1}$$

where ρ_k^i are density matrix descriptions of the individual systems. Both of these definitions are then merely forms of the negative statement that any state that is not separable is entangled. This definition, although simple, is extremely hard to test generally and doing so is called the separability problem. A recent proposal states

that entanglement can be defined as states that can not be simulated using classical-correlations [73]. The simplest compound system to consider involves a bipartite system. This can be further simplified by choosing the individual systems to be two dimensional qubits. Key examples of such entangled states are the maximally entangled Bell states, that are described by

$$\left|\,\Phi^{\pm}\right\rangle = (|\,00\rangle \pm |\,11\rangle)/\sqrt{2}, \tag{2.2}$$

$$\left|\,\Psi^{\pm}\right\rangle = (|\,01\rangle \pm |\,10\rangle)/\sqrt{2}. \tag{2.3}$$

The state $|\,\Psi^{-}\rangle$ is a "spin singlet". Since local operations can transform any Bell state into any other I will use "singlet" to briefly refer to a known maximally entangled two-qubit state. Using similar entangled states, of position and momenta, Einstein, Podolsky and Rosen argued that Quantum Theory gives an incomplete description of reality [1]. Bell later started with this as a working hypothesis leading him to demonstrate that a local hidden variable theory must impose conditions on statistical measurement correlations, that would not be satisfied by quantum theory [3]. These conditions, called Bell inequalities, have now been experimentally studied [4, 5, 6, 7, 8] and, ignoring possible loop-holes, disallow local theories. Later Greenberger, Horne and Zeilinger introduced a nonstatistical contradiction between local hidden variable theories and quantum theory [9]. This introduced the multipartite GHZ state that I will use later and is defined in an n qubit system as

$$|\,GHZ_n\rangle = (|\,0\rangle_1 \ldots |\,0\rangle_n + |\,1\rangle_1 \ldots |\,1\rangle_n)/\sqrt{2}. \tag{2.4}$$

The Bell states are idealized maximally entangled bipartite states and $|\,\Phi^{+}\rangle$ is equivalent to $|\,GHZ_2\rangle$. Using the Schmidt-decomposition every pure two-qubit state can

be expressed, upto local unitaries, in the form

$$|\,\alpha\rangle = \sqrt{\alpha}\,|\,00\rangle + \sqrt{1-\alpha}\,|\,11\rangle\,. \tag{2.5}$$

Hence, this expression contains all the information required to quantify the amount of entanglement present with the parameter $0 \leq \alpha \leq 1$. These simple states will be the main pure state network building blocks that I will consider. The entanglement present in these pure states is very well understood and can be quantified by using the bipartite pure state entanglement measure, $E(|\,\alpha\rangle) = H(\alpha)$, with $H(x) = -x\log_2 x - (1-x)\log_2(1-x)$ the Shannon binary entropy [17]. For a thorough description of possible manipulations using these states, majorization relations, that I discuss in Sec. 2.3, can be used. The quantification of entanglement in pure multipartite states still lacks a thorough understanding although some progress has been made [74, 75, 76, 77, 78].

The simplest means of generating entanglement is via a short range physical interaction or at the creation of the states. However, due to the extreme fragility of the quantum state, the environment quickly interacts with the system resulting in decoherence, a loss of any superposition and destruction of the entanglement. Once the state becomes separable it is useless as an entanglement resource and this places a limit of how far the entangled particles can be separated by direct transmission. With decoherence the state becomes mixed and must be described using a density matrix, ρ. For these mixed states the generalization of the Shannon entropy is the Von Neumann entropy, $S(\rho) = -tr(\rho\log_2\rho)$. Using local operations it is always possible to apply a "twirl" operation [42, 79] on a state to transform it into a "Werner" state [80] of the form

$$\rho_W(\lambda) = \lambda\left|\,\Phi^+\right\rangle\left\langle\Phi^+\,\right| + (1-\lambda)I/4, \tag{2.6}$$

where $0 \leq \lambda \leq 1$ and I is the identity operator. Hence, all mixed states can be assumed to be Werner states. The twirling operation removes local distinguishability from the state restricting the local manipulations that can be performed but it is still a useful simplification. A variety of different entanglement measures have been developed for mixed states [72], based on its inability to increase under LOCC, but these measures do not give a common ordering of the states. Out of these measures I will primarily mention the concurrence [81] and distillable entanglement, that I will describe later in Sec. 2.3. To measure how close a state, ρ, is to a maximally entangled state, $|\psi\rangle$, I will use the fidelity, $F = \langle\psi|\rho|\psi\rangle$. Once the state becomes separable we have exhausted all entanglement present and can no longer gain by its presence.

2.2 Quantum Error Correction

Quantum devices are far more vulnerable to errors than classical devices. Unlike errors on classical bits there is a continuous range of errors that can occur on quantum qubits and these errors have greater variety. Classical devices are also free to measure data and copy it. This is not possible on quantum qubits. The discovery of quantum error correction and fault-tolerant computing have remarkably overcome these difficulties [82, 83, 40, 84, 85]. It is actually sufficient to protect the quantum information from a discrete set of errors. If each of these can be corrected the system can correct all logical errors. These errors acting on n qubits can be described by an operator $E_{\underline{\alpha}}$ which is a Pauli operator and is given by

$$E_{\underline{\alpha}} = \bigotimes_{1 \leq i \leq n} \sigma_{\alpha_i} \tag{2.7}$$

here $\alpha_i \in I, X, Y, Z$. $X = \sigma_X$,$Y = \sigma_Y$ and $Z = \sigma_Z$ are the Pauli matrices. We define the weight of a Pauli operator, $w(\underline{\alpha})$, as the number of $\alpha_i \neq I$. These operators are all members of the Pauli Group which is defined as

$$G_n = \{ \bigotimes_{1 \leq i \leq n} O_i : O_i \in \{\pm I, \pm X, \pm Y, \pm Z, \pm \mathrm{i} I, \pm \mathrm{i} X, \pm \mathrm{i} Y, \pm \mathrm{i} Z\}\} \tag{2.8}$$

By embedding the original state $|\,\psi\rangle \in H$, in a space of dimension 2^k, into a space of dimension 2^n redundancy is added that allows errors to be detected and corrected. These embedded states are the error-correcting code χ and they have the set of orthonormal basis vectors $\{|\,i\rangle\}$. An error $E_{\underline{\alpha}} \in \varepsilon$, from a set of possibilities ε, could then occur on the state. These errors can be detected. If the minimum weight of the operators in ε is $d-1$ the code can detect $d-1$ errors and when errors with weight smaller than $(d-1)/2$ occur they can be corrected. The code is described as a $[[n, k, d]]$ code and d is called the code's distance.

A variety of different classes of error correcting codes have been considered. One class is referred to as the Stabilizer codes. These codes are formed by an Abelian subgroup $S \subset G_n$ called the stabilizer. The stabilizer code is then the subspace χ_S spanned by the $+1$ eigenvalue eigenstates of all $M \in S$. S has generators M_i which can be combined to form all elements of S and are all independent. If there are $n-k$ generators then the dimension is $\dim(\chi_S) = 2^k$. The M_i act as measurements that can detect errors $E_{\underline{\alpha}}$ that anti-commute with them.

A special type of stabilizer code are topological stabilizer codes. The logical qubit errors in these codes, that cannot be detected by measuring the syndrome, have a nontrivial topological nature. They are also characterised by having highly local stabilizers. Here highly local means that the operators forming a stabilizer only need to act between a qubit and its nearest neighbours. The most well known and basic example is the toric code [86, 87, 88].

2.3 Entanglement Purification

Quantum error correction uses extra communication channels to reduce the noise present on the data. This use of extra resources is key to entanglement distribution and further exemplified by the process of entanglement purification. The purification process shares multiple partially entangled states between distant locations instead of settling with one partially entangled state (see Fig. 2.1). This extra entanglement can then be used to provide information on the noise effecting one of the states. Once this is done we can use the knowledge to enhance one of the remaining entangled states, leaving it highly entangled. By using local operations a collection of partially entangled states can be distilled into one highly entangled state, that can now be useful for applications. This enables us to create useful entanglement over a greater distance. There are a variety of methods to accomplish the purification. Please see Ref. [89] for a review of entanglement purification. When the parties are only allowed to communicate in one direction it has been shown that there is a direct relationship between purification and error correction. It is possible to construct purification procedures from error correcting codes [90]. When classical information can be transmitted in both directions this relationship no longer exists and the added communication enables purification to perform better than error correction procedures. The two way communication procedures can be split into various categories. "recurrent" schemes perform the purification on pairs of states. This is in contrast to "M to N" schemes which allow M initial states to be distilled into N final states. For some states it is also possible to enhance the entanglement of an individual state probabilistically using a "filtering" operation. The effectiveness of each method is measured by its "yield". This yield measures the ratio of final perfect singlet states to the number of initial states, in the limit of having an infinite number. The optimal yield is the distillable entanglement but

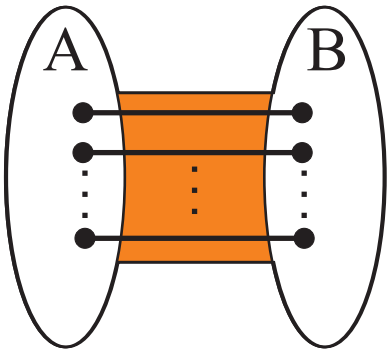

Figure 2.1: A series of n two-qubit entangled states split between two locations, A and B. The entangled states are represented by edges (black lines) and are composed of qubits (black circles). Each node is represented by an open circle. The edges form a bond (orange line). Purification acts on this system to obtain fewer states with concentrated entanglement.

this is only known in a few specific cases. I will show in chapter 4 that, with a finite number of initial states, it is impossible to generate perfect singlets unless the states are of a very specific form. I will start by introducing purification in the case of having pure states. For these bipartite pure states the possible manipulations are completely understood and there is only one precise entanglement measure. All of the possible manipulations are given by the remarkable majorization results found by Nielsen and Vidal [91]. Since we will make use of these results later we will briefly review them here. These results state that a d dimensional state, with a vector of Schmidt coefficients in decreasing order $\underline{\alpha}^{\downarrow}$, can only be converted into a state with sorted Schmidt coefficients $\underline{\beta}^{\downarrow}$, if

$$\underline{\alpha}^{\downarrow} \prec^{w} p\underline{\beta}^{\downarrow}, \tag{2.9}$$

with $0 \leq p \leq 1$ being the probability of succeeding. This means that, for $k = 1, ..., d$,

$$\sum_{j=k}^{d} \alpha_j^{\downarrow} \geq p \sum_{j=k}^{d} \beta_j^{\downarrow}. \tag{2.10}$$

Eq. (2.10) gives us the direct result that a single pure state $|\alpha\rangle$ can be converted into a higher entangled state, $|\beta\rangle$, with a probability of

$$\frac{\min(1-\alpha,\alpha)}{\min(1-\beta,\beta)}. \tag{2.11}$$

This single state operation is a type of filtering, where a weak measurement performed on one of the qubits reveals enough local information to enhance the entanglement. In the specific case, when a perfect singlet is obtained, this form of entanglement distillation is known as the Procrustean method [92]. Hence, any pure two-qubit state $|\alpha\rangle$ can be converted into a singlet, $|1/2\rangle$, with a probability of $2\min(1-\alpha,\alpha)$. Unfortunately, it has been proven that filtering operations do not increase the fidelity of general mixed states [93, 94]. Note that to perform the operations associated with majorization, e.g. to accomplish the Procrustean operation, the pure states must be known.

For mixed states the situation is far more complicated and there are still many open questions even regarding bipartite purification. The simplest example of purification in this case was given by Bennett's recurrent method [42]. This starts with two Werner states split between locations. One of the states is the target state and the other is the control state. Controlled-NOT operations, at each location, are performed between qubits of the target and control states. Local measurements of the target state can then reveal whether we should keep the control state, with a higher degree of entanglement, or discard it. This scheme was later improved on to give the DEJMPS scheme [43]. Both are probabilistic methods and actually give a zero yield. However, they can distill any Werner states with $\lambda > 1/2$. In order to obtain highly entangled states they must be repeated and this would require a vast number of states to be initially stored. One way to overcome this issue is by using a method called "entanglement pumping" [95]. Instead of applying the purification procedure

to identical states this procedure keeps applying the purification to the state being pumped and an initial state. By repeatedly doing this the pumped state increases its entanglement and only two states need to be stored at any time. If it fails it must be restarted from the beginning and it can not create a state with arbitrary entanglement. To get to any level of entanglement the scheme must be concatenated to give "nested entanglement pumping". This applies the basic pumping scheme to give entangled states of a new level to be used in a separate pumping scheme.

The mixed state purification scheme with the highest yield is the "hashing" method [90], which is closely linked to the "breeding" protocol [42]. These are both M to N schemes. As well as the initial partially entangled states the breeding scheme also starts with a collection of perfectly entangled states. It involves performing controlled-NOT (CNOT) operations between a random set of partially entangled state and a singlet, at each location. The singlet's qubits are then measured to reveal information on the errors that can then be removed.

The ability to purify and distill entanglement is our first demonstration of a means to enhance the entanglement between two nodes into a resource that can then be used. It allows a few basic measures of success to be introduced. These "figures of merit" will be used to measure the effectiveness of protocols later. In the pure state case they include the probability of successfully generating a perfect singlet between the nodes, the concurrence and the worst state entanglement. The concurrence can also be applied in the mixed state situation but we will generally use the fidelity between a maximally entangled state and the final state as a measure of success.

2.4 Entanglement Swapping

Purification procedures and error correction are of limited use alone. Once the entangled state has degraded to a separable state it is useless, even for purification. This is where the concept of entanglement swapping can be employed [44, 45, 46]. It allows two entangled states to be combined in order to produce a single entangled state. Systems that have never been in direct contact are left entangled by this procedure. To understand swapping it is beneficial to first understand quantum teleportation [11]. Consider a singlet state shared between two nodes, say C_1 and C_2. If C_2 has a separate quantum qubit they can transfer this to C_1 without sending any quantum information directly. To do this C_2 performs a measurement in the Bell state basis between their singlet qubit and the qubit to be transferred. The outcome of this measurement is sent classically to C_1 where local operations retrieve the teleported qubit. If the initial entangled state was not a maximally entangled singlet the teleportation operation is equivalent to sending the qubit to C_1 through a channel. The procedure is depicted in Fig. 2.2(a). All of the teleported qubits quantum correlations with other systems are maintained throughout teleportation. Hence, if another singlet is shared between C_2 and C_3, C_2 can teleport their qubit from this singlet to C_1 (see Fig. 2.2(b)). This can be generalized to see how the procedure acts on nonmaximally entangled states and if the Bell measurement is optimal. The initial pure two-qubit states we consider here are $|\,\alpha\rangle$ and $|\,\beta\rangle$, with $\alpha \geq 1/2$ and $\beta \geq 1/2$. The four orthogonal states for the measurement basis, $|\,m_i\rangle$ can be decomposed in the "magic basis", $(|\,\Phi^+\rangle\,, \mathrm{i}\,|\,\Phi^-\rangle\,, \mathrm{i}\,|\,\Psi^+\rangle\,, |\,\Psi^-\rangle)$, with corresponding coefficients $m_{i,1}, m_{i,2}, m_{i,3}, m_{i,4}$ respectively. Using this basis the concurrence of each state is $C(|\,m_i\rangle) = |\sum_j m_{i,j}^2|$. In Ref. [58] this was done to calculate that the

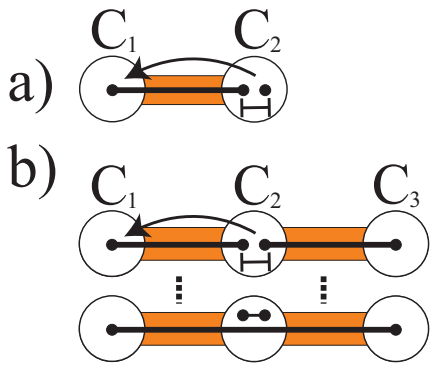

Figure 2.2: (a) Quantum Teleportation. For teleportation a measurement in the Bell basis is performed between a qubit from a singlet and a data qubit. After classical communication and local unitaries the remaining singlet qubit at C_1 has the data qubit's state. (b) Basic arrangement for entanglement swapping. Entanglement swapping involves a measurement in the Bell basis at node C_2 and classical communication between the nodes followed by local unitaries which causes C_1 and C_3 to become entangled.

outcomes have a probability of

$$p_i = p_{min}(m_{i,1}^2 + m_{i,2}^2) + p_{max}(m_{i,3}^2 + m_{i,4}^2), \tag{2.12}$$

where $p_{min} = (\alpha(1-\beta)+(1-\alpha)\beta)/2$ and $p_{max} = (\alpha\beta+(1-\alpha)(1-\beta))/2$. For each outcome the resulting pure state has a Schmidt coefficient of

$$\gamma = \frac{1}{2}\left(1 - \sqrt{1 - \frac{\alpha\beta(1-\alpha)(1-\beta)}{p_i^2} C^2(|\, m_i\rangle)}\right). \tag{2.13}$$

Hence, swapping procedures that use Bell measurements, with $C(|\, m_i\rangle) = 1$ and maximize γ, are indeed optimal. Although the type of Bell measurement depends on the figure of merit being used. To maximize the concurrence any Bell measurement is suitable. Yet for the worst case entanglement (WCE) to be maximized a measurement of Bell states in the XZ basis is optimal. This is because this results in $p_m = 1/4$ for each measurement and for each possible outcome. A Procrustean operation can be performed on the resulting state to create a singlet. The probability

of obtaining a singlet is optimized by a Bell measurement in the ZZ basis. In this case a singlet is obtained with a probability of $2\min(1-\alpha, 1-\beta)$. This is clearly optimal since, from majorization results, the best possible probability of obtaining a singlet from each initial state is $2(1-\alpha)$ and $2(1-\beta)$. The combined system can not generate a singlet with a probability larger than twice the minimum of $1-\alpha$ and $1-\beta$. It notable that if $\alpha = \beta$ the singlet conversion probability (SCP) for the combined system is the same as for one of the states. This is only the case with one swapping step and corresponds to the "conserved entanglement" discussed in Refs. [96, 46]. Also, for two of the measurement outcomes the resulting state is more entangled than the initial state and this can be used as a purification procedure.

Further generalizations of swapping procedures have been made and applied to mixed states and higher dimensional systems. This topic is known as remote preparation of entanglement [97, 98]. One of its primary results is that, with initial two-qubit states, the concurrence of the final state is bound by the product of the initial states concurrences [97].

2.5 Quantum Networks

So far I have only considered small systems composed of entangled states. For larger systems the qubits are partitioned into sets, with all of the qubits in a set being local to each other. During this thesis I will refer to these local regions as nodes and they can be thought of as physical locations, such as cities on a map. When LOCC operations are allowed quantum operations can be performed within each node and classical information transmitted between them. In the situation where the initial entangled states are bipartite they can be represented by edges linking the individual subsystems. These edge states are not necessarily maximally entangled. When the entangled states are split between nodes a distant entanglement relationship has

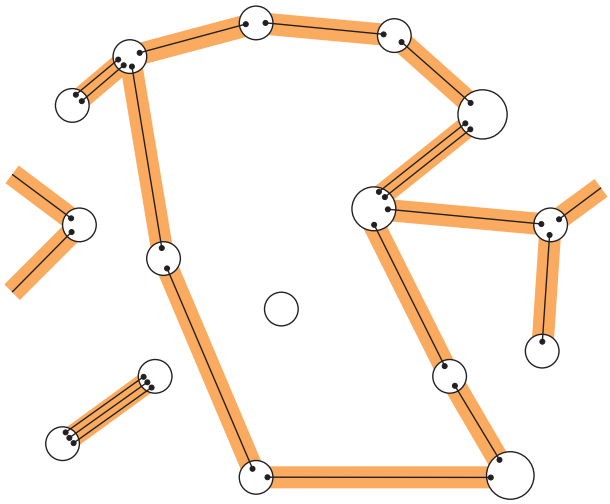

Figure 2.3: An example quantum network. The two qubit entangled states are represented by black edges. Each of these is composed of two qubits (black circles) that are split between nodes (large black outlined circles). These nodes represent locations in which quantum operations can be performed. All of the edges between two nodes are grouped into bonds (orange lines). The nodes and bonds define the network structure.

been created. By grouping all of the edges linking two nodes into a "bond" we have formed a network describing the structure of the entanglement. This is a quantum network and an example is given in Fig. 2.3. Using edges to represent the initial entanglement is only suitable for bipartite states. However, because bipartite states are far easier to create and are the primary type of entanglement in current quantum cryptography implementations, this is the case I will consider for the initial states.

These networks are naturally represented with an undirected graph containing a set of nodes (or vertices), V, and a set of edges, E. The number of node, N, is the networks size. I refer to all of the edges between two specific nodes as a bond (or connection) and self-loops are not allowed. The number of connections a node has to other nodes is its degree, k. In any network the degree distribution, given by the probability, p_k, that a vertex has degree k, is a key property of the network. Along these connections paths that link two vertices can be defined. The networks I will consider are un-weighted. Hence, each path has a length given by the number

of edges traversed along it. For these networks the shortest path length, which is also called the intervertex or geodesic distance, between two nodes is the minimum length of all paths between those nodes. To find such paths a classical breadth-first search algorithm can be applied [99]. An average of the shortest path length can be taken between every pair of nodes in V to calculate the mean shortest path length $\overline{l}$. A connected component of the graph refers to a subset of the nodes that can be linked by a path without any further nodes being added. There can be numerous connected components, or clusters, in a network. Difficulties arise in defining the mean shortest path length in networks with multiple clusters. To get around this the pairings for the average are usually restricted to vertices within the same cluster. If the number of nodes, *i. e.* the size, of the largest cluster is proportional to the size of the network it is called a giant component or cluster. The existence of a giant component is directly related to percolation. For example, in bond percolation the existence of a bond on the original graph is determined with a probability, p. Once p exceeds a percolation threshold a giant cluster exists that scales proportionally to the original network size. For an infinite network this corresponds to an infinite component that contains a finite nonzero fraction of the nodes. The probability that a node belongs to the infinite cluster is known as the percolation probability, $\phi(p)$. Below the threshold no such cluster is present and the resulting network is split into an infinite number of small finite clusters. I will describe this in much more detail during chapter 5 and provide a few example percolation thresholds. A full description of percolation can be found in Ref. [100]. In a similar way to the mean shortest path length and degree distribution, the distribution of cluster sizes and related average cluster size are basic properties of the network that reveal aspects of the network's large scale structure. There are three specific classes of network that I will consider and these are described below.

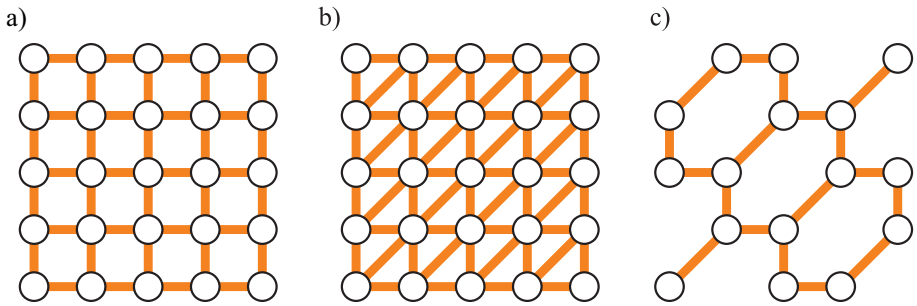

Figure 2.4: (a) A regular square lattice network composed of bonds (orange lines) and nodes (circles). (b) Regular triangular lattice. (c) Regular hexagonal lattice. This is also known as a honeycomb lattice.

I Lattices and Regular Networks

The simplest large scale networks that I will consider are deterministic and based on regular lattices. These have repeating unit segments. Examples of these include graphs based on square, triangular and hexagonal (or honeycomb) lattices (see Fig. 2.4). The lattice can have any dimension and, hence, three dimensional cubic lattice networks are included. In graph theory a k-regular network is specifically a network where every vertex has degree k. Many lattice based networks have this form but not all. One key property of these networks is that the shortest distance between two nodes matches the metric properties of the space the lattice is based in. This is represented by the fact that the mean shortest path length, $\overline{l}$, scales as a positive power of the network size, $N^{1/d}$, with d being the lattices dimension.

II Hierarchical Networks and Trees

Hierarchical networks are deterministic networks that have multiple iterations, with each one constructed from the previous iteration using a rule. Examples are shown in Fig. 2.5(a-b). Included in this definition is the Cayley tree, shown in Fig. 2.5(c). In graph theory a "tree" is any connected network with no loops. The Cayley tree is a finite network with all of the vertices having a

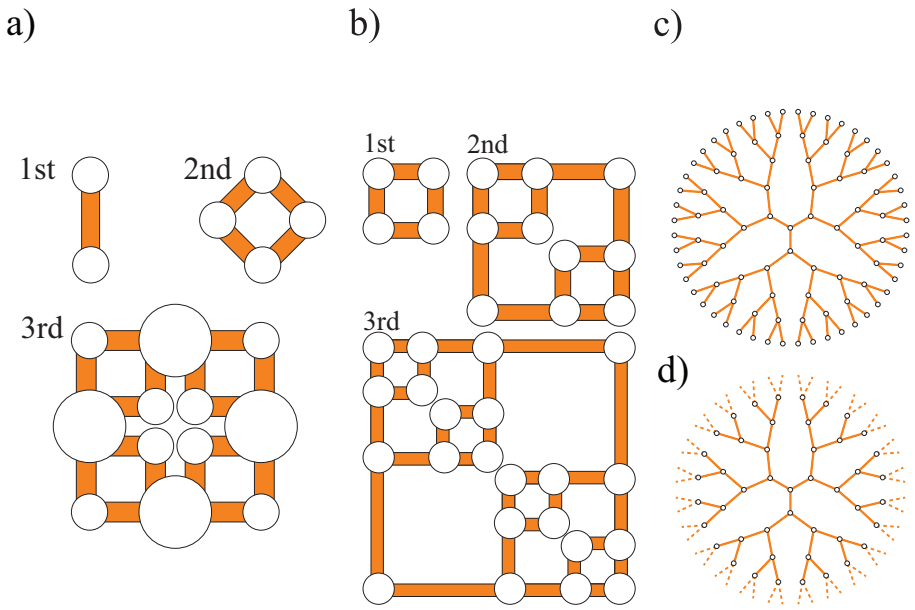

Figure 2.5: (a) First three iterations of the hierarchical diamond network. (b)First three iterations of the hierarchical tree network. (c) A Cayley tree network. (d) The Bethe lattice.

fixed degree except for a boundary of vertices that have degree one. To define it in a hierarchical form a rule is specified that states that at each iteration a set number of new vertices are attached to each boundary vertex. Repeating this indefinitely we obtain the regular infinite Bethe lattice (see Fig. 2.5(d)). Note that in all tree networks there is a unique path between any two nodes.

III Random and Complex Networks

A random network is an element of an ensemble of random graphs. A review of random networks can be found in Refs. [101, 99]. The graphs in the ensemble have specific parameters fixed, together with the number of vertices. Typically, properties of random networks are considered over the entire ensemble. For large graphs one element may be enough to characterize the parameter of interest. In this case the graphs are said to be self-averaging. The most basic random graph model is the Gilbert model, $G(N, p)$, and simply corresponds to connecting vertices randomly, each edge independently existing

with a probability p. The mean vertex degree in this case is $c = (N-1)p$. Related to this is the Erdos-Renyi model (see Fig. 2.6(a)), $G(N, M)$, where the network is chosen randomly from an ensemble of simple graphs that all have M edges. For the Erdos-Renyi model $c = 2M/N$. In the asymptotic limit these are equivalent. The degree distribution for both models is also Poissonian, *i. e.* $p_k = e^{-c}c^k/k!$, so both are sometimes called Poisson random graphs. Complex networks are networks that contain nontrivial topological features and are typical of networks formed in the real world. The study of such networks is a new and growing interdisciplinary field. Many of these networks exhibit a "small-world" phenomenon. This property exists when the mean shortest path length scales logarithmically with the network size, $\overline{l} \sim \log(N)$. The random networks discussed are examples of small-world networks and, when the vertex degree exceeds two, the Bethe lattice is also small world. A further example that combines a deterministic and random structure is Watts-Strogatz model. The Watts-Strogatz network is based on a adding random "short-cuts" to a regular lattice network (see Fig. 2.6(b)). Typically, real-world networks, such as the world-wide web, are thought to exhibit a "scale-free" property. Meaning that the degree distribution exhibits a power-law, $p_k \sim ck^{-\gamma}$, rather than being Poissonian. These networks are dominated by nodes that have a high degree called "hubs". This results in a high tolerance against faults and an ultra small-world property [102]. An example of a scale-free network is illustrated in Fig. 2.6(c). In this thesis I will only introduce complex networks and briefly refer to complex networks when relevant.

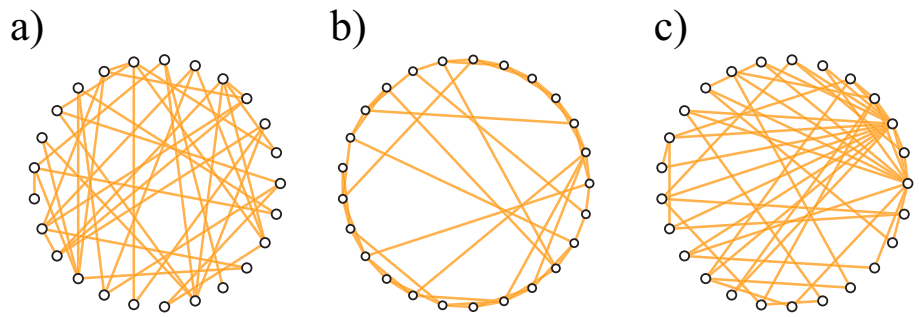

Figure 2.6: (a) A random Erdos-Renyi network composed of 25 nodes. (b) A Watts-Strogatz small-world network. (c) An example scale-free network.

2.6 Chapter Summary

During this chapter I have introduced some of the key manipulations and fundamental ideas that aid in entanglement distribution. Specifically, entanglement purification and swapping. As can be seen there are various versions of these procedures and their development is still ongoing. I have given a basic example of their application to simple entangled systems. Extending on these small systems I have outlined how I use quantum networks to describe larger systems. The field of complex networks is rapidly expanding and I have introduced some of the very basic concepts and network examples from this field. In physical situations the entanglement present in the complex network's bonds would vary and still decrease with distance. This distance dependence would still need to be overcome. Despite this, there have been a few inspiring results found in regards to entanglement distribution on these complex networks which I will discuss in the next chapter. Many of the protocols that I later introduce can be applied to models of these complex networks, however my main examples throughout this thesis will be regular and hierarchical networks. This is because the repeating structure of lattices ensure similar levels of entanglement can be obtained in all of the bonds. The most basic approach to entanglement distribution on any network is composed of combining swapping and purification operations. Typically, it is always preferable to perform purification whenever pos-

sible. The study of this scheme on large networks is difficult due to the freedom available in choosing which operations to perform. This is exemplified in a recent paper where the best performing method depends on the means of quantifying the success [103].

Chapter 3

One Dimensional Networks and their Implementations

Most previous work on entanglement distribution has focused on quantum repeaters. The theoretical proposals for these are surveyed in this chapter. This includes a short discussion on their implementations and how they can be embedded into quantum networks.

I have discussed manipulations that enable the fragility of entanglement to be overcome. However, I have not mentioned how these systems can be combined in order to generate entangled states over extended distances. This brings us on to the field of the quantum repeaters, which have been extensively studied and are currently the favoured method for possible future entanglement distribution. They can be thought of as entanglement distribution on a one-dimensional network, where the nodes initially share entanglement with two neighbouring nodes. This type of network is illustrated in Fig. 3.1. The task is to generate a useful entangled state between the end nodes of the linear array. Various methods have been proposed to accomplish the task. The aim of this chapter is to give a quick overview of these methods. I will discuss their structure, how they work and their restrictions. By doing this I hope to highlight the improvements that can be found by using

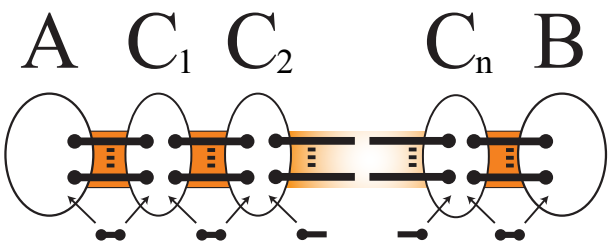

Figure 3.1: One-dimensional network linking the end nodes, A and B, with nodes C_i. The nodes are linked by bonds containing entangled bipartite states (black lines). In a quantum network the entangled states may be continually created between nodes, adding to the edge contents of the bonds.

higher-dimensional network structures. The chapter will be structured as follows. I begin by describing the straightforward application of entanglement swapping called a quantum relay. Limitations to this method will become apparent. I describe how it logically extends to the standard repeater protocol and its variations [51]. The seminal repeater implementation introduced in 2001 by Duan, Lukin, Cirac and Zoller [49] is then discussed. All of the theoretical repeater proposals require a few key quantum technologies to be realised in reality. The greatest difficulties arises at the interface of the photonic transmission and quantum processing. Photonic entanglement needs to be stored and then processed with a high fidelity. This needs two primary components. The first of these are quantum memories and the second are highly efficient photo-detectors. The current state of these technologies are discussed. Recent alternative theoretical proposals make use of error correction [53, 104], dissipation [105] and measurement based computing [106]. I close the chapter with a discussion of error correction based repeaters and how repeaters can be used for entanglement distribution within networks.

3.1 The Quantum Relay

In the previous chapter I gave an overview of entanglement swapping. This procedure allowed us to entangle two states that had never been in contact. This is done by means of a local two-qubit measurement and can be repeated between the newly entangled state, left after the first swapping operation, and another entangled state. The quantum relay is based on repeating this operation along a series of $N+1$ nodes, i.e. performing Bell measurements along every node containing two qubits in an effort to leave the remaining qubits entangled. To give the first illustration of this lets assume that we have $N+1$ nodes in a linear array and all of the initial states are identical pure two qubit states, $|\alpha\rangle$, with $\alpha > 1/2$. For this linear qubit array the maximum probability that we can obtain a singlet between the end nodes is bounded by the maximum concurrence. In Ref. [58] it was shown that this maximum concurrence is given by $[4\alpha(1-\alpha)]^{N/2}$, when XZ Bell measurements are performed for each swapping operation. This gives a bound to the maximum probability. Although it was shown that the use of this maximum concurrence scheme only obtains singlets with a probability that scales as $[4\alpha(1-\alpha)]^{N}$. This is greatly enhance by using ZZ Bell measurements to give the probability scaling as $[4\alpha(1-\alpha)]^{N/2}/\sqrt{N}$. Another strategy that can be employed is a classical percolation strategy, where the Procrustean method [92] converts the bonds to a singlet with a probability of $2(1-\alpha)$ and then swapping can be applied to give a final singlet, between the end nodes, with a probability of $[2(1-\alpha)]^{N}$. These success probabilities decrease exponentially with the number of nodes swapped over, unless the initial states are all maximally entangled. Although the quantum relay can not stop the entanglement degrading over these distances it does help to solve issues relating to signal attenuation. Once we increase the number of edges between each node to m it is no longer the case that maximally entangled states are required for a perfect singlet to be created over

an arbitrary distance with a constant probability. This is the first example in this thesis of long distance entanglement distribution. To accomplish this task majorization results [91] are used to show that perfect singlets can be distilled between each bond as long as $\alpha^m \leq 1/2$, with certainty. Once this has been done entanglement swapping can be performed to link up theses states. Note that this only shows that this is possible and does not give us the lowest required amount of entanglement required for a constant probability. The pure states must also have a known value of α in order to perform the conversions based on majorization. Unfortunately, once mixed states are considered the ability to perform long distance entanglement distribution on a one-dimensional network completely disappears. To give an example of why consider a network of initial mixed Werner states (see Eq. (2.6)), $\rho_W(\lambda)$, i.e. mixtures of a pure state and completely mixed state. This can be thought of as a mixture of these states. Whenever all of the edges between two nodes are separable states it becomes impossible for the end qubits to be left entangled and no entanglement is left. The probability of this not occurring on any of the bonds is $(1-(1-\lambda)^m)^N$ and this decreases exponentially with distance. If we want a constant success probability we must increase the number of edges, m. The quantum relay can only be used to distribute entanglement over a limited number of nodes. To extend the entanglement further more resources are required. These extra resources could have been included in the initial bonds and purified there, however due to memory and operational errors the improvements this can yield are still limited.

3.2 The Standard Repeater Protocol

Despite these limitations there have been various methods proposed to accomplish entanglement distribution along a one-dimensional array using mixed states. The first description of the standard repeater was given in Ref. [47]. In the standard

repeater the distance, N, is split between L^n bonds, with all of the required states being initially created between the nodes. The distance between each node is limited by the extent to which either the free space or a separate quantum relay can create entangled states before they become separable. At each node the edges are purified up to a required level before further swapping is performed. L refers to the number of bonds swapping operations are performed over before further purification. In many cases it is assumed that $L = 2$ to simplify matters. The scheme uses M repeater purification steps at each node. After the swapping further purification is performed and this process is continued up higher levels until the end nodes are linked by a sufficiently entangled state. This nested purification process, combining swapping operations and purification is the fundamental idea behind purification based repeaters. The total number of initial required states is $R = (LM)^n = N^{1+\log_L(M)}$. The time required grows polynomially with distance. Although this achieves a polynomial increase in resources with distance it requires all of the states to be initially created and stored throughout. This raises various technical problems both in terms of storing the resources and manipulating them.

3.3 The Innsbruck and Harvard Repeaters

To reduce the large number of stored qubits required by the standard repeater, entanglement pumping was proposed to increase the entanglement between nodes [95]. This strategy is called the Innsbruck protocol. The states can then be created continuously to pump the entanglement between nodes to a required level. At that stage a swapping operation is performed linking further pairs with an entangled state that can be used to pump the entanglement up between those pairs. This process is then repeated. Again the linear array is split between L^n bonds and for each level, n, of the repeater an extra qubit is required for storage on every L^nth

node. Hence the required number of storage qubits only grows logarithmically with distance. This is at the expense of an increase in polynomial time scaling. A failure in the purification at any level also requires the state to be discarded and the entire purification process for that link needs to be started again at the lowest level. The other states must wait for this to occur and these waiting times become another significant problem when memory errors are considered.

A further reduction of the required number of storage qubits was obtained by Childress et al [50, 107]. Their variation of the Innsbruck protocol, called the Harvard protocol, uses only two qubits per node. It achieves this at the expense of longer waiting times for higher level qubits.

3.4 Implementations and the DLCZ Repeater

The implementation of any entanglement distribution architecture can be split up into three steps - the initial creation of entangled states, separating these states through channels and manipulating them with quantum operations. As previously mentioned, photons are ideal for maintaining the entanglement through long distance channels. The most common method of creating entangled photons is via parametric down conversion where a nonlinear crystal is used to down-convert single photons into pairs of photons that are polarization or momentum entangled [108, 109, 110]. The quantum channel can then either be implemented in free-space or through an optical fibre. Free-space transmission is subject to significant loss. The longest distance achieved through free space has been 144km [111, 32], but this was with a channel loss of 64dB [111]. Proposals to use satellites are now being made that only experience atmospheric loss in a small fraction of the photon's path [37]. Optical fibres are the preferred channels for quantum cryptography [31, 30] and a review can be found in Ref. [112]. Typical single mode fibres

have a diameter of a few wavelengths and attenuation of 0.2dB/km at 1500nm. It is the manipulation of the photons at the nodes that is the main hindrance to realizing entanglement distribution. Photonic qubits are not ideal for quantum manipulation and many of the protocols require storage of the states. This means that the photonic state needs to be coherently mapped onto another state. Ideally, this state would be resistant to environmental noise, open to quantum operations and can either be mapped back to a photon or measured. Devices aimed at achieving this are referred to as quantum memories.

The ability to perform measurements on the recovered photons efficiently using photo-detectors are also essential. Well-established semiconductor avalanche photodiodes (APDs) do not give sufficient efficiency for practical repeaters and typically do not allow photon number resolution. The highest efficiency photo-detectors, superconducting transition-edge sensors (TESs), achieve an efficiency of approximately 95% and give photon number resolution. However, they require very low temperatures($\approx$ 100mK) and give slow response times($\approx 1\mu$s). Recently, the National Institute of Standards and Technology (NIST) has shown progress at increasing the speed of TESs. Superconducting nanowire single-photon detectors (SNSPDs) have also been created that have higher efficiencies than 90%, fast response times ($\sim$ 10ps) and operate at $4K$. Unfortunately, SNSPDs do not have photon resolution. For a review of current photo-detectors please see Ref. [113].

3.4.1 The DLCZ Repeater

In 2001 Duan, Lukin, Cirac and Zoller proposed an implementation of the nested quantum repeater that is now called the Duan-Lukin-Cirac-Zoller (DLCZ) protocol [49]. This focused on a simplified repeater that avoided issues with the implementation. Instead of entangling two photons initially the DLCZ protocol creates a

photon entangled with the collective excitation of an atomic ensemble. This ensemble acts as the quantum memory but avoids mapping from the photonic state into it. The atomic ensemble is composed of a cloud of identical atoms that have a Λ level structure. This structure contains a pair of metastable lower states $|\, g\rangle$ and $|\, s\rangle$. An off-resonant pump pulse can then induce a Raman transition between these states and produce forward-scattered Stokes light. In an ensemble this leads to a collective excitation. To create the entanglement they are simultaneously excited so that they probabilistically emit one Stokes photon. At a central station a beamsplitter is used to remove the "which-way" information and detectors measure the outcoming photons. If one photon is detected entanglement has been generated. This produces entanglement in a "heralded" way, such that one knows once two ensembles are entangled. The state of the memory is recovered using a retrieval light pulse. The DLCZ protocol also avoids the task of performing a complete swapping operation. Once two states are available a probabilistic swapping operation is performed by a beam splitter. This is performed by extracting the qubit from each ensemble and interacting them again via a beamsplitter. The swapping process is only successful if one photon is detected after the interaction. This procedure creates a long distance entangled state after a time that scales polynomially with distance. A review of the DLCZ protocol and more recent variations of it can be found in Ref. [114].

3.4.2 Quantum Memories

The DLCZ protocol employs an ensemble-based quantum memory that does not directly store a photon and is measured by retrieving a photon. This type of memory has achieved impressive experimental results [115, 116, 117, 118]. Yet, it is only one suggestion out of many for quantum memories. A review of possible memories can be found in Ref. [119]. Here I only give a very brief summary of the different techniques.

For entanglement distribution these memories need to have a long storage time, the ability to efficiently couple to photons, and a high fidelity between the stored and retrieved quantum information. Of course, the memory needs to be compatible with the entanglement source putting restrictions on the wavelength and bandwidth. It is also highly advantageous to have memories that can simultaneously store multiple photons with a large bandwidth as these allow greater repetition rates.

A similar proposal to the DLCZ memory allows a photon to be coherently stored using the Raman transition [120, 121, 122]. This proposal has been experimentally demonstrated in a warm caesium vapour [123]. An exciting proposal has also been made to use a similar scheme in diamond to store a photon into an optical phonon of the diamond [124].

Another possible room temperature approach involves the trapping of light in a warm alkali gas medium. A strong control field is used to render the medium transparent using electromagnetically induced transparency (EIT) [125, 126, 127]. By adiabatically turning this control field off the group velocity of the signal light is reduced to zero. The light is then halted inside the medium and, by adiabatically switching the control field back on, the signal can be retrieved.

Both the Raman and EIT memories require knowledge about the signal pulse shape. Photon echo based quantum memories do not require this knowledge. An example of such a photon echo quantum memory is based on exploiting controlled reversible inhomogeneous broadening (CRIB) [128]. Typically, inhomogeneous broadening decreases the fidelity of quantum memories but these protocols create a controlled broadening of the excitation state and absorb the signal light into this state. By reversing the broadening the pulse can then be recovered. For a review of this technique please read Ref. [129]. The first proposal was based on hot gases [130] but three groups later described how CRIB could be extended to rare-earth doped solids [131, 132, 133]. Atomic frequency comb (AFC) based quantum memories [134]

are related to CRIB memories. In AFC memories the absorption profile of an inhomogeneously broadened solid state atomic medium is tailored to be a periodic series of narrow peaks. This periodic structure causes the absorbed state to automatically rephase after a set period of time. For both CRIB and AFC memories the storage time can be extended by transferring the evolving excited state into a long lived ground state using a control pulse.

There has been a great deal of theoretical and experimental progress in realizing these memories. However, few of these proposals allow for flexible quantum processing of the stored information. In contrast, the field of performing quantum information processing in individual quantum systems is well developed. Such systems include individual trapped ions [135], nitrogen vacancy centres in diamond [136, 137] and quantum dots [138]. Proposals for repeaters based on these have the potential for a significant improvement over those with ensemble memories, primarily because they are not limited to probabilistic swapping [139]. Unfortunately, the coupling of these with light is very small and, due to the necessary cooling and trapping, they are experimentally challenging to implement. To overcome the small interaction a cavity can be used [140, 141]. However, using such cavities is also technically challenging and reduces the the bandwidth of the light that can be stored. This would mean that the entire protocol must be run slower and leads to a greater susceptibility to decoherence. Single systems are also unsuitable for protocols that require multi photon states.

3.5 Quantum Error Correction based Repeaters

Despite the tremendous theoretical improvements the purification based quantum repeaters give over direct transmission they are generally slow and given a finite coherence time for the memories a limit is placed on the maximal level of nested

purification and hence distance. To remove this obstacle the memories could make direct use of the quantum error correcting codes briefly introduced in chapter 2. Quantum error correcting codes are designed to correct errors through a quantum channel and can simply be used to correct for the error caused by using entangled states for teleportation. Using error correcting codes to aid quantum communication was initially proposed before purification based repeaters [142]. This scheme achieved a polynomial scaling of resources with distance. Recently, there have been a few proposals that improve on this [53, 104]. These protocols encode the entire Bell state using an error correcting code and then use Bell measurements at the nodes to obtain an error syndrome. By doing this the error correction and swapping operations are combined. The Bell measurements can be performed simultaneously and the classical data collected at one of the end node. By doing this a logarithmic scaling of qubits per node can be obtained with a constant rate. The initial entangled pairs still need to be generated and in Ref. [53] this is done by an initial purification phase. In Ref. [104] they employ a surface code to remove this step and obtain a higher rate of entanglement generation. A measurement based 3D cluster state entanglement distribution scheme, that also makes use of surface codes, is described in Ref. [143].

3.6 Network Implementations

Although the quantum repeater protocols are designed for a one-dimensional quantum network there are other quantum networks that have strong relationships to this situation. In tree structures there is only a single path of bonds between two specific nodes and this maps directly to a linear array. Hence, for the task of creating entanglement between two specific nodes it is not possible to outperform a quantum repeater protocol that is applied directly along this path. In these situations

the distance is given by the shortest path in the network between two nodes. For quantum networks composed of pure states it has been demonstrated that classical path finding algorithms, like Dijkstra's algorithm [144], can be adjusted to find the optimal route for a repeater [145]. This is not the case for mixed state networks but these algorithms still work well. In Refs. [60, 146] it was shown that for networks that show a small-world phenomenon it is possible to obtain efficient entanglement distribution between any two randomly chosen nodes in a small-world network by using the simple quantum relay along a path. This is because the typical path length in these networks does not increase polynomially with the total number of nodes. However, to take advantage of this the same level of entanglement must be present in each bond along the path. In physical realizations the entanglement would decrease with the coordinate space distance and other methods such as quantum repeaters would be required along the complex networks bonds to overcome the distance limitation. By implementing advanced repeater schemes along the paths the efficiency of quantum entanglement distribution can likely be increased further.

3.7 Chapter Summary

I have given a brief review of various theoretical quantum repeater schemes that have been proposed for entanglement distribution along a one-dimensional network. The most efficient schemes proposed to date require a logarithmic increase in local resources with distance. These protocols can be applied directly to the problem of entanglement distribution between two nodes in a general network. However, currently no experiment has been able to outperform direct transmission. This can be especially efficient when the network possesses small-world characteristics however the rate still decreases with the path-length and separation distance.

Chapter 4

Limitations of Entanglement Distribution

In this chapter I will explore restrictions on entanglement distribution caused by having limited initial entanglement resources. I give a necessary and sufficient condition for the production of a perfectly entangled singlet from a bipartite network, containing a finite number of entangled states. Then results from the field of assisted entanglement distillation are applied to study entanglement distribution in the asymptotic limit. By doing this I obtain a capacity for any bipartite quantum network. I will also discuss a restriction on the relationship between the required amount of entanglement and distance that is imposed by using mixed states. [1]

4.1 Introduction

In the previous chapters I have introduced entanglement and emphasized that it can be viewed as a resource in nature. Like all resources it is consumed to accomplish specific tasks. When the initial entanglement is limited this imposes restrictions on what can be accomplished. For the task of entanglement distribution on a quantum network these restrictions are associated with the distance over which entanglement

[1] Some of the material in this chapter has been published in the articles, Stuart Broadfoot, Uwe Dorner and Dieter Jaksch - EPL (Europhysics Letters) **88**, 5, 50002 (2009) and Phys. Rev. A **81**, 042316 (2010).

can be generated and the resulting amount of entanglement. If we impose strict conditions on the type of resulting entangled states we similarly require specific initial conditions in order for any distribution procedure to be successful. In this chapter I will cover a few limiting results that I have found. It is important to understand these limits so that reasonable starting conditions are used when exploring possible methods for entanglement distribution. I will start by looking at the specific case when a perfect singlet is required between two nodes, in a network that initially contains a finite number of entangled states. This situation is shown to impose very strict conditions on the initial bipartite states and the structure of the network. These very restrictive conditions can be removed by either relaxing the requirement for a finite number of initial states or by allowing for a mixed final state. Out of these I will first look at allowing large numbers of initial states and specifically in the limit of having an infinite number of states. This allows results previously obtained in the field of "assisted entanglement distillation" to be applied [147, 54]. Finally, I return to having a finite number of initial states and discuss how using mixed states imposes limits on the distance over which entanglement can be distributed.

4.2 Singlet Generation within a Network

In this section I consider quantum networks of arbitrary geometry as shown in Fig. 4.1 where the qubits in the nodes are "connected" by bipartite mixed states to qubits in other nodes. In the following I will prove that the generation of a perfect singlet between two arbitrary nodes A and B with finite probability in such a network is possible if and only if there are at least two paths of states linking A and B which have, up to local unitaries, the form

$$\rho(\alpha, \gamma, \lambda) = \lambda \left| \alpha, \gamma \right\rangle \left\langle \alpha, \gamma \right| + (1 - \lambda) \left| 01 \right\rangle \left\langle 01 \right|, \tag{4.1}$$

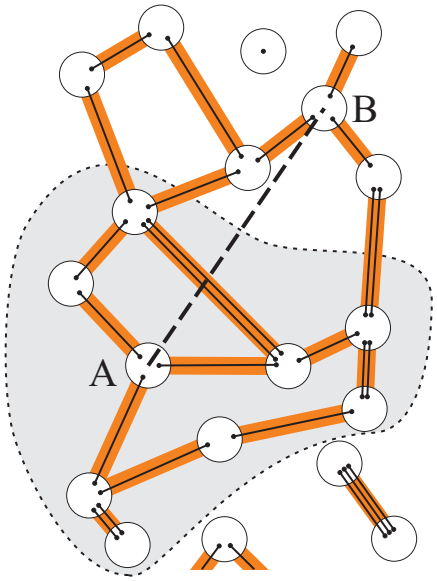

Figure 4.1: Mixed-state quantum network. Qubits in a node (circles) may be connected by bonds (thick lines), that is, they share mixed entangled states, "edges", (solid black lines) of qubits (black dots) with other nodes. When two "paths" of states of the form (4.1) connect A and B a singlet (dashed line) can be created with finite probability. This is proven by partitioning the nodes into two groups with one containing A (shaded region) and the other B. For it to be possible to generate a singlet between A and B, these groups must be linked by at least two states of the form (4.1) for all possible partitions.

where $|\,\alpha,\gamma\rangle = \sqrt{\alpha}\,|\,00\rangle + \sqrt{1-\alpha-\gamma}\,|\,11\rangle + \sqrt{\gamma}\,|\,01\rangle$, $0 < \alpha \leq 1$, $0 < \gamma \leq 1$, $0 < \alpha + \gamma \leq 1$ and $0 < \lambda \leq 1$. I show this by separately proving a necessary and sufficient condition which, together, prove the above statement.

Necessary condition. I split the network into two groups of nodes, $\mathcal{A}$, containing A and a finite number of other nodes, and $\mathcal{B}$, which consists of the rest of the network and particularly contains B. These groups are linked by a finite number of edges. A singlet can be established with finite probability, via local operations in the groups and classical communication between them, if and only if at least two of the states have the form (4.1). Appendix A contains a concise proof of this fact based on [148] which agrees with the result of Ref. [149], that, in general, a singlet can not be generated with a finite probability from a finite number of mixed states.

With two states of the form (4.1), $\rho(\alpha, \gamma, \lambda)$ and $\rho(\beta, \delta, \nu)$, we obtain a singlet with a finite probability by first performing two C-NOT gates locally, with the $\rho(\beta, \delta, \nu)$ state's qubits acting as the target qubits. These target qubits are then measured in the computational basis. If we find both qubits to be in the state $|\,1\rangle$ we have generated a pure entangled state between the qubits that originally corresponded to the $\rho(\alpha, \gamma, \lambda)$ state. I will refer to this measurement as the pure state conversion measurement (PCM). The state formed is

$$|\,\alpha'\rangle \equiv |\,\alpha', \gamma = 0\rangle = \sqrt{\alpha'}\,|\,00\rangle + \sqrt{1-\alpha'}\,|\,11\rangle\,, \tag{4.2}$$

where α' is a Schmidt-coefficient that has the value,

$$\alpha' = \frac{\min(\alpha(1-\beta-\delta), \beta(1-\alpha-\gamma))}{\alpha(1-\beta-\delta) + \beta(1-\alpha-\gamma)}. \tag{4.3}$$

The probability that the PCM succeeds in generating this state is given by

$$p_c = \lambda\nu(\alpha(1-\beta-\delta) + \beta(1-\alpha-\gamma)). \tag{4.4}$$

For identical states, *i. e.* $\alpha = \beta$, $\gamma = \delta$, the PCM already yields a singlet. Otherwise the state can be transformed into a singlet via the Procrustean method (see chapter 2).

The total success probability of generating a singlet is then given by the SCP

$$p_{\text{conv}} = 2\lambda\nu \min[\alpha(1-\beta-\delta), \beta(1-\alpha-\gamma)] \tag{4.5}$$

which coincides with the optimal probability for creating a singlet from two of these states [148].

I can perform this partition of the network in an arbitrary way, as long as one

group contains A and the other contains B. To be able to create a singlet between A and B via LOCC there must be at least two states of the form (4.1) in *all* possible partitions. This gives me a necessary condition that to create a singlet between two nodes with a nonzero probability there have to be at least two distinct "paths" of edges of the form (4.1) connecting the corresponding nodes. In Fig. 4.1(a) this is indicated by two spatially distinct paths of bonds. The states of the qubits that are not contained in this path are irrelevant and can therefore be in arbitrary states.

Sufficient condition. In order to show this I make use of entanglement swapping. If the edges are of the form (4.1), $\rho(\alpha, \gamma, \lambda)$ and $\rho(\beta, \delta, \nu)$, then there are four possible outcomes for each of the swapping operations Bell state measurements. The probabilities to obtain measurement outcomes corresponding to the Bell states $|\,\Phi^{\pm}\rangle = (|\,00\rangle \pm |\,11\rangle)/\sqrt{2}$ and $|\,\Psi^{\pm}\rangle = (|\,01\rangle \pm |\,10\rangle)/\sqrt{2}$ are

$$p(\Phi_{\pm}) = \frac{1}{2}(h_{\pm}\lambda\nu + (1-\beta-\delta)(1-\lambda)\nu + \alpha\lambda(1-\nu)) \tag{4.6}$$

and

$$p(\Psi_{\pm}) = \frac{1}{2}(g_{\pm}\lambda\nu + (1-\nu)(1-\alpha\lambda) + (\beta+\delta)(1-\lambda)\nu), \tag{4.7}$$

where

$$\begin{aligned} h_{\pm} =& \alpha\beta + (1-\alpha-\gamma)(1-\beta-\delta) \\ &+ (\sqrt{\alpha\delta} \pm \sqrt{\gamma(1-\beta-\delta)})^2, \end{aligned} \tag{4.8}$$

$$\begin{aligned} g_{\pm} =& \gamma\beta + (1-\alpha-\gamma)\delta + (1-\alpha-\gamma)\beta \\ &+ (\sqrt{\gamma\delta} \pm \sqrt{\alpha(1-\beta-\delta)})^2. \end{aligned} \tag{4.9}$$

If I measure the qubits at B to be in the states $|\,\Phi^{\pm}\rangle$ then I actually form another

state,

$$\rho\left(\frac{\alpha\beta}{h_\pm}, \frac{(\sqrt{\alpha\delta} \pm \sqrt{\gamma(1-\beta-\delta)})^2}{h_\pm}, \frac{\lambda\nu h_\pm}{2p(\Phi_\pm)}\right), \tag{4.10}$$

of the form (4.1). Unfortunately, for the other outcomes, the states' form is not generally maintained. Note that if $\delta = \gamma = 0$ I can discard these cases by replacing the state with $|\,01\rangle$ leading to an operation that transforms $\rho(\alpha, 0, \lambda) \otimes \rho(\beta, 0, \nu)$ into

$$\rho\left(\frac{\alpha\beta}{h_\pm}, 0, \lambda\nu h_\pm\right). \tag{4.11}$$

I can therefore create a state of the form (4.1) with nonzero probability between two nodes of the network (*e.g.* A and B in Fig. 4.1), given that these nodes are connected by a path consisting of states of the same form. Two such states, originating from two paths, can then be converted into a singlet, using a PCM and the Procrustean procedure. Unfortunately, this scheme leads to an exponential decrease of entanglement fidelity [48], and thus success probability, with the number of swapping operations. Hence it is not an effective solution to the problem of entanglement distribution. In the next chapter I will therefore introduce effective protocols which can be applied in regular network geometries and succeed in creating a singlet with a probability independent of distance.

Note that when entanglement swapping is done with pure states all of the outcomes can be used, and if these outcomes occur with probabilities p_m the pure state $|\,\tilde{\alpha}\rangle$ with

$$\tilde{\alpha} = \frac{1}{2}\left(1 + \sqrt{1 - \frac{\alpha\beta(1-\alpha)(1-\beta)}{p_m^2}}\right) \tag{4.12}$$

is recovered by using classical communication and local unitaries.

4.3 Bounds on the Distribution Rate

The problem of assisted entanglement distillation is strongly related to that of entanglement distribution [147, 54]. I will give a summary of entanglement of assistance results and the implications of these to my studies on entanglement distribution. The simplest example of assisted entanglement distribution considers a tripartite state, ψ^{ABC} that is shared between three systems. No quantum communication is allowed between these systems, however they can communicate classically. The entanglement purification protocols, that I have discussed in chapter 2, can produce $D(\psi^{\mathrm{ABC}})$ singlets from per initial state ψ^{ABC}, with $D(\psi)$ the "distillable entanglement" and depends on the protocol used. Using these distillation methods we could only hope to distill $D(\mathrm{tr}_{\mathrm{C}}\psi^{\mathrm{ABC}})$ singlets in this situation. The problem of assisted entanglement distillation asks how much additional entanglement can be distilled with the help of C, the third party.

For a basic example consider the third party, C, generating n random Bell states and distributing these to the systems, A and B. System C keeps a record of the types of Bell states distributed. If systems A and B are given no further help from C they are forced to distill the reduced state, $\mathrm{tr}_{\mathrm{C}}\psi^{\mathrm{ABC}}$, which is the maximally mixed state and yields no entanglement. In contrast, if C measures his record of the state and supplies this information to A and B they can perform unitaries on each Bell state to give n singlets.

This problem can be generalized to the multipartite entanglement of assistance problem where multiple "helpers" assist A an B in the distillation. In this situation a state $\psi^{C_1C_2\ldots C_mAB}$ is shared between the systems A, B and the helpers, C_1,C_2,...,C_m. From this the problem is to determine how much entanglement can be distilled between A and B when the operations are restricted to being local to each system. Specifically, if all of the helpers are measured to give the vector of outcomes $\mathbf{M}$, with

probability $p_{\mathbf{M}}$ and the resulting state $\psi_{\mathbf{M}}^{AB}$ then the entanglement of assistance is defined as

$$D_A(\psi^{C_1C_2\ldots C_mAB}) = \sup \sum_{\mathbf{M}} p_{\mathbf{M}} D(\psi_{\mathbf{M}}^{AB}), \tag{4.13}$$

where the supremum is taken over all possible measurements. Starting from a general mixed state, $\rho^{C_1C_2\ldots C_mAB}$, it has been proven in Ref. [54] that the optimal distillable singlet rate between A and B is given by the regularization

$$D_A^{\infty}(\rho^{C_1C_2\ldots C_mAB}) = \lim_{n\to\infty} D_A(\rho^{C_1C_2\ldots C_mAB\otimes n})/n, \tag{4.14}$$

Assisted entanglement distillation considers the distillation rate obtained when there are many copies of the state available rather than the limited case, of one state, considered by entanglement distribution. Results obtained to address the assisted entanglement distillation problem can be applied to give bounds on what is possible via entanglement distribution. It also shows how entanglement distribution would behave when there are a large number of entangled states linking the nodes. Unfortunately, this is of limited practical use since schemes based on this situation would require vast numbers of stored qubits and multipartite operations between these stored qubits. One bound is provided by the inequality

$$D_A^{\infty}(\rho^{C_1C_2\ldots C_mAB}) \leq \min_{\Upsilon} D(\rho^{A\Upsilon|B\overline{\Upsilon}}), \tag{4.15}$$

where the Υ is a subset of the helpers and $\overline{\Upsilon}$ is the conjugate set. This gives a cut of the system. A lower bound to Eq. (4.14) has been found [54] to be

$$D_A^{\infty}(\rho^{C_1C_2\ldots C_mAB}) \geq \max(I(A>B)_{\rho}, I_{\min}^{c}(\rho, A:B)). \tag{4.16}$$

Here $I(A>B) = S(B) - S(AB)$ is the coherent information, $S(\rho)$ is the Von

Neumann entropy. $I^c_{min}(\rho, A:B)$ is the minimum cut coherent information that is defined as

$$I^c_{\min}(\rho, A:B) = \min_{\Upsilon} I(A\Upsilon > B\overline{\Upsilon}). \tag{4.17}$$

For the pure state case this simplifies further to give the equality [150]

$$D^{\infty}_{A}(\psi^{C_1C_2\ldots C_mAB}) = \min_{\Upsilon} S(A\Upsilon)_{\psi}. \tag{4.18}$$

For the quantum networks that are formed by pure bipartite states, Eq. (4.18) can be simplified to give that the optimal rate of entanglement distribution is

$$D^{\infty}_{A}(\psi^{C_1C_2\ldots C_mAB}) = \min_{\Upsilon} \sum_{i} H(\alpha_i). \tag{4.19}$$

where the minimization is taken over all cuts and α_i is the Schmidt coefficient for each edge along the cut that is labelled with i. This is the lowest sum of each bond's distillable entanglement along any cut of the network.

This result can actually be easily shown. Consider n copies of the quantum network shared between all the nodes. In the limit of $n \to \infty$ each bond can be distilled to produce singlets and once this is done swapping operations can be performed between the nodes, A and B. The only limit to the number of singlets that can be created is given by the cut with fewest singlets. To show that this is also the maximum number of singlets from any strategy just note that the cut separates the network into two regions and the maximum number of singlets that can be created between these regions is given by the distillable entanglement. This is simply the total distillable entanglement from all of the bonds along a cut. Since I have minimized this over all of the cuts it is impossible to distill greater entanglement between the two nodes, A and B.

Note that the assisted entanglement distillation results can also be applied to networks formed from multipartite states to give an upper bound for the rate of entanglement distribution. This rate can be interpreted as an upper bound on the average number of singlets formed when only one state is available. If this were not the case it would contradict the previous optimal rate.

These results are useful in revealing how entanglement distribution behaves when vast numbers of edges are available for every bond. However, they are of limited use. The bound is only an average. This means that even if it gives a bound on the average number of singlets formed to be less than one it may still be possible to obtain a singlet with a nonzero probability. Also, for most network geometries, even the linear network case, the results do not reveal any distance scaling.

4.4 Percolation Based Restrictions for Networks of Mixed States

In quantum networks composed of bipartite mixed states there is a clear restriction imposed on the generation of entanglement between distant nodes. This is due to the Lewenstein-Sanpera decomposition of mixed states, which allows any mixed state to be expressed as a mixture of an entangled part with a separable part [151]. Specifically, in the two qubit mixed state case any mixed state, ρ can be expressed in the form

$$\rho = p \,|\, \psi\rangle \langle \psi \,| + (1-p)\rho_{sep}. \tag{4.20}$$

where $|\, \psi\rangle$ is a pure entangled state, ρ_{sep} is a separable state and $1-p$ gives the probability of the separable state. The network can now be thought of as a quantum network with each edge chosen at random to be either an entangled or separable

state. No entanglement can be distilled between regions linked solely by separable states and the probability of this can be calculated classically.

For example consider a linear network of nodes connected by m bonds that each contain n edges. This network links the nodes, A and B, that we wish to entangle. If the edges are initially mixed states that can be thought of as separable with a probability of $1-p$, then an entire bond is composed of solely separable states with a probability of $(1-p)^n$. Once this happens it becomes impossible to entangle A and B using any LOCC strategy. This could happen on any of the bonds and the probability of it happening on at least one is given by $1-(1-(1-p)^n)^m$. Hence, any protocol must on average leave a separable state between the end nodes with an increasing probability of $1-(1-(1-p)^n)^m$. This gives a decreasing bound on the average achievable entanglement, along a one dimensional network, for any protocol.

Similar arguments can be used in regular networks and gives the first application of bond percolation to the problem of entanglement distribution. Unlike the later percolation based results I will introduce, this is a negative result that reveals when long distance entanglement is impossible in a quantum network. Consider the quantum network as a classical network where each edge exists with the probability p, which corresponds to the mixed state acting entangled. Only the nodes in the same cluster can be connected by entanglement using any procedure. This is the case since no entanglement exists between two separate clusters. The size of the clusters then reveals the range over which entanglement could be distributed. When p is less than the percolation threshold the entangled states form small clusters with an infinite number of separable states spread between them. Hence, entanglement distribution is limited by the size of the cluster and long distance entanglement distribution is impossible. When p is greater than the percolation threshold the entangled states form an infinite cluster and there is no clear limit on the range over which entanglement can be distributed. This does not necessarily mean that

long distance entanglement distribution is possible. The two nodes that we wish to entangle must both be in the infinite cluster of linked entangled states and the probability of this is given by $\phi(p)^2$, with $\phi(x)$ the percolation probability. Hence, on average any protocol must leave the state, between two random nodes, as separable with a probability of at least $1 - \phi(p)^2$.

4.5 Chapter Summary

I have derived three restrictions for entanglement distribution in this chapter. The first is a necessary and sufficient condition for the generation of a perfect singlet from a bipartite quantum network. The second gives the optimal rate at which entanglement can be generated from any quantum network and the third gives a restriction on the final entanglement when the initial states are mixed. The reasons behind this last restriction are actually very similar to those employed in Ref. [63] to give a transition in the computational power of thermal states for measurement based quantum computing. Unfortunately, the mixed state restriction simply comes from the purity of the initial states and can not be applied to pure states. The requirements for entanglement distribution and specifically long distance entanglement distribution on pure state networks are still unknown. These give a few tools to analyse specific entanglement distribution tasks, however they are limited and there are still many unanswered questions. The restrictions on the state type for perfect singlet production are important to know and in the next chapter I will develop an effective strategy for long distance entanglement distribution using these states.

Chapter 5

Entanglement Percolation

In this chapter I will describe one method of producing an entangled singlet using the phenomenon of percolation. I generalized this method, previously developed for pure states, to mixed states. As part of this, I found and compared different purification protocols necessary to convert groups of mixed states shared between neighbouring nodes of the network into singlets. In addition, I will discuss protocols that only rely on local rules for the efficient connection of two remote nodes in the network via entanglement swapping.[1]

5.1 Introduction

A scheme for entanglement distribution in general networks was proposed by Acín et al. [57] in which ideas from classical bond percolation have been applied to regular (*i. e.* lattice-shaped) quantum networks. Unlike quantum repeaters this scheme makes use of the network's connectivity and allows for the generation of maximally entangled singlet states between arbitrary points of the network, with a probability that is independent of their separation. The only requirement is that the nodes are initially connected by bipartite *pure* states with sufficiently high entanglement.

[1]The material in this chapter has been published in the article, Stuart Broadfoot, Uwe Dorner and Dieter Jaksch - EPL (Europhysics Letters) **88**, 5, 50002 (2009) and Phys. Rev. A **81**, 042316 (2010).

The restriction to pure states was made since a pure, partially entangled state can be converted into a singlet with finite probability via the Procrustean method [92] which is essential for the bond percolation protocol: Initially one attempts to convert all bipartite pure states into a singlet which, in each case, succeeds with a certain probability. If this singlet conversion probability (SCP) exceeds a lattice-geometry-dependent threshold, arbitrarily large clusters of singlet-connected nodes form which can successively be connected via entanglement swapping. In this way a singlet between arbitrarily remote nodes in the network can be created. It was pointed out in [57] that this process is not optimal since certain quantum preprocessing schemes applied to the network can improve the SCP [57, 58, 59, 62, 60, 146, 61]. The standard percolation procedure is known as classical entanglement percolation (CEP) to distinguish it from these preprocessing schemes that are referred to as quantum entanglement percolation (QEP). This strategy has also been studied for complex networks [60, 146, 152]. The QEP procedures will be discussed later during chapter 7.

Clearly, the assumption of having a pure-state network is an idealization and in any practical situation the states connecting the nodes of the network will be mixed. During this chapter I will introduce my mixed state percolation scheme, which does allow the network to be composed of mixed states. In chapter 4 I gave my proof that singlet generation between two nodes is possible if and only if they are connected by at least two "paths" consisting of a particular class of states. Hence, I restrict the bipartite states in the network to this class. The aim is to create a perfect singlet between two arbitrary nodes in the network using a finite amount of resources, *i. e.* a finite number of initial states between nodes, which are converted into a singlet. This distinguishes our and other entanglement percolation schemes from, for example, the quantum repeater protocol where one aims to generate a state with high but nonunit entanglement fidelity and the number of initial states needed grows with

the distance separating the two nodes to be entangled. I make the assumption that all operations on states within a node can be performed perfectly. This assumption was previously made for Acín's pure state scheme and is a reasonable assumption to initially investigate an extension to mixed states.

I will structure the chapter as follows. I start in Sec. 5.2 by briefly summarizing the idea of classical entanglement percolation with pure states. In Sec. 5.3 I extend the concept of classical entanglement percolation to mixed states. To this end I consider regular networks where each node is connected to its neighbouring nodes by a finite number of the purifiable mixed states, introduced in chapter 4. I present two different purification protocols which are used to convert these states into a singlet with a probability above the percolation threshold of a variety of lattice geometries. After the purification, clusters of singlet-connected nodes emerge and the aim is to create a singlet between two nodes in such a cluster by successive application of entanglement swapping. By communicating classically each node can determine if singlets exist between it and its neighbouring nodes. This information can be communicated and stored classically in a central data processor. Typically one would then use this information to apply a path-finding algorithm which locates a suitable "path" of singlets before swapping operations are performed. As an alternative to this I discuss a classical and a quantum protocol which merely require classical communication between neighbouring nodes and basic computing within each node.

5.2 Entanglement Percolation with Pure States

In this section I will briefly review the use of percolation for distributing singlets in pure state networks [57, 58]. The procedure is based on classical bond percolation, where a regular lattice of nodes connected by identical quantum states, as shown in

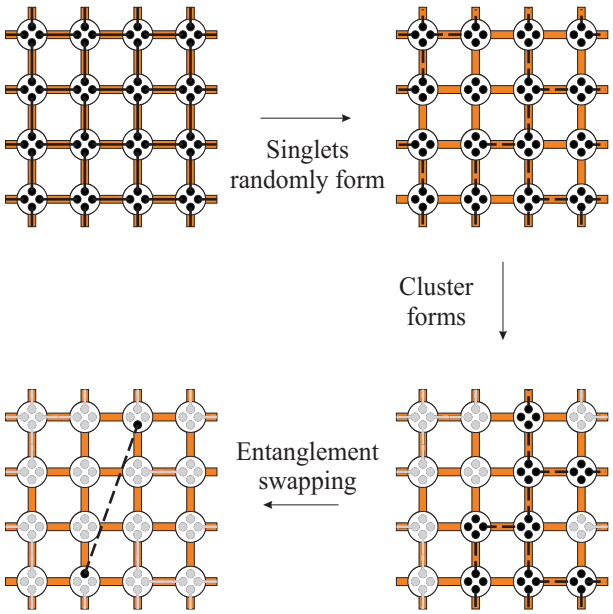

Figure 5.1: Illustration of classical entanglement percolation in a square network. Pairs of qubits (black dots) in neighbouring nodes (circles) are in identical, pure, partially entangled states (solid, black lines). The percolation scheme involves these entangled states being converted into singlets (dashed lines) with probability p. If p exceeds the percolation threshold, these form large clusters and a singlet can be obtained between any two qubits within a cluster by performing swapping operations.

Fig. 5.1, is considered. A description of classical bond percolation can be found in Ref. [100]. If the nodes are connected by pure states of the form $|\alpha\rangle$ they can be converted into singlets using the Procrustean method with a SCP of $p = 2\min(\alpha, 1-\alpha)$ (see chapter 2). These singlets act as the bond in the bond percolation model and are distributed randomly with a probability p. The set of nodes that can be connected by a path of singlets form a cluster. By using entanglement swapping (see chapter 2) a singlet can then be generated between any two nodes in the cluster. In the theoretical case of an infinitely large lattice a cluster that is infinite in extent forms if and only if $p > p_c$, where p_c is a lattice-dependent percolation threshold. This approximates the case for large but finite lattices where the threshold becomes more definitive as the size of the lattice increases. Values of p_c for a number of lattice geometries are given in Table 5.1. If each bond in a network consists of a

single pure state $|\alpha\rangle$ a threshold for α, given by $2\min(\alpha, 1-\alpha) > p_c$, can be calculated. The probability that a node belongs to the infinite cluster is the percolation probability $\phi(p)$. Two randomly chosen nodes are both part of the infinite cluster with a probability $\phi(p)^2$ and thus can be connected over an arbitrary distance.

Lattice	Threshold p_c
2D Square	0.5
2D Triangular	$2\sin(\pi/18) \approx 0.347$
2D Honeycomb	$1 - 2\sin(\pi/18) \approx 0.653$
3D Simple cubic	≈ 0.249
3D Face-centred cubic	≈ 0.120

Table 5.1: Threshold probabilities for various regular network geometries [100, 153].

5.3 Entanglement Percolation with Mixed States

It was initially unclear whether CEP was even possible with mixed states. Here, I will give the extension I developed of CEP to mixed states. I consider regular lattices, for example, triangular (see Fig. 5.2), square, or even lattices in higher dimensions. Bonds between network nodes are composed of multiple edges to satisfy the necessary condition, for forming a perfect singlet, proven in chapter 4. This restricts the edge states to those of the form (4.1) given by

$$\rho(\alpha, \gamma, \lambda) = \lambda\,|\,\alpha, \gamma\rangle\,\langle\alpha, \gamma\,|\,+\,(1-\lambda)\,|\,01\rangle\,\langle 01\,|\,, \tag{5.1}$$

where $|\,\alpha, \gamma\rangle = \sqrt{\alpha}\,|\,00\rangle + \sqrt{1-\alpha-\gamma}\,|\,11\rangle + \sqrt{\gamma}\,|\,01\rangle$ and $0 < \lambda \leq 1$. Each bond is assumed to be identical. When these bonds contain at least two states of the form (5.1) they can be converted into singlets by the pure state conversion measurement (PCM), discussed in chapter 4, followed by the Procrustean method. If the probability that a bond becomes a singlet exceeds the percolation threshold CEP

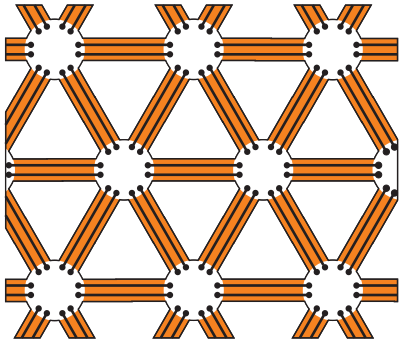

Figure 5.2: Triangular network. This is a simple 2D arrangement of PMSs in which CEP is possible.

is achieved. I will assume that the states forming edges are of the form (5.1) with $\gamma = 0$. Setting $\gamma = 0$ is not a major restriction but allows us to keep the equations manageable. All protocols presented can also be performed if $\gamma \neq 0$. I have included general equations, with $\gamma \neq 0$, for the recycling procedure introduced later (see Sec. 5.3.1) in Appendix B. I will call states of the form (5.1) with $\gamma = 0$, that is,

$$\rho(\alpha, \lambda) \equiv \rho(\alpha, \gamma = 0, \lambda), \tag{5.2}$$

purifiable mixed states (PMSs). The entangled states formed between the atomic ensembles in the DLCZ repeater are equivalent to PMSs after local X operations are performed on one of the ensembles. Unfortunately, such local operations are non-trivial in the DLCZ protocol's memories. A few extensions to the DLCZ repeater that use two-photon measurements do not require such an X gate and are reviewed in Ref. [114]. However, even in the basic DLCZ protocol the presence of one local X flip does not pose an obstacle. Two such states are still purified to a maximally entangled state, $|\Psi^+\rangle$, after a PCM operation.

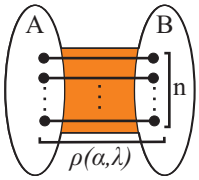

Figure 5.3: The purification setup consists of n PMSs (solid lines) shared between two nodes A and B. The aim is to distill these states into a singlet.

5.3.1 Purification Procedures

Distillable Subspace Scheme

I assume that each pair of neighbouring nodes is connected by n PMSs and our aim is to distill these into a singlet. The basic setup is shown in Fig. 5.3. To accomplish this I will use ideas proposed in Ref. [154]. Here the concept of a *distillable subspace* (DSS) is introduced as a subspace such that the local projection of the system state into this space is pure and entangled. Locating the DSS involves calculating the eigenvectors of the state with nonzero eigenvalues. To simplify notation I will represent the states at A and B using the decimal value of its binary form, *i. e.* for example $|\,00110\rangle_A\,|\,01001\rangle_B = |\,6\rangle_A^d\,|\,9\rangle_B^d$.

As an example, in the case of $n = 2$ identical states $\rho(\alpha, \lambda)$ the eigenvalues and corresponding eigenvectors are

$$\begin{aligned}
\lambda^2: \quad & \alpha\,|\,0\rangle_A^d\,|\,0\rangle_B^d + \sqrt{\alpha(1-\alpha)}\,|\,1\rangle_A^d\,|\,1\rangle_B^d + \\
& \sqrt{\alpha(1-\alpha)}\,|\,2\rangle_A^d\,|\,2\rangle_B^d + (1-\alpha)\,|\,3\rangle_A^d\,|\,3\rangle_B^d\,, \\
\lambda(1-\lambda): \quad & \sqrt{\alpha}\,|\,0\rangle_A^d\,|\,2\rangle_B^d + \sqrt{1-\alpha}\,|\,1\rangle_A^d\,|\,3\rangle_B^d\,, \\
\lambda(1-\lambda): \quad & \sqrt{\alpha}\,|\,0\rangle_A^d\,|\,1\rangle_B^d + \sqrt{1-\alpha}\,|\,2\rangle_A^d\,|\,3\rangle_B^d\,, \\
(1-\lambda)^2: \quad & |\,0\rangle_A^d\,|\,3\rangle_B^d\,. \qquad (5.3)
\end{aligned}$$

If this is acted on by the projective measurement $|\,1\rangle_A^d\,\langle 1\,| + |\,2\rangle_A^d\,\langle 2\,|$ at A and

$|\,1\rangle_B^d\,\langle 1\,| + |\,2\rangle_B^d\,\langle 2\,|$ at B the state remaining is $(|\,1\rangle_A^d\,|\,1\rangle_B^d + |\,2\rangle_A^d\,|\,2\rangle_B^d)/\sqrt{2}$. Both of these projective measurements only occur with probability

$$p_{n=2} = 2\lambda^2\alpha(1-\alpha). \tag{5.4}$$

For this example there is no choice between entangled states to project out and if the original states are the same a maximally entangled state is automatically obtained. For states that are not identical this does not need to be the case.

An extension of this scheme to n identical copies of PMSs $\rho(\alpha,\lambda)$ yields the SCP

$$\begin{aligned} p_n = &\sum_{m=0}^{n} \lambda^{n-m}(1-\lambda)^m \binom{n}{m} \\ &\times \left(\sum_{k=1}^{n-m-1} \frac{\alpha^{n-m-k}(1-\alpha)^k \binom{n-m}{k}\left(\binom{n-m}{k}-1\right)}{\binom{n}{k}-1} \right). \end{aligned} \tag{5.5}$$

A derivation of this formula is given in Appendix C. As a particular example it is worthwhile to discuss the case of three states in more detail. In this case the measurement at A is given by a positive operator valued measure (POVM) with the elements,

$$\begin{aligned} &(|\,0\rangle_A^d\,\langle 0\,| + |\,7\rangle_A^d\,\langle 7\,|), \\ &(|\,1\rangle_A^d\,\langle 1\,| + |\,2\rangle_A^d\,\langle 2\,|)/2, \\ &(|\,1\rangle_A^d\,\langle 1\,| + |\,4\rangle_A^d\,\langle 4\,|)/2, \\ &(|\,2\rangle_A^d\,\langle 2\,| + |\,4\rangle_A^d\,\langle 4\,|)/2, \\ &(|\,3\rangle_A^d\,\langle 3\,| + |\,5\rangle_A^d\,\langle 5\,|)/2, \\ &(|\,3\rangle_A^d\,\langle 3\,| + |\,6\rangle_A^d\,\langle 6\,|)/2, \\ &(|\,5\rangle_A^d\,\langle 5\,| + |\,6\rangle_A^d\,\langle 6\,|)/2. \end{aligned} \tag{5.6}$$

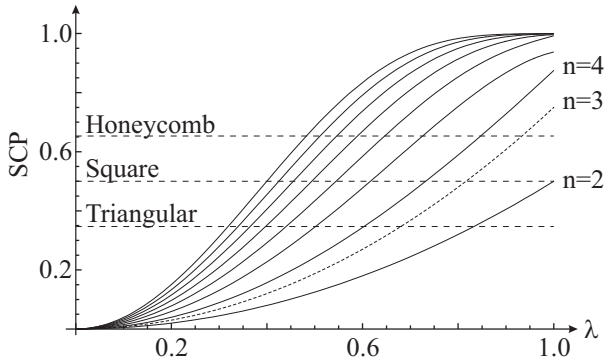

Figure 5.4: Singlet conversion probability for n-edged bonds using the recycling scheme for $\alpha = 1/2$ and $n = 2, (3), 4, 6, 8, 10, 12, 14, 16$ (bottom to top). The $n = 3$ line (dashed) corresponds to the DSS scheme. The percolation thresholds for triangular (T), square (S), and honeycomb (H) lattices are given by the horizontal lines.

The measurement at B then depends on this outcome and creates a maximally entangled state with a certain probability. The SCP is obtained by setting $n = 3$ in Eq. (5.5) and is given by

$$p_{n=3} = 3\lambda^2\alpha(1-\alpha). \tag{5.7}$$

Comparing this with the $n = 2$ case [*cf.* Eq. (5.4)] shows an increase in the success probability which can be seen in Fig. 5.4, where the dashed line represents the SCP for three identical states.

Recycling scheme

The SCP using the DSS scheme does generally increase with increasing n. However, the scheme does not make use of the available resources in the best way. Indeed, the SCP p_n can be significantly improved by grouping n identical PMSs into sets of m and converting each of these sets into a singlet. For example, for $m = 2$ a PCM is applied on pairs of states which converts them into singlets with a probability given by Eq. (4.5). If this fails for a given pair both measured qubits may still be found in the state $|\,0\rangle$ and have generated another PMS. This PMS can then be used

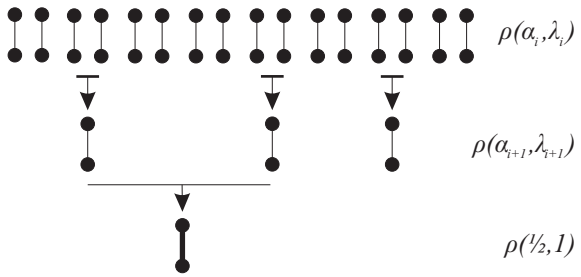

Figure 5.5: The recycling scheme consists of splitting the states into pairs that are then purified. If no singlets are successfully produced some of the states may still have been transformed into PMSs and given enough of these the process can be repeated.

again in another purification attempt. To be more precise, starting with n copies of a state $\rho(\alpha, \lambda)$ (with $\alpha \geq 1/2$) I apply a 2-state purification protocol on groups of two. If no singlet is obtained the procedure is repeated on the remaining PMSs as illustrated in Fig. 5.5. The coefficients for the PMSs after k repetitions, when no singlet is created, are given by

$$\alpha_k = \frac{\alpha_{k-1}^2}{1 - 2\alpha_{k-1} + 2\alpha_{k-1}^2}, \tag{5.8}$$

$$\lambda_k = \frac{\lambda_{k-1}^2(1 - 2\alpha_{k-1} + 2\alpha_{k-1}^2)}{1 - 2\lambda_{k-1} + 2\lambda_{k-1}^2(1 - \alpha_{k-1} + \alpha_{k-1}^2)}, \tag{5.9}$$

where $\alpha_0 = \alpha$ and $\lambda_0 = \lambda$. For states of the form $\rho(\alpha_k, \lambda_k) \otimes \rho(\alpha_k, \lambda_k)$ the probability of obtaining a PMS is $c_k = 1 - 2\lambda_k + 2(1 - \alpha_k + \alpha_k^2)\lambda_k^2$. If the PCM yields two qubits that are measured in different states the purification step between the two PMSs has completely failed. The probability of this is given by $f_k = 2\lambda_k(1 - \lambda_k)$. The probability of not generating a singlet using this *recycling protocol* on n states of the form $\rho(\alpha_i, \lambda_i)$ is then found to be

$$F_n(i) = \sum_{k=0}^{\lfloor \frac{n}{2} \rfloor} \binom{\lfloor \frac{n}{2} \rfloor}{k} f_i^{\lfloor \frac{n}{2} \rfloor - k} c_i^k F_k(i+1), \tag{5.10}$$

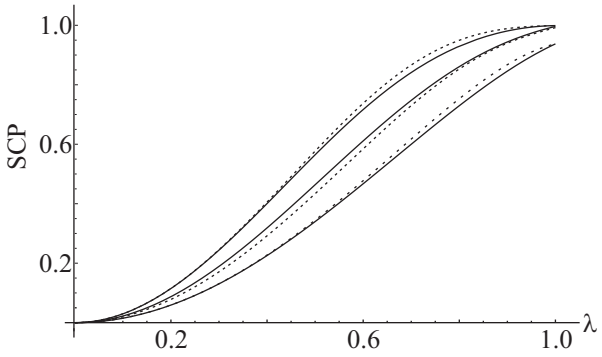

Figure 5.6: Success probabilities for the recycling schemes that split the states into pairs (dashed lines) and sets of three (solid lines). Shown are the SCPs for 6, 9 and 12 initial states (bottom to top) for $\alpha = 1/2$.

where $F_0(i) = 1$ and $\lfloor x \rfloor$ returns the value of x rounded down to the nearest integer. Consequently, the probability of successfully generating a singlet by applying the procedure to n states of the form $\rho(\alpha, \lambda)$ is $1 - F_n(0)$ which is calculated iteratively. Examples are shown in Fig. 5.4 for $\alpha = 1/2$.

Obviously, the states do not necessarily need to be split into pairs. For example, all of the states can be separated into sets of three and then the three-state DSS purification applied. In case of failure this can yield a PMS state as well, which can then be used in later purification steps. There are a variety of ways to combine the three-state purification with the two-state recycling scheme. Here I concentrate on the straightforward approach which only uses the three-state purification on every level of the recycling scheme. The results are shown in Fig. 5.6. As can be seen in most cases the two-state recycling scheme has a higher chance of success and because of this I will focus on the pairing arrangement.

5.3.2 Percolation Thresholds

Using the purification procedures described above I can apply CEP, as described in Sec. 5.2, for lattice networks with multiedged bonds. In most cases it is advantageous

to use the two-state recycling scheme, except for $n = 3$ where the DSS scheme should be used. From Fig. 5.4 it can be seen that the SCP increases with the number of edges per bond and this allows for a larger range of values for λ and α such that CEP is successful. For double-edged bonds the optimal probability of generating a singlet was shown in Ref. [148] to be given by

$$0 \leq 2\lambda^2\alpha(1-\alpha) \leq 1/2. \tag{5.11}$$

When the bonds are composed of three edges (*i. e.* , three PMSs between nodes), my protocol will generate a singlet with a probability of

$$0 \leq 3\lambda^2\alpha(1-\alpha) \leq 3/4. \tag{5.12}$$

By comparing these ranges to the percolation thresholds it can be seen that a basic successful setup is a double bonded triangular lattice (see Fig. 5.2). The double bonds can be converted to singlets and if the chance of this is larger than the percolation threshold an infinite cluster will form. A singlet can then be created between any two nodes within the cluster. Thus, percolation occurs if

$$2\lambda^2\alpha(1-\alpha) > 2\sin(\pi/18) \approx 0.347. \tag{5.13}$$

However, the singlet conversion probability never exceeds 1/2 for two states. Therefore, more states are required in other geometries. For example, if there are three-edged bonds between each neighbouring node then CEP can be applied to a square lattice. This is because there are parameters such that $3\lambda^2\alpha(1-\alpha) > 1/2$. Analogously, CEP is also possible in honeycomb lattices with three edges per bond.

5.3.3 Local Processing Strategies

The process of creating singlets, randomly replacing the initial network bonds, can be run if each node can only communicate classically with their neighbours. Each node then knows if a qubit that it contains is part of a singlet after this procedure has finished. This information can be stored classically within a node but after the bonds are distilled there is the problem of finding a set of singlets that connect the requested nodes, A and B.

If all of the singlet generation data is collected by a "controller" then an efficient pathfinding algorithm can be applied to determine a suitable "path" of singlets linking the nodes. An example of a suitable algorithm would be a Dijkstra scheme [144] such as the A* pathfinding algorithm [155]. The path information can then be used to instruct the correct nodes to perform swapping. The swapping operations are performed in order from node A to B, so that the measurement outcomes only need to be communicated along the chain, between neighbouring nodes. However, this procedure requires one classical computer to have complete knowledge of the network. Instead, it is interesting to note that this does not need to be the case as there are algorithms which do not require any more classical communication than this "controller" method; indeed, they do not require a central "controller" at all. This can be done not only classically but also via a quantum algorithm using multipartite entanglement which I will introduce below.

A classical pathfinding method would use a type of breadth-first search algorithm called a burning algorithm [156]. Node A sends a "burning" signal to its neighbouring nodes connected by singlets. These nodes keep a record of where they received the signal from and send out an identical signal to the other nodes to which they are connected to. I will say that the node has "burned". If it has already received a signal from a different node then the additional signal is ignored. This

continues outwards from A, "burning" the nodes. Once node B receives the signal it replies to the node it came from with a "swapping" message. This node can then perform a swapping operation and send another "swapping" signal, together with the Bell-measurement outcome, back to the node from which it received a "burning" signal. The path can then be traced back along the nodes with swapping performed at each step until node A is reached. Both A and B can determine if the protocol has been successful. However, A and B may not be in the same cluster and they do not know if the protocol has failed when the network is of infinite size. This is not a problem for finite networks, containing N nodes, as A and B can time the steps taken and if these exceed $2(N-1)$ they both know they are not in the same cluster.

Note that no extra information actually needs to be transmitted. It is possible to combine the burning algorithm with the process of transmitting the purification protocol information. For example, in a double-edged network of identical edges, A can perform her PCM and if $|1\rangle$ is the outcome she assumes she has a singlet and sends a burning signal to the node that would contain the singlet's other qubit. If a node receives this signal it can perform its PCM and determine if there is a singlet there. When there is and if it is the first instance for the node it should record that entry qubit and repeat the process, performing a PCM on the remaining qubits and sending signals to those with the $|1\rangle$ outcome. Once B receives a signal it can check that a singlet has been created with a PCM and then send a swapping signal back as before. During the swapping, a node can use the Bell-measurement information received to indicate that a swapping is required so no explicit "swapping" signal is required either. All of this information transfer would have been necessary as well if a controller algorithm would have been used. Hence the generation of the singlet can be accomplished by defining rules for each node and allowing them to run with nearest-neighbour classical communication. This is fundamentally different to the controller process and has made use of parallel computation to find a path of which

no single node has full knowledge.

I will now consider an alternative, quantum algorithm that is based on the burning algorithm and makes use of multipartite entanglement in the network. The protocol starts after an attempt to convert all bonds into singlets and every node has knowledge about its singlet connections to nearest neighbours. I build up a progressively larger multiqubit GHZ state, defined by $|\,\mathrm{GHZ}_n\rangle = (|\,0\rangle_1 ... |\,0\rangle_n + |\,1\rangle_1 ... |\,1\rangle_n)/\sqrt{2}$, spread between the "burned" nodes by adding qubits in each burning step. Building up such a state requires joining two GHZ states, $|\,\mathrm{GHZ}_n\rangle$ and $|\,\mathrm{GHZ}_m\rangle$, to create $|\,\mathrm{GHZ}_{n+m-1}\rangle$ (note that a singlet equals $|\,\mathrm{GHZ}_2\rangle$). This is done by performing a CNOT gate between a qubit in $|\,\mathrm{GHZ}_n\rangle$ and a target qubit in $|\,\mathrm{GHZ}_m\rangle$, measuring the target qubit in the Z-basis, communicating the measurement result to the other qubits in $|\,\mathrm{GHZ}_m\rangle$ and performing a unitary operation on them depending on the outcome. Now I perform the same process as for the "burning algorithm", however, as each node is "burned" it is connected to the GHZ state spread over the previously burned nodes. The process to do this is illustrated in Fig. 5.7 and consists of joining the singlets partially contained in that node to the GHZ state. Within each node one qubit is left entangled with the GHZ state. After this operation has been run for a maximum of $N-1$ times all of the nodes in the cluster containing A have a qubit from a single GHZ state.

At each node a record is kept of the bond via which it has been included into the GHZ state. If there is a singlet between two nodes that are being burned then the singlet is ignored. Furthermore, I add the rule that whenever a node can not extend the GHZ state, X-basis measurements are performed along the recorded path back to A. This removes a qubit from the GHZ state but introduces a phase error in the remaining GHZ state depending on the outcomes of the measurement. The information about these measurement outcomes has to be sent back along the path to A. Whenever the route back branches, the measurement outcome is sent

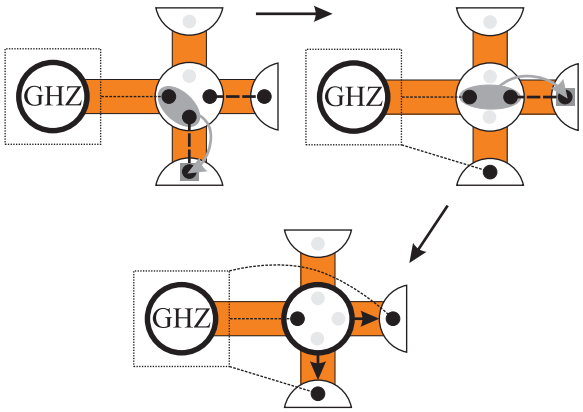

Figure 5.7: Procedure to join a node's singlets onto a GHZ state. Here the GHZ state is represented by a dotted box. Additional qubits (black dots) that are a part of the GHZ state are linked to the dotted box by a dotted line. A CNOT gate and measurement (both are represented by a shaded oval) are performed between the qubit already in the GHZ state and those that are part of a singlet (dashed lines). Each measurement outcome needs to be sent (gray arrow) to the other singlet qubit to perform a local unitary (shaded square). This extends the GHZ state to include qubits connected by edges to the node being attached. Once this has occurred for each qubit in a singlet the process is repeated by sending out a signal to repeat the step at each node that was linked by a singlet.

in one way and a message corresponding to "no phase error occurrence" is sent to the others. At each node the returning process is paused until all of the bonds to which it sent a burning signal to provide it with the phase information. At nodes A and B no X measurement is performed. Finally after A receives all of the phase information a phase correction can be performed and a singlet between A and B is obtained. In Fig. 5.8 an example is given to illustrate the protocol.

In the example described both burning algorithm schemes leave a singlet entangled. However, each scheme has different advantages. Unlike my first burning algorithm, the alternative multipartite burning algorithm has the advantage that it has a chance to form any multipartite GHZ state. The first protocol described is aimed at only generating singlet states. The advantages of the first scheme are that it does not make use of all of the entanglement in the network and avoids generating

a decoherence prone GHZ state over the entire network.

5.4 Chapter Summary

I have demonstrated that within lattice networks, where the nodes are connected by multiple bipartite mixed states, percolation strategies can be applied for distributing entanglement. This is reliant on the states being PMSs, which can arise as a result of sending one qubit from a singlet through an amplitude damping channel. States that are equivalent, upto local unitaries, are also observed in the DLCZ repeater scheme. To implement the percolation strategies I have introduced some new purification protocols designed to maintain the form of these states or generate singlets. Since I have shown that classical entanglement percolation is only possible for a specific class of bipartite states, entanglement distribution in a network which is subject to more general forms of noise needs to make use of other methods. These will not produce perfectly entangled states, however, the resulting state fidelity may be independent of distance and sufficient for purification. One strategy for this will be the topic of the next chapter.

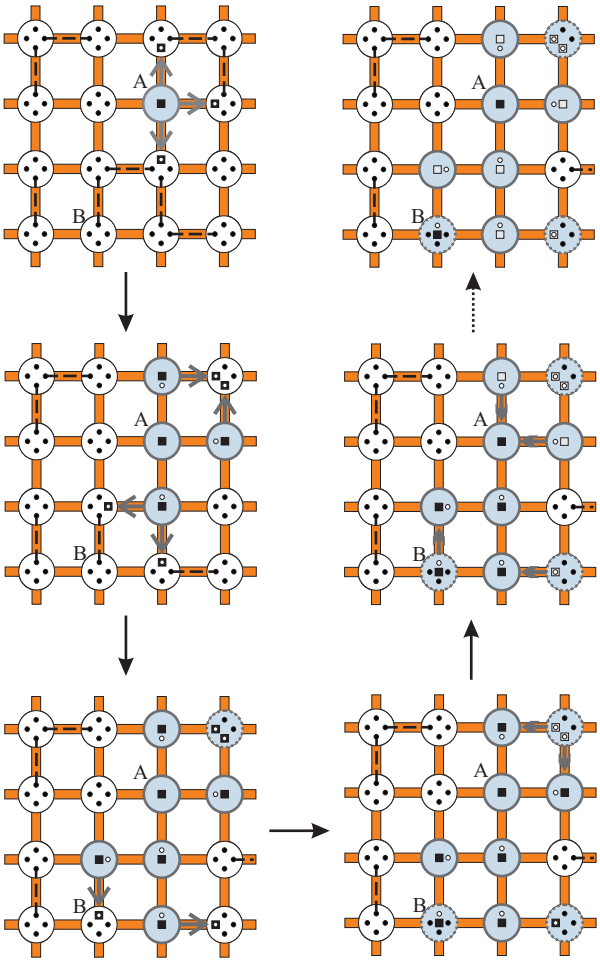

Figure 5.8: After the singlets are formed a GHZ state can be extended from node A. This procedure uses the operation shown in Fig. 5.7 to add qubits to the GHZ state. The black squares depict qubits that are part of the GHZ state. Arrows represent a message to add nodes to the GHZ state along singlet paths. Each node keeps a record of the node from which it received this message from, symbolized here by a white dot. When a node cannot extend the GHZ state any further (highlighted by a dashed outline) it measures its qubits in the X-basis (open squares) and sends this information back toward A (thin arrows) along the route recorded. Certain nodes are selected beforehand not to perform the measurement (here A and B) and these will form the resulting GHZ state. At each node the incoming data can be combined and sent back along one path if the routes branch. Once this data returns to A a phase operation can be performed on the qubit there to correct for any errors and the final GHZ state (here a singlet between A and B) will remain.

Chapter 6

Global Error Correction

During this chapter I will explain another method of distance-independent entanglement distribution developed after percolation, that works on networks composed of binary states, *i. e.* rank two states that are mixtures of two bell states. I give my generalization of this method that can be applied to any network geometry. By using this method and combining it with the concept of percolation I also show that the generation of long distance entanglement is possible with rank three states.[1]

6.1 Introduction

For the generation of a perfect singlet between two network nodes, using finite resources, I have shown that the states in the network must be of a particular rank two form. I have also given a method that allows this to be accomplished over an arbitrary distance, with finite local resources, via percolation. However, the states required are still restrictive and any other noise causes an exponential degradation of the resulting singlet with swapping steps. It would be beneficial to find other protocols that allow for long distance entanglement distribution but with a broader range of initial states. My necessary condition removes the possibility that a perfect singlet would result when other states are used but it is still possible that highly

[1]The material in this chapter has been published in the article, Stuart Broadfoot, Uwe Dorner and Dieter Jaksch - Phys. Rev. A **82**, 042326 (2010).

entangled mixed states can be generated over a long distance. After I introduced my percolation procedure other schemes have been proposed that generate highly entangled states from a regular 2D square network made of rank two mixtures of bell states [64]. These states are called "binary states" [48]. Here, if the amount of entanglement in the binary states exceeds a threshold, the network is transformed into an entangled state that can stretch over an arbitrary distance, while maintaining a nonmaximal but constant entanglement. My previous percolation protocol [65, 66], as well as the scheme described in Ref. [64], requires states of rank two, or less, for long distance entanglement generation using constant local resources.

In this chapter I extend these ideas to obtain a "global error correction" procedure that can be applied to quantum networks that have arbitrary geometry and are composed of binary states. By combining it with quantum state percolation I show that entanglement can be efficiently generated over long distances by using a constant number of *rank three* states between each node. The final fidelity being independent of the distance.

The chapter is structured as follows. In Sec. 6.2 I develop a generalized form of global error correction. This scheme works on binary states and in Sec. 6.3 I will give a way of generating these binary states from rank three states. I will prove a restriction on the types of states that can be distilled into binary states. These capabilities are then combined to enable long distance entanglement distribution with rank three states. Requirements for the scheme are calculated and compared with numerical results.

6.2 Global Error Correction

In this section I devise a global error correction method that performs local measurements and, by combining the results, obtains information on the error locations

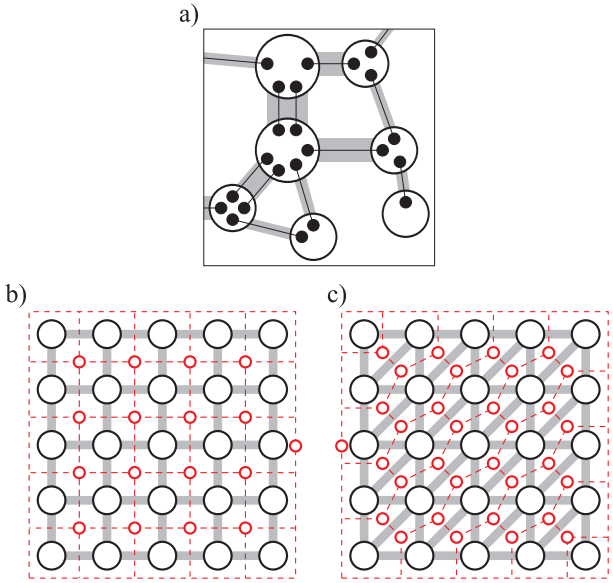

Figure 6.1: (a) A quantum network composed of nodes (large open circles) that contain qubits (filled circles). Each qubit is initially entangled with another (thin black lines) and these two-qubit states form the edges that are contained within each bond (thick grey lines). (b) A 5x5 node square network with its dual network. Individual edges and qubits are not shown. However, dual nodes are presented as small open (red) circles connected by dashed lines, including the network exterior (dashed square with small circle). (c) A 5x5 node triangular network with its honeycomb dual network.

within the quantum network (see Fig. 6.1). This information does not allow the errors to be located exactly but, as I will show, does allow the errors to be subdued so entanglement can be created between distant nodes. Note that, throughout, I assume that the measurements and operations act perfectly.

I consider the entire network as a mixture of pure states and analyse the protocol acting on each of these using the stabilizer formalism [17]. From these results I can then determine the mixed state produced. To begin, lets construct the network's initial state using the states of individual edges. Each of these initial two-qubit edge states can be transformed into a probabilistic mixture of Bell states [42], via LOCC. This allows us to assume that each edge is in one of the four Bell states that I introduced in Eq. 2.3. In this chapter I will introduce a new notation for the Bell

states, with

$$|\psi_{ab}\rangle = (X^a Z^b \otimes I)(|00\rangle + |11\rangle)/\sqrt{2}, \tag{6.1}$$

where $a, b \in \{0, 1\}$. A stabilizer generated by $\left\{(-1)^a Z \otimes Z, (-1)^b X \otimes X\right\}$ can describe each Bell state and the probability of having that state can be labelled as p_{ab}. For a network that contains N_E of these identical edges, and $N_Q = 2N_E$ qubits, the whole state will have the form

$$\begin{aligned}\rho_I &= \sum_{\{b_i\}} \sum_{\{a_i\}} \prod_{i=1}^{N_E} p_{a_i b_i} |\psi_{a_i b_i}\rangle \langle\psi_{a_i b_i}| \\ &= \sum_{\{b_i\}} \sum_{\{a_i\}} P(\{a_i\}, \{b_i\}) \rho_{\{a_i\},\{b_i\}},\end{aligned} \tag{6.2}$$

where each edge, i, has parameters $a_i \in \{0, 1\}$ and $b_i \in \{0, 1\}$. The summations are over all values that these can take and give a mixture of pure states

$$\rho_{\{a_i\},\{b_i\}} = \prod_{i=1}^{N_E} |\psi_{a_i b_i}\rangle \langle\psi_{a_i b_i}|, \tag{6.3}$$

which occur with probability

$$P(\{a_i\}, \{b_i\}) = \prod_{i=1}^{N_E} p_{a_i b_i}. \tag{6.4}$$

The error model considered has independent bit-flip and phase-flip errors. For this case the pure states that contribute to the mixture can be thought of as networks of error free singlet states, $|\psi_{00}\rangle$, on which errors randomly occur. A bit-flip error that causes $a \to 1$ occurs with probability p_x. Similarly, phase-flip errors cause $b \to 1$ and have a probability of p_z. This situation is equivalent to having edges with the values $p_{00} = (1 - p_x)(1 - p_z)$, $p_{01} = (1 - p_x)p_z$, $p_{10} = (1 - p_z)p_x$, and $p_{11} = p_x p_z$ and

it simplifies the probability of each state $\rho_{\{a_i\},\{b_i\}}$ to become

$$P(\{a_i\},\{b_i\}) = p_x^{N_X}(1-p_x)^{N_E-N_X} \times p_z^{N_Z}(1-p_z)^{N_E-N_Z}, \tag{6.5}$$

with N_X and N_Z giving the number of bit-flip and phase-flip errors on the state, respectively,

$$N_X = \sum_{i=1}^{N_E} a_i, \quad N_Z = \sum_{i=1}^{N_E} b_i. \tag{6.6}$$

Now the global error correction procedure is applied to one of these pure states, each of which can be described using a stabilizer that is formed by the union of Bell state stabilizers. The procedure extracts information by performing $Z \otimes Z$ measurements locally on nodes along a closed path of edges, as illustrated in Fig. 6.2. Such paths are referred to as "loops" and contain edges from the set loop $= \{l_1, l_2, ...l_{N_L}\}$, where the $l_1, l_2...$ give the index of each of the N_L edges forming the loop. These measurements take -1 and 1 as possible values. The product of the measurement results around a loop is labelled $(-1)^{L_{\text{loop}}}$. Here L_{loop} gives the bit-flip error parity around the loop, $L_{\text{loop}} = \left(\sum_{i\in\text{loop}} a_i\right) mod\, 2$. Each value of L_{loop} gives us information on the errors that can then be used. As the measurements are made the stabilizer follows the rules given in Ref. [17]. After each measurement the stabilizer generator is manipulated so that at most one element anti-commutes with the measurement operator and the measurement operator, multiplied by the outcome, is then substituted in place

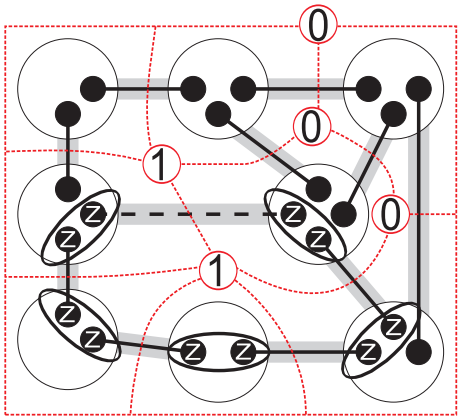

Figure 6.2: One possible pure state network $\rho_{\{a_i\},\{b_i\}}$ from the ensemble given by Eq. (6.2). Each node (open circles) contains qubits (filled circles) that are part of two qubit entangled states (thin lines) and edges are located in bonds (thick grey lines). For $a = 0$ the edge line is solid, and for $a = 1$ it is dashed. $Z \otimes Z$ measurement operations are carried out within each node (black ovals) around one plaquette. This allows a value of L_{loop} to be associated with each plaquette. The dual network (dashed red lines) is shown with these values contained within each dual node (dashed red circles). The dual vertex representing the exterior is represented by a dashed red box.

of the anti-commuting element. If the operator does not anti-commute with any elements in the stabilizer then nothing is changed.

Each measurement of the operator $Z \otimes Z$ yields $(-1)^{m_j}$ $(m_j \in \{0, 1\})$ and these measurements are performed between every pairing of qubits, that are inside the same node. By making these measurements the quantity $L_{\text{loop}} = \left(\sum_{i \in \text{loop}} m_i\right) mod\, 2$ can be calculated for all of the smallest possible loops in the network, which I refer to as plaquettes, and can then deduce L_{loop} for any loop. I do not need to perform the actual measurement between every qubit pair in a node because some of the $Z \otimes Z$ operators will be products of previously measured $Z \otimes Z$ operators. From the state $\rho_{\{a_i\},\{b_i\}}$ these measurements result in a state given by a stabilizer that has generators $(-1)^{N_Z}(X^{\otimes N_Q})$, $(-1)^{a_i}(Z \otimes Z)$ for every edge, i, and operators $(-1)^{m_j}(Z \otimes Z)$ for every measurement j.

All of the plaquettes in the network can then be assigned their values of L_{loop}. Values of one can be considered defects on nodes in the dual network (see Fig. 6.2).

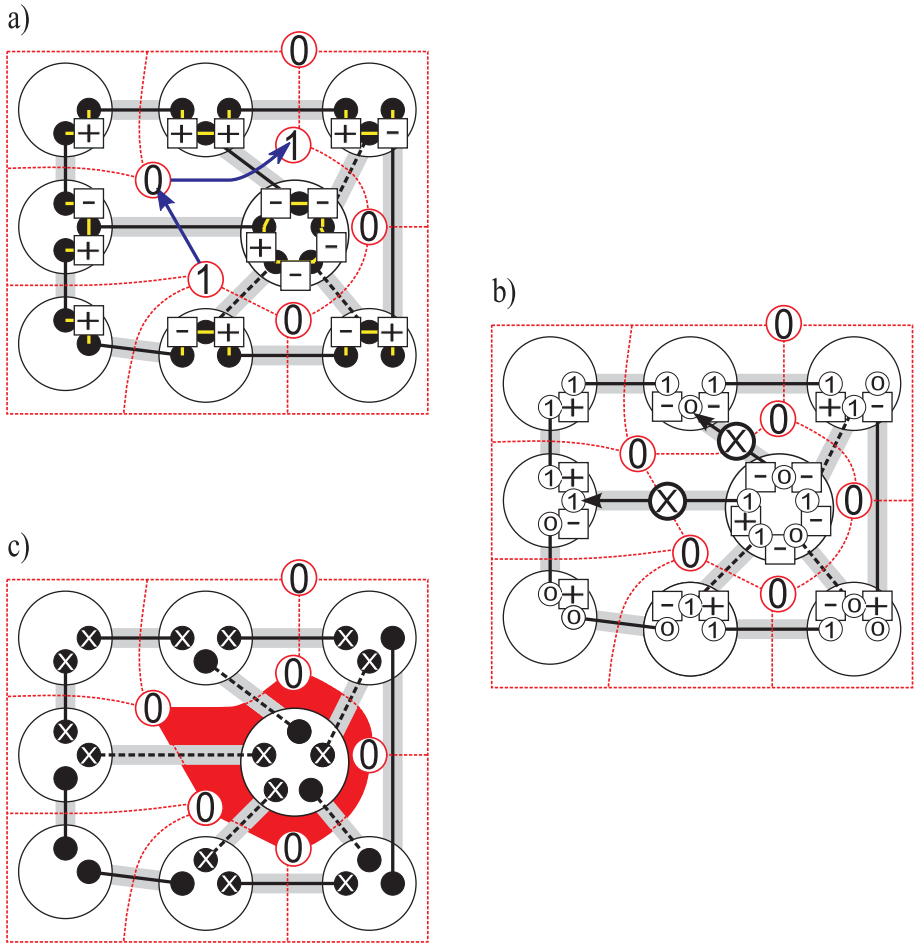

Figure 6.3: (a) A single-edged network is shown where three edge errors have occurred (dashed black lines). The local $Z \otimes Z$ measurement outcomes are displayed inside boxes, with '$\pm$' referring to a $(-1)^{m_j} = \pm 1$ eigenstate. Around each plaquette the values of L_{loop} are then calculated and shown on the dual network nodes (dashed red circles linked by dotted red lines). Values of 1 are defects and are matched together along a path (blue arrows). (b) Edge errors are assumed to lie across the matching path and X gates are applied to one qubit within each of these edges (black arrows). This "flips" ($+ \leftrightarrow -$) some of the local measurement outcomes. Each qubit can then be put into two groups (labelled '0' and '1') using the measurement outcomes (a minus sign means the groups need to be different for the two qubits), and qubits that are in a network edge are put in the same group. To assign the values we pick an initial qubit and value at random and then assign values in all remaining qubits. (c) X gates are applied to one group (nodes containing white crosses) and for each pure ensemble state a GHZ state is created with patches (shaded red area) of bit-flip errors. These occur where the actual edge error path differed from the assumed path.

These defects occur in pairs. A chain of errors, $a_i = 1$, on the quantum network's edges separates the dual node defects in each pair (see Fig.6.3(a)). These error affected edges must cross a path of dual network edges that connect the two defects. Hence, we can obtain information on the location of bit-flip errors by pairing the defects, in a matching problem. I assume that the length of the paths is minimal, since longer paths require more errors, and this is unlikely when p_x is small. This gives a minimum weight matching problem to be solved [157] in an analogous way to the correction methods used in surface codes [86, 87, 88]. By doing so we find the most likely defect pairs to be linked by a path of errors. The actual path is assumed to be the one of the shortest distance, that is, the smallest number of edges, linking the defects in the dual network (see Fig.6.3(a)). Sometimes more than one such path exists. Later, we will see that it is the gap between the assumed paths and actual paths that lead to errors in this protocol. Hence, we wish to minimize the number of nodes between the true path and the assumed path. This can easily be done in regular networks, by using paths that approximately follow straight lines, but for simplicity, in the general case it is sufficient to choose one of the shortest paths at random. One qubit in each network edge that lies along the assumed paths is then acted on with an X gate. We can actually avoid performing these X gates until the very end when there may be fewer qubits to apply gates on. Here I include the gates at this stage for clarity. When these gates are applied to a qubit the value of m_j changes to $1 - m_j$ for each measurement pairing that includes those qubits (see Fig.6.3(b)). This gives $m_j = 1$ for an even number of times around every loop and by acting around every loop with X gates we can force $m_j = 0$ for every local qubit pairing. A procedure for accomplishing this task is given in Fig.6.3(b-c). Once this is done the resulting stabilizer will have generators $(-1)^{N_Z} X^{\otimes N_E}$, $(-1)^{a'_i} Z \otimes Z$ for every edge, i, and $Z \otimes Z$ from every local pairing of qubits. The a_i values have been changed to a'_i after performing the X gates. These a'_i values are unknown,

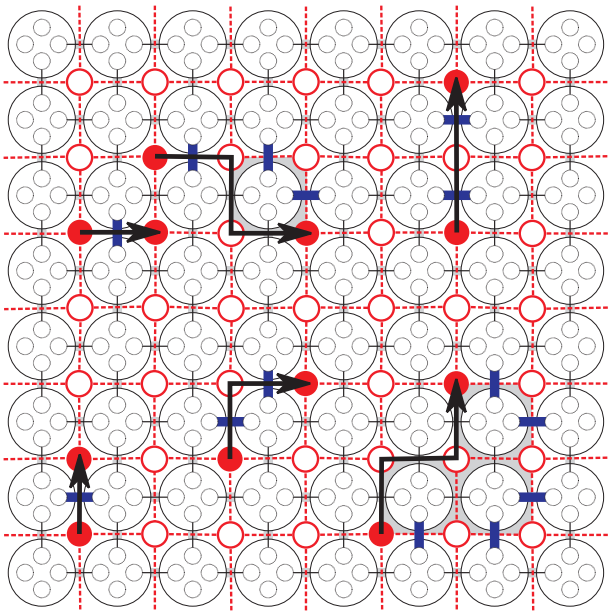

Figure 6.4: Regular square network formed by single edged bonds. The dual lattice is shown by (red) dashes and includes the error syndromes on the dual vertices (small red circles; $L_{\text{loop}} = 1$, filled; $L_{\text{loop}} = 0$, outlined). The edge errors causing these plaquette errors are shown by thick (blue) bars. The error syndromes are matched together (black arrows), and this can be used to give the most likely edge error locations for the recorded measurement syndrome. The shaded (grey) areas between the assumed error locations and the actual edge errors identify groups of nodes. For this particular pure state in the ensemble a GHZ state is obtained, with X errors present on the qubits within these nodes. In practice the initial state is unknown and hence do not know the location and size of the shaded (grey) patches, but for the regions to become larger, more errors are required and hence are less likely.

however all of the dual edges that cross edges with $a'_i = 1$ must form loops on the dual network. This stabilizer describes a pure GHZ state that has had N_Z Z operators acting on it and X operators acting on all the qubits within some nodes. These affected nodes are within loops on the dual network and appear as patches (see Fig. 6.4). The X gates that remain when the procedure is run on an initial configuration $\{a_i\}$ are described by an operator $X_P(\{a_i\})$, which applies X gates on the qubits that lie within patches. The whole procedure will result in a mixture of

these pure states,

$$\rho_F = \sum_{\{b_i\},\{a_i\}} p_z^{N_Z}(1-p_z)^{N_E-N_Z} P(\{a_i\} \mid \{m_j\}) \times X_P(\{a_i\}) Z^{N_Z} \rho_{\mathrm{GHZ}} Z^{N_Z} X_P(\{a_i\}), \tag{6.7}$$

where Z acts on an arbitrary qubit and $P(\{a_i\} \mid \{m_j\})$ is the probability of the initial error configuration being $\{a_i\}$ given the results of the measurements.

Larger patches require more errors and are less likely to occur. Hence, for low values of p_x the most probable case is that finite sized patches, containing a small number of nodes, occur randomly. I quantify the probability of a random node existing in a patch as P_X, which has the same value throughout the network. Later, when I select nodes to connect with entanglement, I assume that each exists in a patch with a probability of P_X. This makes the assumption that the nodes are sufficiently separated that these probabilities are independent. This is a reasonable assumption since we are primarily interested in the long range entanglement and for shorter separations the extra correlations are beneficial towards the resulting entanglement. For high values of p_x the likely number of errors increases so that it becomes impossible to match the defects up correctly and accurately guess the paths. Within infinite networks there exists a critical value of p_x below which patches almost certainly exist and long distance entanglement can be generated. Above the critical value this is not possible and $P_X = 1/2$ for the most likely pure states. Here, P_X is only calculated numerically and I will not analyze the relationship between P_X and p_x analytically.

When it is highly likely that patches will form the resulting mixed state can be cut back to an impure GHZ state, with any number of qubits up to N_Q, by removing qubits with X measurements and, depending on their outcomes, applying

a correcting Z operation on one of the qubits to be kept. The final fidelity, that is, overlap with a pure GHZ state, is dependent on p_x and decreases for more qubits in the resulting state. It is, however, still independent of the distance between the qubits. In particular, we can remove all of the qubits except two leaving a two-qubit entangled state spread between two nodes. For each pure state, contributing to the mixture in Eq. (6.7), after removing the qubits, an ideal singlet is obtained when the remaining qubits are either both in an error affected patch or outside of them (see Fig. 6.5). The pure state $\rho_{\{a_i\},\{b_i\}}$ is transformed to the state $\rho_c(\{b_i\},\{a_i\})$, which has the form

$$\begin{aligned}\rho_c =&(P_X^2+(1-P_X)^2)\frac{(1+(1-2p_z)^{N_E})}{2}\left|\psi_{00}\right\rangle\left\langle\psi_{00}\right| \\ &+2P_X(1-P_X)\frac{(1+(1-2p_z)^{N_E})}{2}\left|\psi_{10}\right\rangle\left\langle\psi_{10}\right| \\ &+(P_X^2+(1-P_X)^2)\frac{(1-(1-2p_z)^{N_E})}{2}\left|\psi_{01}\right\rangle\left\langle\psi_{01}\right| \\ &+2P_X(1-P_X)\frac{(1-(1-2p_z)^{N_E})}{2}\left|\psi_{11}\right\rangle\left\langle\psi_{11}\right|, \end{aligned} \tag{6.8}$$

and the final mixed state is given by the weighted sum of these,

$$\begin{aligned}\rho_f = \sum_{\{b_i\},\{a_i\}} &p_z^{N_Z}(1-p_z)^{N_E-N_Z}P(\{a_i\}\,|\,\{m_j\})\times \\ &\rho_c(\{b_i\},\{a_i\}).\end{aligned} \tag{6.9}$$

Since P_X is independent of the state separation it can be seen that as long as there are no phase errors present, that is, $p_z = 0$, the state produced has a fidelity that is independent of the node separation. These states that do not experience phase errors are called binary states [48]. My global error correction procedure is a generalization of the one given in [64] but does not involve explicitly teleporting qubits and can be easily applied to any network geometry. Later I show that we

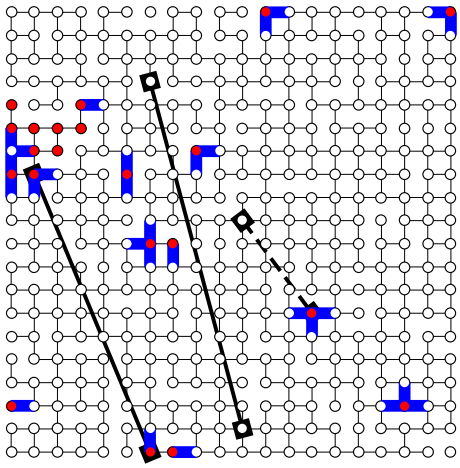

Figure 6.5: Here a 20x20 network has had its bonds removed with a probability of 0.05 and then X errors introduced with a probability of 0.05. I applied my global error correction procedure, and eventually this generates a GHZ state with patches of nodes that exhibit unwanted, extra bit-flips (filled red circles). If we try to link a node from within a patch to outside of them (dashed line) the final state two-qubit state exhibits a bit-flip error. Examples are also given of qubit pairings that would not exhibit errors (bold black lines).

can randomly purify states into binary states, obtaining them on random bonds but also destroying all of the entanglement in the remaining bonds. My scheme can still be applied in these situations, and in Fig. 6.5 it is applied to a contributing term in the largest cluster of a square network that was missing such bonds. I discuss this in more detail in Sec. 6.3. Furthermore, in regular networks with all bonds intact, I performed simulations to reveal the critical threshold of p_x below which long distance entanglement distribution is always possible. This was done for both square and triangular networks (see Figs. 6.1(b) and 6.1(c))). In both cases the final state's fidelity decreases suddenly after a critical p_x value (see Fig. 6.6). These transitions become more prominent for larger networks, and later I attach values to the thresholds.

If both bit-flip and phase errors are present, the initial edges will be rank four Werner states [80]. To apply the procedure in this case we can use error correction codes to subdue the phase-flip errors [158, 82, 17]. All of the qubits are then replaced

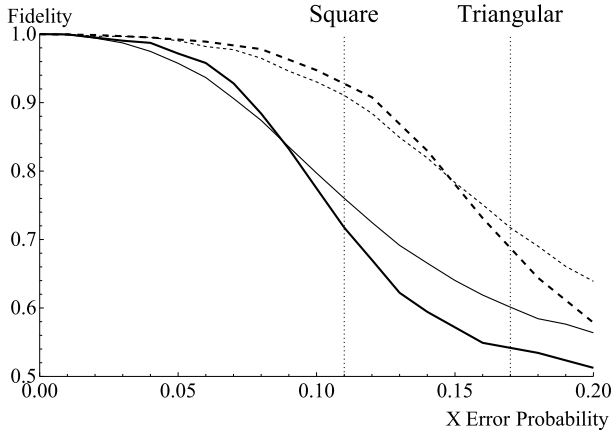

Figure 6.6: Fidelities are plotted from simulations of global error correction when run on complete square and triangular networks to produce a two-qubit entangled state between two randomly chosen qubits. In the square case (solid lines) a lower threshold is seen compared to the triangular network (dashed lines). Also included are the approximate threshold values (dotted vertical lines) calculated in Sec. 6.3. I used networks of 10x10 nodes and 20x20 nodes, with the larger networks presented by thicker lines; the threshold becomes more pronounced when the network gets larger.

with encoded qubits and all operations are replaced with their encoded versions. This technique was looked at in [64] for a square network using a majority voting Calderbank-Shor-Steane (CSS) code. In this case, for bonds containing $2t+1$ edges the phase error probability on each encoded edge can be suppressed to $\approx \binom{2t+1}{t+1} p_z^{t+1}$. To maintain a constant phase error probability on the final state the number of edges in each bond only needs to increase logarithmically with the size of the network. Unfortunately, this operation also increases the chance of a bit flip on the encoded edge to $\approx (2t+1)p_x$, which means that there is a point where the chance of a bit-flip exceeds the network's critical value, patches are no longer small and the procedure fails. When p_x is small this still enables the p_z error probability to be substantially reduced. For rank two, binary states, the number of edges required in each bond does not need to scale with distance, yet for rank four states there is a logarithmic scaling. In the following I am interested in extending the constant scaling with states that are of rank three.

6.3 Entanglement Distribution with Rank Three States

Using the global error correction procedure the edge errors in every pure state in an ensemble can be made to condense into patches on a large GHZ state in such a way that a highly entangled two-qubit state can be generated between two distant nodes. This requires the initial network nodes to be linked by sufficiently entangled binary states. However, in the following I show that such states can be probabilistically generated from a larger class of rank three states using LOCC. This widens the class of states in a 2D network that allow for long distance entanglement distribution.

It is impossible for a rank two, binary state to be created using anything other than states that are rank three or less. Binary states cannot be generated from two-qubit full rank states and I prove this by contradiction. If there were to exist some local procedure that produced some binary states from a full rank state then, by acting after with local projective measurements on all qubits except those in one binary state, we can easily construct a method to generate a single binary state and pure separable state. This local procedure can be described by an operator $M_A \otimes N_B$, where M_A and N_B act locally. The dimension of the entire Hilbert space is D. They must also satisfy $M_A M_A^\dagger$ and $N_B N_B^\dagger \leq 1$. The initial mixed state is

$$\sum_{i=1}^{D} p_i \left| i \right\rangle \left\langle i \right|,$$

with $p_i > 0, \sum_i p_i = 1$, and $\left| i \right\rangle \in H_A \otimes H_B$ is a complete basis. The procedure can then convert this initial state into

$$\sum_{i=1}^{D} p_i M_A \otimes N_B \left| i \right\rangle \left\langle i \right| M_A^\dagger \otimes N_B^\dagger = p\rho_{\text{bin}} \otimes \rho_{\text{sep}}.$$

ρ_{sep} is a pure separable state, ρ_{bin} is the two-qubit binary state and p a nonzero probability. Since the initial state was full rank this property requires $M_A \otimes N_B$ to be rank two. This is only the case when either M_A or N_B has rank one. Any operator, $M_A \otimes N_B$, with this property would not generate an entangled state. Hence, a binary state can not be generated using LOCC from a full rank state and this includes the case of finite full rank two-qubit states.

An example of a suitable state is demonstrated by the fact that if there are two rank three states of the form

$$\rho(\lambda, \nu) = \lambda \,|\, \psi_{00}\rangle \langle \psi_{00} \,| + \nu \,|\, \psi_{01}\rangle \langle \psi_{01} \,| + (1 - \lambda - \nu) \,|\, 01\rangle \langle 01 \,|\,, \tag{6.10}$$

with $0 \leq \lambda, \nu \leq 1$ and $\lambda + \nu \leq 1$, then they can be probabilistically distilled into a binary state

$$\rho_b(p'_x) = (1 - p'_x) \,|\, \psi_{00}\rangle \langle \psi_{00} \,| + (p'_x) \,|\, \psi_{10}\rangle \langle \psi_{10} \,|\,, \tag{6.11}$$

where

$$p'_x = 1 - \frac{(\lambda + \nu)^2 + (\lambda - \nu)^2}{2(\lambda + \nu)^2}. \tag{6.12}$$

The states given by Eq. (6.10) can actually form (up to local unitaries) when both qubits of a maximally entangled state, $|\, \psi_{10}\rangle$, pass through phase flip and amplitude damping channels. Having two of these states the transformation to a binary state is done by performing the same "pure state conversion measurement" (PCM) discussed in chapter 5 and in Ref. [65, 66], followed by local Hadamard operations. The PCM involves performing two C-NOT gates locally, with one entangled state's qubits acting as the target qubits. These target qubits are then measured in the computational basis. If both qubits are found to be in state $|\, 1\rangle$, it has succeeded, which happens with a probability of $(\lambda + \nu)^2/2$. If it fails, then the entanglement has been destroyed and both edges used. A graph of p'_x and the probability of suc-

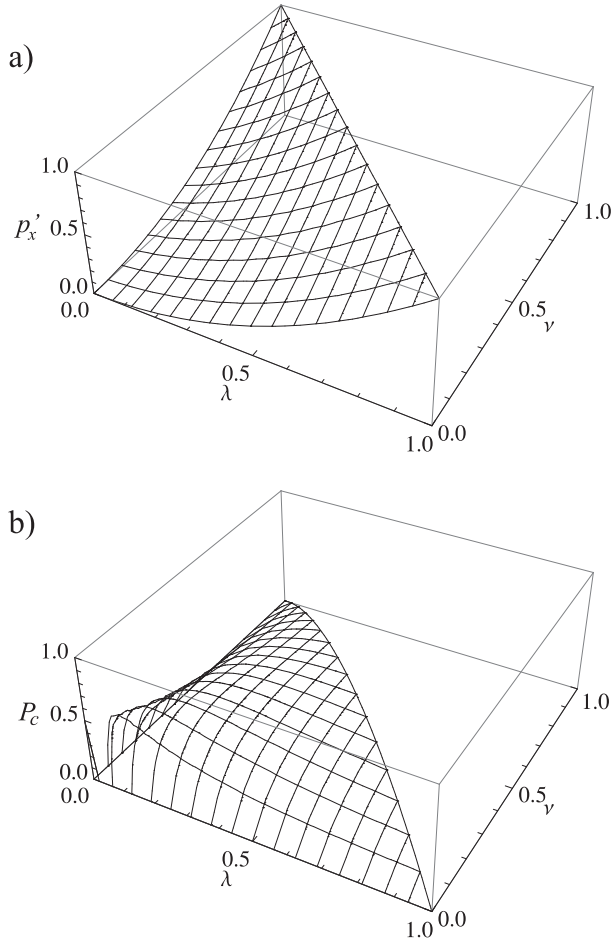

Figure 6.7: (a) p'_x coefficient for the binary state created using a PCM. (b) The probability, P_c, of generating a binary state from two initial states, *i. e.* $m = 2$, of the type given by Eq. 6.10.

ceeding is shown in Fig. 6.7. From this it can clearly be seen that to minimize the resulting p'_x, we would like $|\lambda - \nu|$ to be maximal. The maximal success probability with two states is 1/2. If there are m initial states in a bond we can generate a binary state with finite probability exceeding $P_c = 1 - [1 - ((\lambda + \nu)^2/2)]^{\lfloor m/2 \rfloor}$, which can be arbitrarily close to one given enough edges. Again, if this fails then all of the edges are lost. Note that any state that can be locally transformed into the states given by Eq. (6.10) can also be used to generate binary states and these are not the only rank three states that can be used to generate binary states.

By using this purification procedure it is possible to transform an initial network

composed of rank three states into a network of binary states, where the bonds are missing with a certain probability. This is the case for the network shown in Fig. 6.5. All of the nodes that are connected by a path of entangled states are then said to be in a cluster. For entanglement to be generated between two nodes they must both be in the same cluster and this links with results from bond percolation theory [100]. For a square network of infinite extent, if the success probability of transforming each bond into a binary state is larger than $1/2$ then a cluster that contains infinite nodes is almost certain to exist. This is the "percolation threshold" and values for further geometries are listed in Table. 5.1. The probability of a node being inside the infinite cluster is given by the "percolation probability", $\phi(P_c)$. The values of these together with $\psi(P_c)$, the probability that a bond exists and is linking nodes in the infinite cluster, can be calculated numerically for different networks [159, 160]. For large finite networks this threshold phenomenon still exists but the transition becomes smoother. In this case, when the critical value is exceeded a large cluster is obtained that contains a majority of the nodes. I will assume that P_c exceeds the percolation cluster as otherwise there is no infinite cluster. We can then apply my general global correction procedure to this cluster to obtain a highly entangled state between two nodes. This requires that the binary states present in the largest cluster are sufficiently entangled for global error correction to succeed. I use entropic arguments to give an approximate threshold for a finite square network, with sides consisting of L nodes. The cluster will contain an average of $\langle N_E \rangle = 2L(L-1)\psi(P_c)$ binary states, with each of these introducing a Shannon entropy $H(p'_x)$. The measurements then extract one bit of information from every plaquette in the cluster. Using Euler's formula [161] for finite, connected, planar graphs, the number of these plaquettes on average is given by $\langle N_P \rangle = 2 + \langle N_E \rangle - \langle N_N \rangle$, with $\langle N_N \rangle = L^2\phi(p_x)$ being the average number of nodes in the cluster. We require $\langle N_P \rangle > \langle N_E \rangle H(p'_x)$ for enough information to be gathered and this gives a bound for p'_x when $H(p'_x) = \langle N_P \rangle / \langle N_E \rangle$

is solved. These bounds define a region for P_c and p'_x within which long distance entanglement distribution can be achieved. In the infinite network case, $N \to \infty$, we have $\psi(P_c) = P_c\phi(P_c)$ and can calculate that

$$\begin{aligned} \langle N_P \rangle / \langle N_E \rangle &= 1 + \frac{2 - L^2\phi(P_c)}{2L(L-1)P_c\phi(P_c)} \\ &\overset{N\to\infty}{\to} 1 - (2P_c)^{-1}. \end{aligned} \tag{6.13}$$

Given that $P_c > 1/2$ so that an infinite cluster to exist, this defines a region by the relation

$$(1 - H(p'_x))P_c > 1/2, \tag{6.14}$$

and the boundary is shown in Fig. 6.8. My procedure is also related to methods developed to cope with qubit loss in surface codes [27] and similar critical regions have been found in these situations. For the case where $P_c = 1$ the critical value of p'_x in an infinite square network is then given by $H(p'_x) = 1/2$. This can be solved to yield a threshold of $p'_x = 0.11$. Further analysis for the complete square case is given in Ref. [64], and by relating the scheme to surface code error correction [88], a threshold of $p'_x = 0.1094$ is found. Similarly, in a complete, infinite triangular network, I calculated $H(p'_x) = \langle N_P \rangle / \langle N_E \rangle = 1 + (2 - L^2)/(L-1)(3L-1) \to 2/3$, yielding a threshold of $p'_x = 0.17$. Both of these thresholds are shown in Fig. 6.6. In this figure it can be seen that the higher connectivity present in the triangular network does provide for a higher fidelity and a lower threshold than does a square network. The simulations were run for finite networks so a perfect transition at the critical threshold does not occur. However, as the networks become larger the fidelity will approach 1/2 for these critical values. Note that these critical values are calculated for the ideal method and will be slightly larger than the simulated threshold due to the random choice of paths.

I have performed numerical simulations of the scheme, when edges are removed randomly, for a 25x25 square network. This involved using Monte Carlo methods to obtain random percolated network samples and error configurations. On each run the protocol was then performed. The main contribution to the calculations time is in the construction of a complete graph, that connects every pair by a weighted edge of the shortest path length. This was required by the implementation of Edmond's algorithm, that I used to obtain the minimum weight matching [157]. Together with finding the path linking the pairs, this step scales as $O(L^6)$. By combining the samples the final singlet state fidelity for different purification parameters was calculated and the results are shown in Fig. 6.8. This was run over a week and performed using Mathematica on a single workstation. My boundary between the values allowing long distance entanglement distribution and those that do not is also shown. This gives a good separation between the parameters producing singlets and those resulting in separable states. There is no sharp transition between the low and the high fidelity region which is due to the finite network size. The limiting cases of pure state percolation and binary state global error correction are given by $P_c > 0.5$, $p'_x = 0$ and $P_c = 1$, $p'_x < 0.11$, respectively.

6.4 Chapter Summary

Previous to this work, long distance entanglement distribution over an arbitrary distance, with finite local resources, could only be accomplished with rank two states, or less, in regular 2D networks [57, 64, 65, 66]. No other states can be used to create perfect singlets with finite resources. Here I have devised a global error correction scheme that enables a highly entangled state to be generated over an arbitrary distance. This procedure can be applied to any network composed of binary states and allows the creation of multiqubit GHZ states. By combining this method with

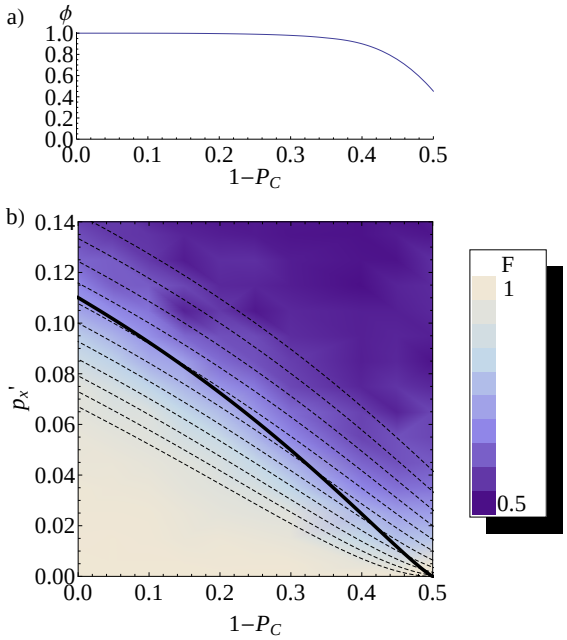

Figure 6.8: (a) The probability of a node existing in the largest cluster, ϕ. (b) Based on a 25x25 square network, the fidelity F between two randomly chosen nodes in the largest cluster of connected nodes is shown depending on the bond conversion probability P_c and X-error probability p'_x. The boundary for values, given by Eq. 6.14, that allow long distance entanglement distribution in infinite networks is shown as the thick solid (black) line. Pure states can be probabilistically transformed into binary states with parameters along the dashed lines (see next chapter). These lines are for the pure states $\alpha = 0.75, 0.76 \cdots 0.85$, from lowest to highest p'_x values, respectively.

entanglement percolation I have extended this ability to any network and a class of rank three states. These states would result from a combined amplitude damping and phase error channel. For networks composed of these rank three states it becomes possible to produce highly entangled states over arbitrary distances, with constant resources between the nodes. Although this is still a restricted case it is one step closer towards 2D networks composed of full rank states and allows us to deal with two important kinds of noise. Initially there must be a sufficient amount of entanglement between the nodes for the scheme to succeed and we have provided an entropic estimate for the requirements in percolated networks, based on the es-

timate in Ref. [64]. I have numerically calculated the resulting fidelities and the results agree with the threshold estimate. The procedure is still limited to rank three states but global error correction can be applied to full rank states with the help of an error correcting code. If this is done the local resources need to scale logarithmically with the distance between the final entangled nodes.

Chapter 7

Entanglement Enhancement

Here I develop further improvements on the success probability of my long distance entanglement distribution procedures by using particular forms of "quantum preprocessing" on specific networks. Similar techniques have been applied previously for percolation protocols involving pure states and I give a brief description of these techniques. They show that classical percolation is not the optimal procedure in regards to the resources required for long distance entanglement distribution. My generalized mixed state strategies include a form of entanglement swapping and I show how these strategies can be embedded in regular and hierarchical quantum networks. All of these preprocessing strategies involve compromising on aspects of the original schemes. I will discuss different advantages of entanglement percolation and global error correction under certain conditions and reveal a pre-processing trade-off between them when acting on networks containing pure states.[1]

7.1 Introduction

Classical entanglement percolation (CEP) and global error correction (GEC) are effective protocols, on specific mixed and pure states, for long distance entanglement generation. Yet, the advantages of each and the possibilities for further improvement are unclear. It was originally shown by Acín et al [57], when entanglement

[1]The material in this chapter has been published in the articles, Stuart Broadfoot, Uwe Dorner and Dieter Jaksch - Phys. Rev. A **81**, 042316 (2010) and Phys. Rev. A **82**, 042326 (2010).

percolation was introduced, that with pure states it is not optimal and lower initial requirements are sufficient for long distance entanglement distribution. I will briefly review a few of these pre-processing techniques and then in Sec. 7.2 I show that the idea of "quantum preprocessing", that was successfully applied to pure state networks, can be generalized to mixed states. In particular I devise a number of strategies on small networks which improve the SCP, and I show that these smaller networks can be embedded into larger networks to enable CEP which would otherwise not be possible. Furthermore, I apply my findings to "hierarchical network", i.e. networks which are defined iteratively (see chapter 2). In these networks it turns out that my quantum methods can also outperform classical percolation.

The choice of method used always involves a compromise based on the requirements of the system. In Sec. 7.3, to demonstrate this I look at the application of classical percolation and global error correction on a pure state square lattice network. These protocols can be combined to create a range of altered schemes that allow for a continuous transition from a pure state global error correction method to entanglement percolation. I find that global error correction allows any two chosen nodes in the network to be linked by an entangled state, but this is at the expense of the state's fidelity. Entanglement percolation only allows pairs of nodes from a known subset to be to be connected, but this is via a perfect singlet and allows more singlets to be created between other pairings from one application. If the criteria for entanglement percolation are not satisfied we have to use a specific combined scheme to create states of maximal fidelity and the choice of this scheme is dependent on the initial states in the network. This is a demonstration of the type of trade-off typical in choosing the method to use.

7.2 Quantum Preprocessing

Despite being a very effective method, it is known that CEP in a network of pure states can be improved by certain quantum "preprocessing" strategies. These strategies were first introduced in relation to classical percolation on regular networks [57, 58, 59, 62]. There the network geometry is transformed via the addition of swapping operations before the distillation of singlets. As discussed in chapter 2, a swapping operation, in the ZZ basis, followed by distillation has the same SCP as an individual distillation operation on one of the states. This means that the extra operation has transformed the problem of percolating singlets on the initial lattice to the new lattice. The percolation threshold of the new lattice can be satisfied by the new SCP even if the original lattices percolation threshold was lower that the initial bond's SCP. Another strategy uses swapping operations to split a square lattice into two separate square lattices. By performing classical entanglement percolation on these two lattices it is possible to create two long distance entangled states with a higher probability than could be achieved by applying CEP on the single lattice. Later Cuquet and Calsamiglia showed that a special q-swap operation could be used, as a preprocessing step, on complex networks to substantially improve the percolation threshold [60, 146]. Note that in all of these strategies aimed at reducing the percolation threshold we are removing nodes from the system or splitting them into two networks in the preprocessing step. This reduces the possible nodes that can be entangled via the procedure. In the following I show that preprocessing techniques can also be used in the case of mixed-state networks.

7.2.1 Swapping procedure

To adapt these schemes to mixed states I will start by generalizing the swapping arrangement shown in Fig. 2.2 previously studied for pure states [58, 46]. In this

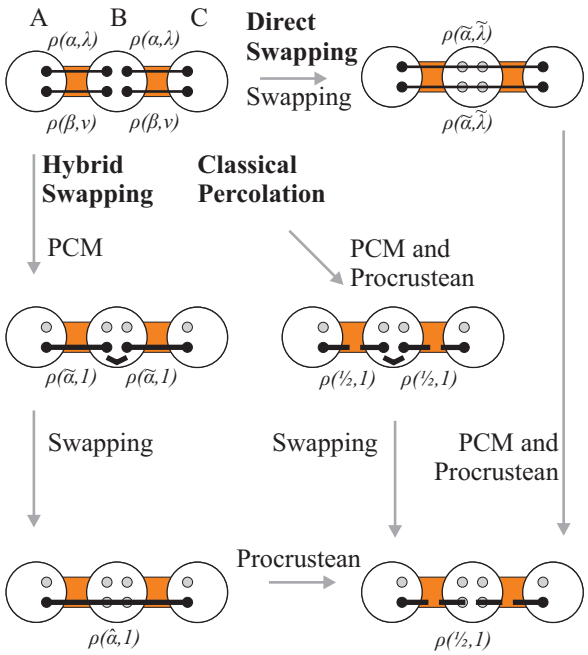

Figure 7.1: Three methods can be used to generate a singlet between two nodes A and C via an intermediate node B in an arrangement with two edges per bond. The thick black lines indicate pure but not maximally entangled states.

arrangement I have two two-qubit states that both have a qubit in a common node. If the two states are pure states $|\alpha\rangle$ and $|\beta\rangle$, with $\alpha \geq 1/2$ and $\beta \geq 1/2$, I can obtain a singlet by swapping and then converting the resulting pure state into a singlet with a total probability of $2\min((1-\alpha),(1-\beta))$ which turns out to be the optimal probability. Particularly CEP, which consists here of the Procrustean method followed by entanglement swapping, always has a smaller SCP of $4(1-\alpha)(1-\beta)$. Note that the optimality follows from the fact that the probability is equal to that of converting the least entangled of the two bonds into a singlet using the Procrustean scheme [46]. By splitting the system into two it can be seen that this probability is a bound to the success probability of any protocol.

To generalize this to mixed states we must consider double-edged bonds, each consisting of two PMSs, as illustrated in Fig. 7.1, since otherwise singlet generation would not be possible. Introducing more than one edge between the nodes allows me

to concentrate the entanglement at different stages which gives rise to three different possibilities:

I CEP. As previously described, the bonds are converted to singlets and then swapping is performed over the resulting states.

II Direct swapping. This applies entanglement swapping twice and then the resulting states are converted into a singlet.

III Hybrid swapping. Here I distill a state of higher entanglement in each bond (but not necessarily a singlet) leading, if successful, to a single (partially) entangled pure state in each bond. This is followed by entanglement swapping and the Procrustean scheme to create a singlet.

Each of these possibilities uses the swapping operation at different stages as illustrated in Fig. 7.1. The exact implementations for the procedures depend on the types of states used. I will first apply each of them on a network of pure states and compare the SCPs. I then generalize to PMSs and show that direct and hybrid swapping can outperform CEP.

Pure states

If I start with bonds made of pure states $|\alpha\rangle$ and $|\beta\rangle$ I must have a way to convert each bond into a singlet in order to apply CEP(I). The method and highest possible probability to accomplish this are given by majorization [91] with a probability $p = \min(1, 2(1-\alpha\beta))$ [58, 59]. CEP applies this operation on each bond and if both bonds are converted into singlets swapping can be performed and the operation is a success. Therefore CEP succeeds with a probability $(\min(1, 2(1-\alpha\beta)))^2$.

The second method, direct swapping (II), is simply the application of the procedure for bonds containing one edge twice. If either generates a singlet the procedure

succeeds. This gives a SCP of $1-(1-2(1-\alpha))(1-2(1-\beta))$. There are adjustments I could make; for example, use the results of majorization to convert both of the states into a singlet with the highest possible probability, however all of these have a smaller SCP than CEP for a range of parameters.

Finally, the hybrid swapping (III) method concentrates each bond to one pure state, $|\max(1/2, \alpha\beta)\rangle$, with certainty. This concentration procedure is also found using results from majorization theory [91]. Afterwards there is one pure state in each bond, as discussed previously, and I can then perform the strategy with optimal success probability $\min(1, 2(1-\alpha\beta))$, i.e. swapping over the pure states followed by the Procrustean method. I can actually consider the setup as a bipartite system between A and BC. The majorization results then give the best possible probability of generating a maximally entangled two-qubit state between these systems as $\min(1, 2(1-\alpha\beta))$ which means that it must be the highest possible probability for any method to succeed.

Figure 7.2 shows the probabilities in all three cases and we can see that CEP is outperformed for a vast range of parameters by both other strategies. In hybrid swapping (III), I have used multi-edged bonds to create pure states with the highest probability before applying entanglement swapping. I will refer to all strategies that have this property as "hybrid". This probability is unity for initial pure states but for mixed states the initial conversion of bonds to pure states is probabilistic, so when the conversion fails the bond is destroyed.

Purifiable Mixed States

I will now investigate if similar improvements can be obtained with PMSs, i.e. if the bonds between the nodes are composed of $\rho(\alpha, \lambda)$ and $\rho(\beta, \nu)$. Again I will see that hybrid swapping provides the highest SCP. The results for general PMSs, $\rho(\alpha, \gamma, \lambda)$ and $\rho(\beta, \delta, \nu)$, are included in Appendix B.

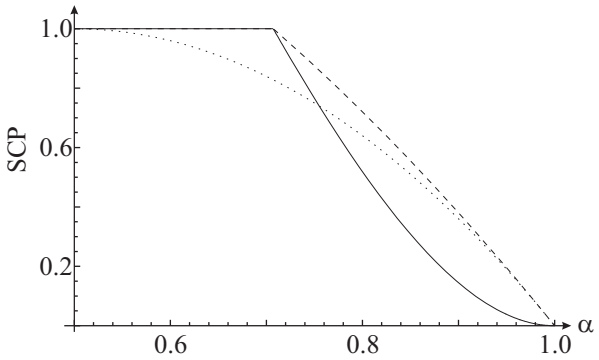

Figure 7.2: Comparison of the three methods described in the text for creating a singlet between nodes A and C in the setup shown in Fig. 7.1 for pure states. Shown are the success probabilities if the bonds are each made up initially of two states $|\,\alpha\rangle$ for CEP (solid line), direct swapping (dotted line) and hybrid swapping (dashed line).

I CEP

The classical percolation scheme involves performing a PCM, described in chapter 4, followed by the Procrustean protocol on both bonds and each succeeds with a probability given by Eq. (4.5) which simplifies to

$$p_{conv} = 2\lambda\nu \min(\alpha(1-\beta), \beta(1-\alpha)). \tag{7.1}$$

To perform a swapping operation yielding a singlet, between nodes A and C we must succeed for both bonds which gives the total chance of success

$$p_{CEP} = (2\lambda\nu \min(\alpha(1-\beta), \beta(1-\alpha)))^2, \tag{7.2}$$

by simply squaring Eq. (7.1). In this case the swapping operation is the final step of the protocol.

II Direct swapping

In our 2-edged setup I perform the swapping operation, mentioned in chapter 4,

twice and there are two choices to do this if the states are not identical. Either I perform the swapping over the identical states $\rho(\alpha,\lambda)\otimes\rho(\alpha,\lambda)$ or I perform the operation on the states $\rho(\alpha,\lambda)\otimes\rho(\beta,\nu)$. When I swap over identical states I obtain the state

$$\rho\left(\frac{\alpha^2}{1-2\alpha+2\alpha^2},\lambda^2(1-2\alpha+2\alpha^2)\right), \tag{7.3}$$

together with a further state where β is replacing α and ν is replacing λ. Note that Eq. (7.3) is obtained by setting $\gamma=\delta=0$ and $\alpha=\beta$, $\lambda=\nu$ in Eq. (4.11). This pair of states can then be transformed into a singlet with a probability

$$p_{d^*}=2\lambda^2\nu^2\min(\alpha^2(1-\beta)^2,\beta^2(1-\alpha)^2) \tag{7.4}$$

which is calculated using Eq. (7.1). In the case where I swap over nonidentical states $\rho(\alpha,\lambda)\otimes\rho(\beta,\nu)$ I obtain two states of the form (4.11) with $\gamma=\delta=0$. These can be converted into a singlet with probability

$$p_d=2\lambda^2\nu^2\alpha\beta(1-\alpha)(1-\beta). \tag{7.5}$$

This is always larger than p_{d^*} and thus swapping with nonidentical states should be preferred.

III Hybrid swapping

The hybrid method requires a concentration procedure to be performed (yielding a single pure state in each bond) which is given here by PCM. However, in contrast to the pure state case discussed above, if $\alpha=\beta$ I obtain singlets (in which case the method is identical to CEP) and, generally, the operation succeeds with a finite probability given by Eq. (4.4). For nonidentical PMSs

PCM yields two nonmaximally entangled pure states which are then used for entanglement swapping followed by the Procrustean method. The probability of succeeding in converting both of the bonds to pure states is

$$p_c^2 = \lambda^2\nu^2(\alpha(1-\beta)+\beta(1-\alpha))^2. \tag{7.6}$$

These pure states have largest Schmidt coefficient

$$\hat{\alpha} = \frac{\max(\alpha(1-\beta),\beta(1-\alpha))}{(\alpha(1-\beta)+\beta(1-\alpha))}. \tag{7.7}$$

So, by using the SCP in single-edged swapping with pure states I find that I can convert this pair of states into a singlet between the end nodes with probability,

$$2(1-\hat{\alpha}) = 2\frac{\min(\alpha(1-\beta),\beta(1-\alpha))}{(\alpha(1-\beta)+\beta(1-\alpha))}. \tag{7.8}$$

Hence, the overall probability of succeeding with this scheme is

$$\begin{aligned} p_h =& 2\lambda^2\nu^2[\alpha(1-\beta)+\beta(1-\alpha)] \\ & \times \min[\alpha(1-\beta),\beta(1-\alpha)]. \end{aligned} \tag{7.9}$$

If we compare the success probability of direct swapping, p_d, to the probability of success in the classical percolation scheme, p_{CEP}, it can be seen that classical percolation is more likely to succeed in producing a singlet if

$$2\min(\alpha(1-\beta),\beta(1-\alpha)) > \max(\alpha(1-\beta),\beta(1-\alpha)). \tag{7.10}$$

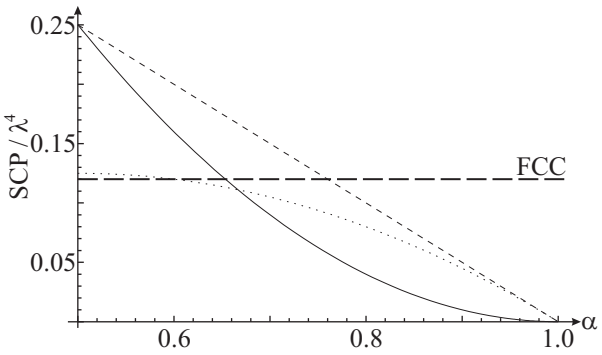

Figure 7.3: Success probability to generate a singlet between the end nodes of the swapping setup shown in Fig. 7.1 for the classical scheme (solid line), direct swapping (dotted line), and the hybrid scheme (dashed line). Each bond initially contains the states $\rho(\alpha, \lambda)$ and $\rho(1/2, \lambda)$. I have indicated the percolation threshold of a face-centred cubic network.

But the ratio of the success probability for the classical scheme against the hybrid protocol, p_h, is

$$\frac{p_{CEP}}{p_h} = \frac{2\min(\alpha(1-\beta), \beta(1-\alpha))}{(\alpha(1-\beta) + \beta(1-\alpha))}. \tag{7.11}$$

Whenever $\alpha \neq \beta$ this is less than one and there is an improvement over the classical percolation scheme. Furthermore, the hybrid scheme is more likely to succeed than direct swapping. In Fig. 7.3 I compare the probabilities of success for all schemes. As can be seen, hybrid swapping leads to the highest success probability.

Hybrid swapping can be used in sections of larger networks to allow percolation to take place. A simple example is a face-centred cubic (FCC) network, where every bond is split into two 2-edged bonds (see Fig. 7.4). When the above schemes are applied at the nodes linking two 2-edged bonds the FCC network is recovered. Percolation is possible in these 3D networks with a threshold of approximately 0.12. Since the classical scheme always gives a smaller success probability than the hybrid scheme there are cases where the hybrid scheme allows the percolation threshold to be exceeded but the classical scheme does not (see Fig. 7.3).

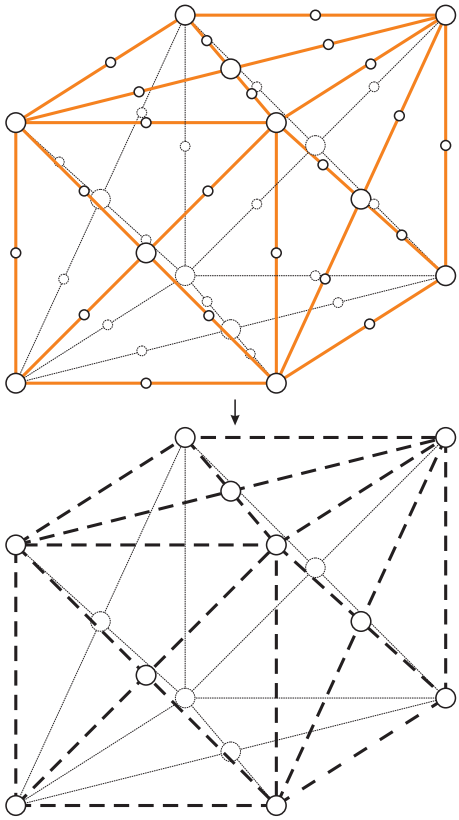

Figure 7.4: Illustration of entanglement percolation in a 3D network. The circles represent nodes containing qubits and the lines represent bonds containing pairs of two-qubit entangled states (the edges are not shown). The 3D network can be transformed into a face-centred cubic network by performing the swapping operations (see Fig. 7.12) over the smaller nodes. For some bond parameters the hybrid scheme allows percolation to occur where classical percolation fails.

7.2.2 The Square Protocol and Hierarchical Networks

CEP can also be improved on by using the hybrid strategy in a 2D square network, as shown in Fig. 7.5. Each bond is converted into a pure state, $|\hat{\alpha}\rangle \equiv \sqrt{\hat{\alpha}}\,|00\rangle + \sqrt{1-\hat{\alpha}}\,|11\rangle$, by using PCM which is successful with a probability p_c on each bond. If this yields only two states $|\hat{\alpha}\rangle$ having a common node (B or C), entanglement swapping can be performed followed by the Procrustean scheme. If all four PCMs succeed the resulting states can be connected (e.g. at nodes B and C) via a slightly modified version of entanglement swapping, the so-called XZ swapping [58]. For this swapping operation the Bell measurement that usually has both qubits measured

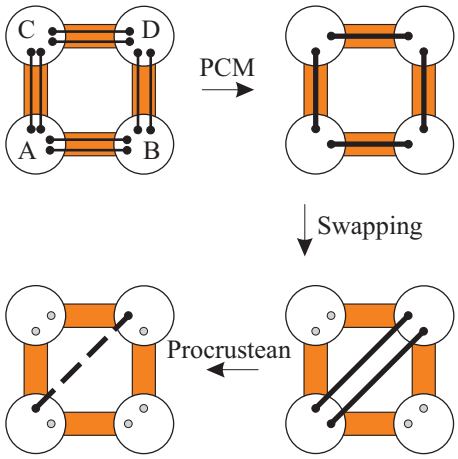

Figure 7.5: Application of the hybrid scheme in a square network. This involves transforming the PMSs into pure states probabilistically and then applying a suitable pure state procedure (see text). In the case shown all of the conversions are successful. When this happens a swapping operation can be performed and the resulting states distilled into a singlet.

in the Z basis now measures one in the X basis. After this measurement unitaries are again applied to return the state into Schmidt form. The results of the Bell measurement have an equal probability, $p_m = 1/4$, for all outcomes m. Performing this operation twice on the square leads to two pure states (between A and D) of the form $|\,\tilde{\alpha}\rangle$, with $\tilde{\alpha} = (1+\sqrt{1-16\hat{\alpha}^2(1-\hat{\alpha})^2})/2$. These can be distilled into a singlet with probability $\min[1, 2(1-\tilde{\alpha}^2)]$ by using the protocol based on majorization [91]. The overall chance of succeeding in generating a singlet is then given by

$$p_{sq} = 4p_c^2(1-p_c^2)(1-\hat{\alpha}) + p_c^4 \min(1, 2(1-\tilde{\alpha}^2)). \tag{7.12}$$

When attempting to accomplish the same scheme using CEP I succeed with a probability of $\tilde{p}_{CEP} = 1-(1-p_{CEP})^2$ which can be significantly smaller than Eq. (7.12), as shown in Fig. 7.6.

Again, this improved strategy may enable an infinite cluster to form when applied to larger networks. An example is shown in Fig. 7.7. Here the square protocol recovers a triangular lattice. If the conversion of the squares into singlets succeeds

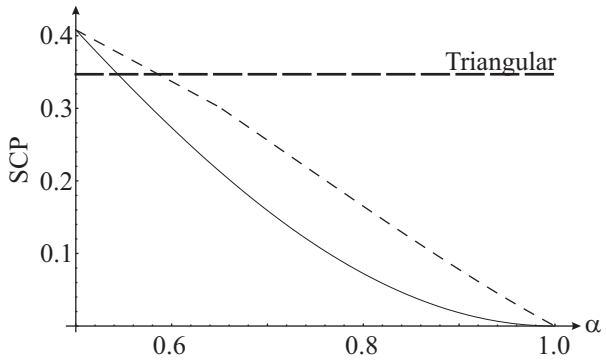

Figure 7.6: Comparison of singlet conversion probabilities for the different strategies in the square configuration, that is, $\tilde{p}_{CEP}$ (solid line) and p_{sq} (dashed line) for $\lambda = \nu = 0.98$, $\beta = 0.5$. I have also indicated the percolation threshold for a triangular network.

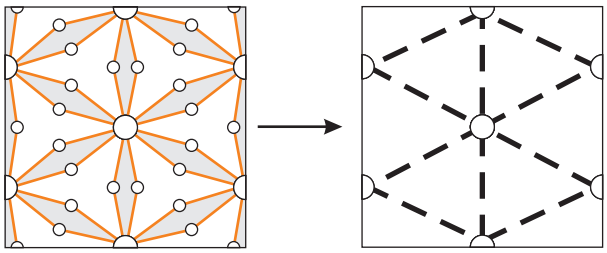

Figure 7.7: By applying the square protocol on the shaded regions a triangular network of randomly distributed singlets (dashed lines in the right figure) is recovered. In the left figure the nodes (circles) are linked by bonds (solid lines) each containing two edges (not shown).

with a probability exceeding the percolation threshold an infinite cluster forms. In Fig. 7.6 it can be seen that the hybrid scheme exceeds the threshold for a triangular lattice in cases where CEP does not.

Small networks like the square configuration discussed above can be extended to larger networks in an iterative fashion. Networks formed in this way from pure states were considered in [58]. Again the probability of successfully creating a singlet was shown to be larger when quantum strategies were used instead of CEP. However, the scheme with the highest probability is still unknown for these "hierarchical" networks. Here I will consider two different hierarchical networks with two edges

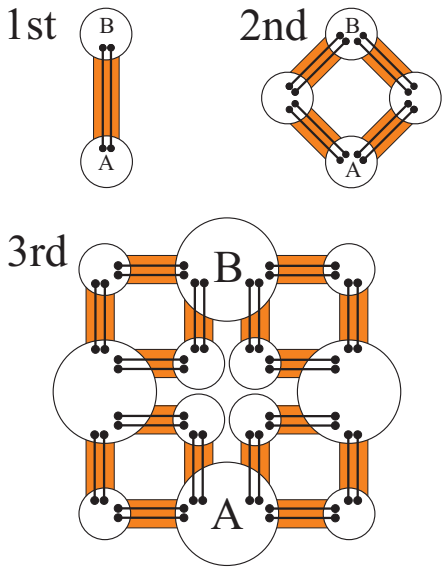

Figure 7.8: The first three iterations of a diamond lattice. I aim to create a singlet between nodes A and B in each case.

per bond. Each of these contains the square network at some iteration level. I determine the SCP when using CEP in both cases which I then compare to the hybrid strategy. As it turns out, the hybrid scheme outperforms CEP.

The first hierarchical network I consider is based on the "diamond" lattice, which at each stage replaces its bonds by the square network. The geometry for the first three iterations is shown in Fig. 7.8. The aim is to create a singlet between A and B and if I apply CEP the probability of succeeding at each level is given by the iterative formula

$$p_i^{\text{Diamond}} = 1 - (1 - p_{i-1}^2)^2, \tag{7.13}$$

starting with $p_1^{\text{Diamond}} = p_{\text{conv}}$.

The second hierarchical network I consider is the "tree" network which is again built on the square configuration. For these networks an iteration is formed by creating two copies of the previous iteration and linking the bottom-left and top-right corner of the square to separate nodes A and B as shown in Fig. 7.9. Again, the aim is to generate a singlet between the opposite corner nodes (A and B) and

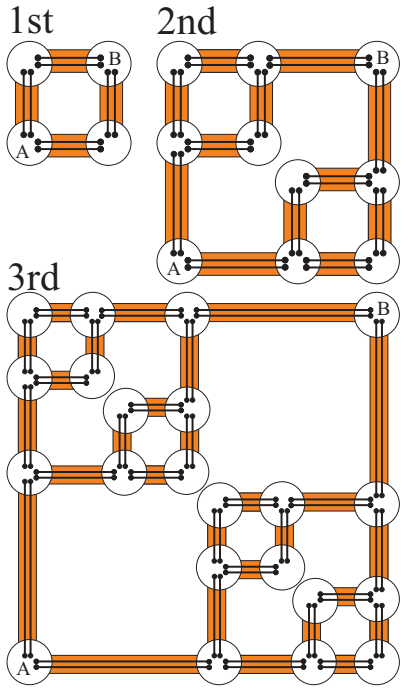

Figure 7.9: First three iterations of the tree lattice. Each iteration is given by repeating the previous lattice twice and linking the pair of previous endpoints at new endpoints. The aim is to create a singlet between nodes A and B.

CEP generates a singlet with a probability

$$p_i^{\text{Tree}} = 1 - (1 - p_{i-1} p_{\text{conv}}^2)^2, \tag{7.14}$$

where $p_0 = 1$.

Now I wish to see whether the hybrid scheme gives a larger SCP in these networks. Once again, the hybrid scheme I consider starts by converting all of the bonds into identical nonmaximally entangled pure states probabilistically. If the conversion fails on a bond then the bond is destroyed. This results in a network containing random pure state bonds. Each of these bonds contains one edge. Ideally we would then apply a pure state protocol yielding the highest SCP between the intended nodes, however, this protocol is not known in the general case [58]. Instead I apply a procedure which performs XZ swapping in cases when two bonds

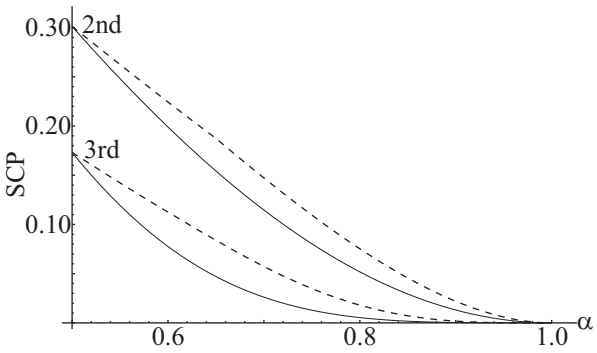

Figure 7.10: Probability of succeeding in generating a singlet between the endpoints of a diamond lattice for the 2nd and 3rd iterations (dashed lines). These give higher probabilities than the classical protocol (solid lines). The bonds contain two edges with parameters $\lambda = \nu = 0.9$, $\beta = 0.5$.

each have a qubit in the same node (except if these nodes are A or B). However, I also distill pure states into states with more entanglement whenever two edges form between two nodes and before performing further swapping. Finally, once one state is obtained between A and B, the Procrustean procedure is used to create a singlet.

I applied this protocol to the hierarchical diamond and tree networks. For the second and third iterations of the diamond lattice the probabilities of creating a singlet are given in Fig. 7.10 together with the probabilities using CEP. This comparison was also made for the first, second and third iteration of the tree network and the results are shown in Fig. 7.11. These examples all illustrate an improvement in the probability of forming a singlet when using the hybrid method rather than classical percolation.

7.3 Comparisons between different strategies on Pure state networks

It is interesting to look at the behaviour of entanglement percolation and global error correction when creating long distance entanglement from the same initial network.

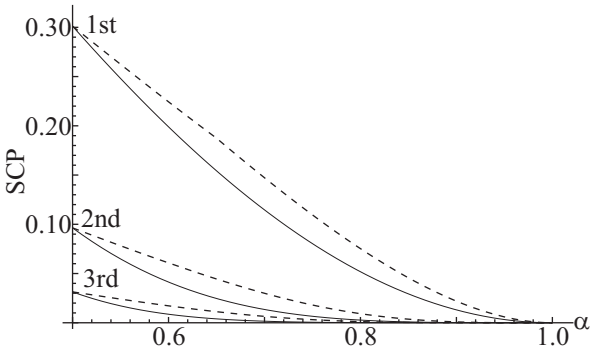

Figure 7.11: Probability of succeeding in generating a singlet between the endpoints of the 1st, 2nd, and 3rd iterations of the tree lattice (dashed lines). These also outperform the classical protocol (solid lines). The bonds contain two edges with parameters $\lambda = \nu = 0.9$, $\beta = 0.5$.

These procedures require a network of identical initial states. If the bonds in the network contain enough entanglement they produce a highly entangled state between two nodes that are a long distance apart. The two nodes that are connected are out of a random set of nodes. Different methods may have benefits such as requiring less entanglement in the initial bonds, generating higher entangled states between two nodes or allowing a greater proportion of nodes to be linked by the entangled state. Pure states are the simplest case where this comparison can be considered so I will look at this case.

By randomly generating binary states between nodes from the initial states and then using global error correction I have found a method that works on networks containing rank three states. This can be adjusted to start with pure states, which can be randomly transformed in pure states with more entanglement, via majorization based filtering. A choice emerges here as to which pure state to distill. Binary states can be generated from each of the percolated pure states ready for global error correction to be performed. By choosing different pure states to be generated, I will later find that each of these may provide further benefits compared to entanglement percolation or global error correction.

For pure nonmaximally entangled states, entanglement percolation is known to succeed in creating a long distance singlet state deterministically [57]. This requires a geometry dependent amount of entanglement, related to the percolation thresholds (see Table. 5.1). Let us recall that any pure state can be transformed via local unitary operations into its *Schmidt decomposition*,

$$|\,\alpha\rangle = \sqrt{\alpha}\,|\,00\rangle + \sqrt{1-\alpha}\,|\,11\rangle\,, \tag{7.15}$$

with α being the largest Schmidt coefficient, $1 \geq \alpha \geq 1/2$.

Apart from basic entanglement percolation other techniques have also been proposed in pure state networks with smaller initial entanglement requirements [57, 58, 59, 61]. These include the global error correction in a square network with no missing edges, as discussed in [64], and it was shown that a lower amount of entanglement was required to succeed at the expense of the final state's fidelity. By randomly generating different states before global error correction, it becomes possible to explore the transition between global error correction and entanglement percolation. Here I again choose to create binary states by probabilistically converting pure states into binary states. When I start with pure states there are a number of ways to perform this operation. These create binary states with a higher probability of success or more entanglement. To perform the conversion each pure state is transformed, using LOCC, into another pure state

$$|\,\alpha'\rangle = \sqrt{\alpha'}\,|\,00\rangle + \sqrt{1-\alpha'}\,|\,11\rangle\,, \tag{7.16}$$

that has higher entanglement, with the optimal probability of succeeding $P_c = (1-\alpha)/(1-\alpha')$. This operation involves a local measurement at one qubit. The result is then communicated to the other qubit, where a unitary is performed. This

transformation operation and probability come from majorization results [91]. These states can then be "twirled" [42, 79] into binary states, with $p'_x = (\sqrt{\alpha'}-\sqrt{1-\alpha'})^2/2$. These actions probabilistically generate binary states at random bonds, allowing global error correction to be applied. The value of P_c can be adjusted between 0 and 1. If P_c is larger than the percolation threshold then an infinite cluster, of binary states $\rho_b\,(p'_x)$, is formed and a node is a member of this cluster with probability $\phi(P_c)$. Any two nodes in the cluster can then be linked by global error correction. Two nodes are in the cluster with a probability of $\phi(P_c)^2$ and they can be turned into a binary state that has fidelity F after global error correction. In Fig. 6.8 the paths of $(1-P_c,\, p'_x)$ are shown for different values of α as a dashed line. Each point on these lines corresponds to a binary state that can be obtained from the initial pure state. The relationship between the available fidelities, F, and the fraction of nodes in the cluster is shown in Fig. 7.12. This fraction is given by $\phi(P_c)$, which can easily be calculated numerically to a high degree of accuracy. In comparison, the fidelity is dependent on simulating global error correction, which introduces considerable noise. This has the most influence when considering twirling straight away and using the global error correction. In Fig. 7.12 this is demonstrated by the numerical noise as $\phi \to 1$. Each line relates to a different initial pure state. For each dashed line representing an initial state in Fig. 6.8 the only points allowing long distance entanglement in the infinite case lie below the critical boundary, shown in Fig. 6.8.

If the requirement is to generate long distance entangled states with the highest possible amount of entanglement then, given that the threshold for entanglement percolation is satisfied, the preferred method is to randomly obtain perfect singlets and then use entanglement swapping. This generates a perfect singlet, however in doing so we reduce the number of nodes that are available to be linked. When the threshold is not satisfied we must probabilistically transform the initial states to binary states with the largest $1-P_C$ that still lie within the critical region. Doing

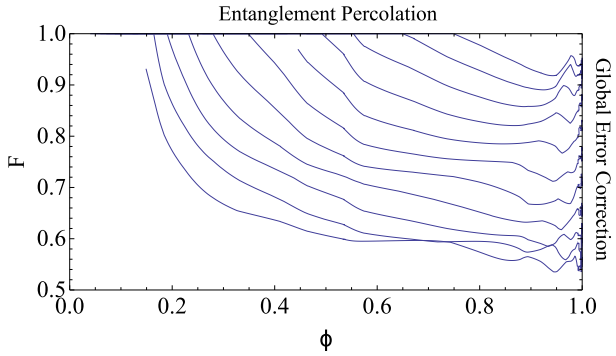

Figure 7.12: Starting from pure states, a range of binary states (dashed lines in Fig. 6.8) can be created. For each of these the largest cluster contains a different proportion ϕ of total nodes and any two of these can be linked using global error correction to leave a two qubit entangled state that has fidelity F. The different values of F and ϕ are given for each initial pure state. Shown are plots corresponding to eleven initial pure states with $\alpha = 0.75, 0.76, 0.77, \ldots, 0.85$ (top to bottom).

this creates one highly entangled state over a long distance. Note that the initial state of the edges needs to be known to decide on the state to percolate. The nodes to link can not be chosen before running the protocol, but we still know which nodes are linked at the end. If we are required to link two particular nodes, which have been chosen before the protocol is run, we must maximize ϕ, and this is achieved by using global error correction. The choice between maximizing the fidelity and maximizing ϕ is dependent on the intended use of the entangled state. If one entangled state between any two nodes in a set is sufficient, it may be beneficial to maximize ϕ. To judge the schemes, a figure of merit can be constructed from ϕ and the fidelity. This can then be maximized to reveal the preferred scheme. For example a suitable figure of merit in the case where two specific nodes need to be entangled would be $F\phi^2$, and this is maximized for global error correction.

7.4 Chapter Summary

During this chapter I have introduced additional steps that can be used to enhance entanglement percolation. This concept had been introduced previously for pure

states and I have extended the concept to my mixed state percolation scheme. This demonstrates that entanglement percolation is not optimal. Like in the pure state case, a higher probability of distributing a singlet can be obtained, when the states in a bond are not identical. The question of whether quantum strategies can outperform CEP when each edge in a bond is identical is still open. For pure states another quantum entanglement distribution protocol called "multipartite percolation" has also been suggested [61]. These act by percolating multipartite GHZ states using an adjusted swapping operation that acts on three qubits. This results in a site percolation problem. Extensions of multipartite methods, so that they act on mixed-state networks, still need to be devised although global error correction can be seen as a type of multipartite protocol.

It should be noted that different schemes have specific benefits and preprocessing steps usually act to trade-off one advantage for another. To give an example of this I have generalized global error correction to pure states. This allows for a range of pure-state schemes, each of which has applications in particular circumstances: For instance, I can identify a protocol for creating perfect entanglement between two distant nodes. However, this protocol can not generate a singlet between any two nodes. On the other hand, I can also construct schemes for creating entanglement between any nodes, but the corresponding entanglement fidelity is lower.

Chapter 8

The Excitation of Nanotubes by Nanofibre Photons

Here I introduce a novel proposal for a new means to couple photons with electronic excitations. This is of fundamental importance for entanglement distribution. My proposal involves the excitation of electrons in semiconducting carbon nanotubes by photons from the evanescent field created by a subwavelength-diameter optical fibre. The strongly changing evanescent field of such nanofibres requires dropping the dipole approximation. I show that this leads to novel effects, especially a high dependence of the photon absorption on the relative orientation and geometry of the nanotube-nanofibre setup in the optical and near infrared domain. In particular, I calculate photon absorption probabilities for a straight nanotube and nanofibre depending on their relative angle. In addition, I show that if the nanotube is wrapped around the fibre in an appropriate way the absorption is enhanced. I find that optical and near infrared photons could be converted to excitations with efficiencies that may exceed 90%. This may provide opportunities for future photodetectors and I discuss possible setups.[1]

[1]The material in this chapter is related to a patent application (UK Patent no. GB1119337.2) and has been published in the article, Stuart Broadfoot, Uwe Dorner and Dieter Jaksch - Phys. Rev. B **85**, 195455 (2012).

8.1 Introduction

It is clear that photons are the ideal qubits for use in entanglement distribution protocols due to their resistance against decoherence. Yet, they are not the ideal system for quantum information processing. It is of fundamental importance to find an efficient means to convert flying photonic qubits into qubits that can be processed. During this chapter I introduce a new system for this conversion. As a first step in its analysis I have focused on its photonic absorption, rather than quantum coherence, and emphasized its use for photon detection. Its successful application as a photo-detector would still be of great importance in current repeater schemes. The system I introduce is composed of a subwavelength-diameter optical fibre coupled to carbon nanotubes. A photon in a typical optical fibre can be coupled into a subwavelength diameter fibre (nanofibre). This makes such systems ideal for interfacing with current fibre optic telecommunications and optical fibre based quantum networks.

The unique physical properties of carbon nanotubes and the flexibility they provide in selecting their characteristics has already shown great potential for nanotechnology [162, 163, 164]. Carbon nanotubes can be either semi-conducting or metallic, depending on their diameter and helical configuration. They typically have nanometer sized diameters and a length of a few microns, although centimetre long nanotubes have been produced recently [165]. This makes them ideal 1D systems that possess a ballistic conducting channel [166], no backward scattering, and energy levels that can be adjusted with external fields [167, 168, 169]. Superconductivity has also been observed in multiwalled carbon nanotubes and single carbon nanotubes have exhibited a superconducting proximity effect [170, 171, 172, 173]. Their applications range from extremely strong fibres and organic electronics [174] to electrochemical sensors [175, 176] and photon detectors [177].

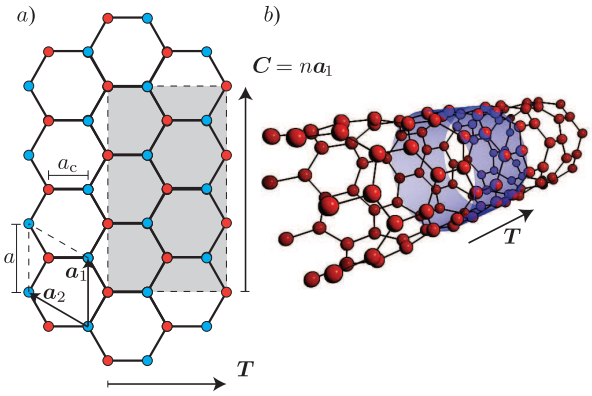

Figure 8.1: (a) Graphene lattice with the unit cells vectors labeled $\mathbf{a}_1$ and $\mathbf{a}_2$. These vectors have the length a. Here the atoms in the A sublattice are red and the B sublattice is cyan. a_c is the distance between neighbouring atoms. The unwrapped unit cell for a zigzag (3,0) nanotube is shown shaded and the $\mathbf{C}$ vector defines the nanotubes circumference. (b) A section from a zigzag (7,0) nanotube is shown with its unit cell shaded. $\mathbf{T}$ is the tangential unit vector of the nanotube's unit cell.

Carbon nanotubes are a form of carbon formed by rolling up a sheet of graphene into a cylindrical tube. An illustration of this is given in Fig. 8.1. Here I focus on the optical properties of carbon nanotubes. For a straight nanotube, inside a weak uniform classical plane wave field, these properties have been extensively studied [178, 179, 180, 181, 182, 183, 184, 185, 186, 187, 188]. Their quasi one-dimensionality means that their density of states exhibits Van Hove singularities and these contribute to strong optical absorption peaks. However, these results apply the dipole approximation, where it is assumed that the field does not vary along the nanotube's length. I extend this treatment by allowing for the spatial dependence of the field. This situation is particularly relevant when the electrons are delocalized in a tightly-confined field, such that the field varies greatly over a few hundred nanometres. The degree to which the electrons are delocalized is a topic of ongoing research and various studies have been done on the coherence length in nanotubes. Their results range from 10 nm to several microns suggesting that the spatial field dependence is certainly important for confined fields and may also be relevant for plane waves [189, 190, 191, 192, 193].

The other component of my system is a nanofibre. These are simply optical fibres that have a diameter smaller than the wavelength of the light. Once the photon is in the nanofibre, the electrical field is tightly confined and primarily exists outside of the fibre, in a large evanescent field [194]. Due to the presence of a strong field in a relativity small volume, these nanofibres are ideal candidates to achieve a high optical absorption in atomic systems. For example, their interaction with atom-arrays has been studied [195, 196, 197]. However, in contrast to such atom-fibre systems, the dipole approximation cannot be applied in the case of nanotubes since the optical field typically changes rapidly along a nanotube's length. I calculated the (internal) quantum efficiency, i.e., the probability that a nanotube, placed inside the evanescent field of a nanofibre, absorbs a photon. Calculations for the external quantum efficiency, i.e., the efficiency for detecting the excitation with the photocurrent, are not considered. However, it should be noted that important effects that could aid in this procedure, such as the avalanche effect, have been observed in carbon nanotubes [198]. I focus specifically on the example of zigzag nanotubes (see Fig. 8.1) because they can be direct semiconductors. However, my results are still representative of other semiconducting nanotube types such as chiral nanotubes. I found that the absorption is extremely dependent on the nanotube's orientation. These results are highly relevant for the interface between any future nanoscale photonics and carbon nanotubes.

I will be using the band-to-band tight binding transition model for the carbon nanotube. This has proven itself to be very effective in determining the basic optical properties of nanotubes but does not include effects due to excitons [199] and electron-electron interactions [200]. Such effects give measurable corrections and there have been a few studies considering the exciton absorption strength [178, 201, 184, 202]. Nevertheless, the band-to-band model is suitable to determine the main contributions to optical absorption.

I will begin by giving an overview of nanotube properties and the calculation of their band structure in Sec. 8.2. Based on this I then evaluate the photon absorption by zigzag carbon nanotubes in Sec. 8.3. For the setups considered the nanotubes experience fields that change strongly along their length, i.e. to calculate photon absorption we cannot rely on the dipole approximation. I obtain general expressions for the absorption probability which are then applied to cylindrical vacuum-clad silica nanofibres in Sec. 8.4, and discuss different geometrical setups of nanofibres and nanotubes. Possible photodetectors that use these setups are then presented in Sec. 8.5.

8.2 The Tight-binding Carbon Nanotube Model

Here I will review the basic properties of carbon nanotubes and layout the notation that I use in later sections. A single walled carbon nanotube (SWCNT) can be thought of as a sheet of graphene wrapped into a tube, so I will start by describing the tight-binding model of graphene [203]. Graphene is a regular 2D hexagonal Bravais lattice of carbon atoms and its structure is shown in Fig. 8.1. I label the unit vectors of the graphene lattice $\mathbf{a}_1$ and $\mathbf{a}_2$. The length of these vectors is the lattice constant a which is related to the distance between neighbouring carbon atoms, a_c, by $a = \sqrt{3}a_c \simeq 0.246\,\text{nm}$. Within each unit cell there are two carbon atoms, which are labeled to form the A and B sublattices. I can then define the unit vectors of the reciprocal lattice as $\mathbf{b}_1$ and $\mathbf{b}_2$, with $\mathbf{a}_i.\mathbf{b}_j = 2\pi\delta_{ij}$. The first Brillouin zone given by these is also hexagonal. It has a selection of points with high-symmetry; one at the centre, the midpoints of the hexagonal edges and two inequivalent types of corners.

The well-established tight-binding model assumes that the electrons are tightly bound to the individual carbon atoms and the localized atomic orbitals are used as

a basis for expanding the wavefunction. Only the orbitals that contribute to states that lie within an optical range of energies around the Fermi level are considered. These are the states that give the main contributions to the optical properties of the nanotube. Every carbon atom has four valence orbitals (2s, $2p_x$, $2p_y$ and $2p_z$) that could lie in this energy range. For 2D graphene the (s, p_x, p_y) orbitals combine to form hybridized sp^2 orbitals. These give the strong covalent bonds; primarily responsible for the binding energy and elastic properties of the nanotubes. In the tight-binding model they result in σ and σ^* bands. However, their energy levels are far away from the Fermi level and hence they do not play a key role in the optical properties that I am interested in. That role is played by delocalized π and π^* bands that are formed from the p_z orbitals [162]. Hence, I can ignore the σ electrons and restrict the tight-binding model to the π electrons. The Hamiltonian for this system is

$$\hat{H}_0 = -\gamma_0 \sum_{ij} (\hat{\alpha}_i^\dagger \hat{\beta}_j + h.c.), \tag{8.1}$$

where $-\gamma_0$ is the hopping amplitude and ij refers to nearest neighbors. Here, $\hat{\alpha}_i^\dagger$ and $\hat{\beta}_j^\dagger$ are the creation operators for electrons in sublattice A and B, respectively. In this Hamiltonian I have removed the constant energy contribution that corresponds to the Fermi level. I expand the wavefunction in terms of p_z orbitals at every atom site and split this expression into two parts; one for each sublattice. The wavefunction for each state is then

$$\Psi(\mathbf{k}, \mathbf{r}) = \sum_{\mathbf{r}_A} C_A(\mathbf{r}_A, \mathbf{k}) p_z(\mathbf{r} - \mathbf{r}_A) \tag{8.2}$$

$$+ \sum_{\mathbf{r}_B} C_B(\mathbf{r}_B, \mathbf{k}) p_z(\mathbf{r} - \mathbf{r}_B) \tag{8.3}$$

with $\mathbf{r}_A$,$\mathbf{r}_B$ labeling the atom locations in sublattice A and B, respectively. The individual p_z orbitals are given by the normalized wavefunctions $p_z(\mathbf{r})$ and each one

has a coefficient, represented with C_A and C_B. By using translational symmetry I can represent this as

$$\Psi(\mathbf{k},\mathbf{r}) = c_A(\mathbf{k})\tilde{p}_z^A(\mathbf{k},\mathbf{r}) + c_B(\mathbf{k})\tilde{p}_z^B(\mathbf{k},\mathbf{r}) \tag{8.4}$$

where the Bloch functions, $\tilde{p}_z^A$ and $\tilde{p}_z^B$, are

$$\tilde{p}_z^A(\mathbf{k},\mathbf{r}) = \frac{1}{\sqrt{N_{cells}}}\sum_{\mathbf{r}_A} \mathrm{e}^{\mathrm{i}\mathbf{k}.\mathbf{r}_A} p_z(\mathbf{r}-\mathbf{r}_A) \tag{8.5}$$

$$\tilde{p}_z^B(\mathbf{k},\mathbf{r}) = \frac{1}{\sqrt{N_{cells}}}\sum_{\mathbf{r}_B} \mathrm{e}^{\mathrm{i}\mathbf{k}.\mathbf{r}_B} p_z(\mathbf{r}-\mathbf{r}_B). \tag{8.6}$$

Here N_{cells} is the number of unit cells in the graphene sheet. These Bloch functions have the coefficients c_A and c_B. The states are labeled by their crystal momentum vector $\mathbf{k}$. I now solve the time-independent single-particle Schrödinger equation

$$\hat{H}_0\Psi(\mathbf{k},\mathbf{r}) = E(\mathbf{k})\Psi(\mathbf{k},\mathbf{r}). \tag{8.7}$$

I define the quantity

$$\phi_{\mathbf{k}} = \sum_{\mathbf{q}} \mathrm{e}^{\mathrm{i}\mathbf{k}.\mathbf{q}}, \tag{8.8}$$

where $\mathbf{q}$ are vectors from an atom in the A sublattice to its neighbouring atoms in the B lattice. This gives me the following quantities

$$\begin{aligned} H_{AA} = H_{BB} &= \langle \tilde{p}_z^A \,|\, \hat{H}_0 \,|\, \tilde{p}_z^A \rangle = \langle \tilde{p}_z^B \,|\, \hat{H}_0 \,|\, \tilde{p}_z^B \rangle = 0 \\ H_{AB} = H_{BA}^* &= \langle \tilde{p}_z^A \,|\, \hat{H}_0 \,|\, \tilde{p}_z^B \rangle = -\gamma_0\phi_{\mathbf{k}} \\ S_{AB} = S_{BA}^* &= \langle \tilde{p}_z^A | \tilde{p}_z^B \rangle = u\phi_{\mathbf{k}}. \end{aligned} \tag{8.9}$$

Now the variational Schrödinger equation in matrix form is

$$\begin{pmatrix} H_{AA} & H_{AB} \\ H_{BA} & H_{BB} \end{pmatrix} \begin{pmatrix} c_A \\ c_B \end{pmatrix} = E(\mathbf{k}) \begin{pmatrix} 1 & S_{AB} \\ S_{BA} & 1 \end{pmatrix} \begin{pmatrix} c_A \\ c_B \end{pmatrix}. \tag{8.10}$$

The above matrix equation can be solved to give the energy of each state as

$$E^{\pm}(\mathbf{k}) = \frac{\pm\gamma_0 \left|\phi_{\mathbf{k}}\right|}{1 \mp u \left|\phi_{\mathbf{k}}\right|}, \tag{8.11}$$

where

$$\left|\phi_{\mathbf{k}}\right| = \left[1 + 4\cos\left(\frac{k_x a\sqrt{3}}{2}\right)\cos\left(\frac{k_y a}{2}\right) + 4\cos^2\left(\frac{k_y a}{2}\right)\right]^{\frac{1}{2}}. \tag{8.12}$$

A typical value for γ_0 is 2.89eV such that the tight-binding model corresponds with experiments [204, 205, 164]. I will keep u in the equations but for all plots and numerical calculations I assume that $u = 0$; i.e., there is no orbital overlap. In Fig. 8.2 this 2D dispersion relation is plotted as a contour. In Eq. (8.11) the signs refer to the two relevant bands, the conduction band and the valence band. The coefficients are found to be

$$c_A^v(\mathbf{k}) = \sqrt{\frac{\phi_{\mathbf{k}}}{2\left|\phi_{\mathbf{k}}\right|\left(1 + u\left|\phi_{\mathbf{k}}\right|\right)}}, \tag{8.13}$$

$$c_B^v(\mathbf{k}) = \sqrt{\frac{\phi_{\mathbf{k}}^*}{2\left|\phi_{\mathbf{k}}\right|\left(1 + u\left|\phi_{\mathbf{k}}\right|\right)}}, \tag{8.14}$$

$$c_A^c(\mathbf{k}) = -\sqrt{\frac{\phi_{\mathbf{k}}}{2\left|\phi_{\mathbf{k}}\right|\left(1 - u\left|\phi_{\mathbf{k}}\right|\right)}}, \tag{8.15}$$

$$c_B^c(\mathbf{k}) = \sqrt{\frac{\phi_{\mathbf{k}}^*}{2\left|\phi_{\mathbf{k}}\right|\left(1 - u\left|\phi_{\mathbf{k}}\right|\right)}}. \tag{8.16}$$

Now that the relevant band structure of graphene and their wavefunctions is known, I need to obtain the energy states of the nanotubes. To do this I use the zone-folding approximation. This assumes the nanotube bands are the same as graphene but with limited $\mathbf{k}$, due to the 1D nature of a carbon nanotube.

For extremely small diameter nanotubes two further effects, that will be ignored here, need to be considered [162]. Firstly, the curvature causes the lengths and form of the bonds to change. This results in three different hopping terms and shifts the bands. Secondly, in extreme cases the curvature breaks the symmetry and allows the π and σ orbitals to mix. This gives the orbitals a partial sp^2 and sp^3 character. For nanotubes with a diameter greater than 1nm this rehybridization effect is unimportant. The shift to the band stucture relating the deformed bonds has an inverse square dependence to the nanotube's diameter. For tubes with a diameter of 3nm this shift is less than 0.1eV.

There are a variety of ways available to wrap the sheet up into a nanotube, each of which results in very different properties. The nanotubes are characterized by a vector in the graphene plane that corresponds to the circumference of the nanotube and is called the chiral vector $\mathbf{C} = n_1\mathbf{a}_1 + n_2\mathbf{a}_2$ ($0 \leq |n_2| \leq n_1$) (see Fig. 8.1). It gives the relative position of two graphene atoms that become "identical" when the graphene is rolled into a nanotube. I will use these parameters in the standard form (n_1, n_2) to label each type of nanotube. This immediately defines some basic geometric properties such as the tube's circumference and radius $R_t = a\sqrt{n_1^2 + n_1 n_2 + n_2^2}/2\pi$. The translational vector is defined as the vector, perpendicular to $\mathbf{C}$, that corresponds to the direction along the tube, $\mathbf{T} = t_1\mathbf{a}_1 + t_2\mathbf{a}_2$. Using the greatest common divisor (gcd), I define $t_1 = (2n_2 + n_1)/N_R$, $t_2 = -(2n_1 + n_2)/N_R$ and $N_R = \gcd(2n_1 + n_2, 2n_2 + n_1)$. The two vectors, $\mathbf{C}$ and $\mathbf{T}$, define the unit cell of the nanotube. Within each nanotube unit cell there are $N_G = 2(n_1^2 + n_1 n_2 + n_2^2)/N_R$ graphene unit cells and, hence, $N_C = 2N_G$ carbon atoms. In a nanotube of length L

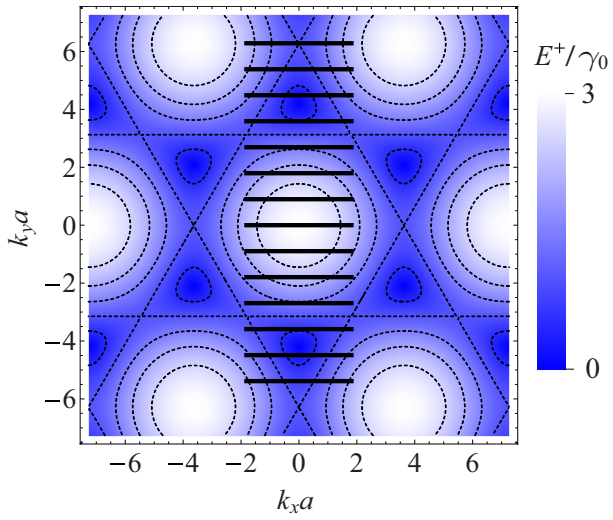

Figure 8.2: Graphene band structure and the locations of subbands for a (7,0) nanotube (black solid lines). The transitions between bands allowed with the electric field perpendicular to the nanotube can occur between neighbouring subbands. The dashed lines are contours for E^+/γ_0 equal to 0.5, 1, 1.5, 2, and 2.5.

there are $N_L = L/|\mathbf{T}|$ nanotube unit cells. For the nanotube's reciprocal lattice I define $\mathbf{K}_1 = (t_1\mathbf{b}_2 - t_2\mathbf{b}_1)/N_G$ and $\mathbf{K}_2 = (n_2\mathbf{b}_1 - n_1\mathbf{b}_2)/N_G$ such that $\mathbf{K}_1.\mathbf{T} = \mathbf{K}_2.\mathbf{C} = 0$ and $\mathbf{K}_1.\mathbf{C} = \mathbf{K}_2.\mathbf{T} = 2\pi$. These give the allowed vectors in the SWCNT's Brillouin zone to be a set of N_G 1D "cutting lines" with values

$$\mathbf{k} = \mu\mathbf{K}_1 + k_{||}\frac{\mathbf{K}_2}{|\mathbf{K}_2|}, \tag{8.17}$$

with $\mu = -N_G/2+1, \ldots, 0, \ldots, N_G/2$ and $-\pi/|\mathbf{T}| \leq k_{||} < \pi/|\mathbf{T}|$. It is the periodic boundary condition along the circumferential direction of the tube that causes the wave vector to become quantized and each discrete cutting line is labeled by the azimuthal quantum number μ. For short nanotubes the wave vectors are also quantized along the nanotube's length causing discrete energy levels to be formed [206]. These discrete values have $k_{||} = 2\pi j/L - \pi/|\mathbf{T}|$, for an integer $j = 1, \ldots, N_L$. Local effects also occur in short nanotubes, such as a sharp spike in the density of states (DOS), caused by defects at the caps. Such effects will be ignored here. Typically,

the nanotube is assumed to be of infinite length, allowing continuous values of the wave vector along the nanotube axis. This causes possible wave vectors to lie in "subbands". The subbands can cut through the Fermi points of graphene causing the tube to become metallic. This can be shown to be the case for nanotubes of the type (n, m), where $n - m$ is a multiple of three. If this is not the case there is a nonzero band gap and the nanotube is semiconducting. Here I consider "zigzag" semiconducting nanotubes of the form $(n, 0)$, with n not a multiple of three. The discrete wave vectors are then

$$|k_\perp| = \frac{2\pi\mu}{|\mathbf{C}|} \tag{8.18}$$

with $\mu = -(n-1), ..., 0, 1, 2, ..., n$ and

$$\left|k_{||}\right| < \frac{\pi}{|\mathbf{T}|}. \tag{8.19}$$

The momentum vectors associated with these subbands are highlighted in Fig. 8.2 for a (7,0) nanotube. For zigzag nanotubes $k_\perp$ corresponds to k_y and $k_{||}$ corresponds to k_x. It should be noted that subbands μ and $-\mu$ both have the same energy and this degeneracy is referred to as the "valley" degeneracy. Combined with the two electron spins this gives a degeneracy of four for each energy value, except for $\mu = 0$ and $\mu = n$ that only have spin degeneracy. The energy of the subbands is

$$E^{\pm}_{NT}(k_{||}, \mu) = E^{\pm}(k_{||}\frac{\mathbf{K}_2}{|\mathbf{K}_2|} + \mu\mathbf{K}_1) \tag{8.20}$$

These are plotted for a (7,0) nanotube in Fig. 8.3, which has a bandgap of 1.43eV.

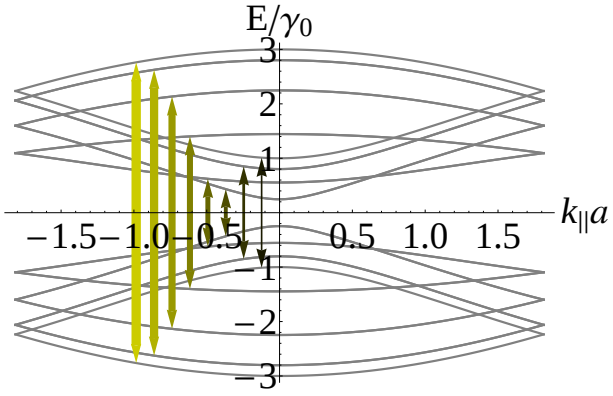

Figure 8.3: The dispersion relation for a (7,0) nanotube. The possible transitions caused by light linearly polarized parallel to the nanotube are shown by arrows. These arrows only represent the transition between subbands and their horizontal positions have no meaning. Here the bandgap is 1.43eV, when γ_0 is taken as 2.89eV.

8.3 The Optical Absorption of Carbon Nanotubes

The Hamiltonian of a nanotube interacting with an electromagnetic field is $\hat{H} = \hat{H}_0 + \hat{H}_\mathrm{F} + \hat{H}_\mathrm{I}$, with

$$\hat{H}_\mathrm{I} = \frac{e}{m_\mathrm{e}} \hat{\mathbf{A}}.\hat{\mathbf{p}}, \tag{8.21}$$

being the interaction term and $\hat{H}_\mathrm{F}$ representing the field Hamiltonian. Here, e is defined as the magnitude of the electron charge, m_e is the electron mass and I am using SI units. Each field mode is characterized by its angular frequency ω and further parameters, which define the mode's polarization and propagation direction. The field vector potential operator is

$$\hat{\mathbf{A}} = \int_0^\infty \mathrm{d}\omega (\hat{\mathbf{A}}_\omega^+ \mathrm{e}^{-\mathrm{i}\omega t} + \hat{\mathbf{A}}_\omega^- \mathrm{e}^{\mathrm{i}\omega t}). \tag{8.22}$$

I will consider the initial and final state of field to be a coherent monochromatic state $|\,\alpha_{\omega_0}\rangle$, with an angular frequency of ω_0 and a mean photon flux of F photons per unit time. This state satisfies the equation $\hat{a}_\omega\,|\,\alpha_{\omega_0}\rangle = \alpha\,|\,\alpha_{\omega_0}\rangle$, with $\alpha = \sqrt{2\pi F}\delta(\omega - \omega_0)$

and $\hat{a}_\omega$ being the field mode's destruction operator [207]. This allows me to give

$$\mathbf{A} = \langle \alpha_{\omega_0} \,|\, \hat{\mathbf{A}} \,|\, \alpha_{\omega_0} \rangle \tag{8.23}$$

$$= \mathbf{A}^{+} \mathrm{e}^{-\mathrm{i}\omega_0 t} + \mathbf{A}^{-} \mathrm{e}^{\mathrm{i}\omega_0 t}. \tag{8.24}$$

Using time-dependent perturbation theory I find that, after time t, the initial state of the nanotube and field, $|\, \Psi^{\mathrm{v}} \rangle \,|\, \alpha_{\omega_0} \rangle$, is in the state $|\, \Psi' c \rangle \,|\, \alpha_{\omega_0} \rangle$ with probability

$$P = t \frac{2\pi}{\hbar} \left| \langle \Psi' c \,|\, (\frac{e}{m_e} \mathbf{A}^{+}.\hat{\mathbf{p}}) \,|\, \Psi^{\mathrm{v}} \rangle \right|^2 \delta(E' - E - \hbar\omega_0), \tag{8.25}$$

which is Fermi's golden rule. The transition rate for each electron in the state with energy E to each state with energy E' can be expressed as

$$w = \frac{2\pi}{\hbar} \left| \frac{e}{m_e} \mathrm{i}\hbar G \right|^2 \delta(E' - E - \hbar\omega_0). \tag{8.26}$$

To calculate the optical absorption of a carbon nanotube of length L, the interaction term, $\mathrm{i}\hbar G = \mathrm{i}\hbar \langle \Psi' c \,|\, \mathbf{A}^{+}.\nabla \,|\, \Psi^{\mathrm{v}} \rangle$, needs to be found with spatially changing field. The state is assumed to be coherent over the entire length of the nanotube. To calculate G I define

$$\mathbf{v}^A(\mathbf{k}) = \sum_{\mathbf{q}} \mathrm{e}^{\mathrm{i}\mathbf{k}.\mathbf{q}} \mathbf{q}, \tag{8.27}$$

$$\mathbf{v}^B(\mathbf{k}) = -\sum_{\mathbf{q}} \mathrm{e}^{-\mathrm{i}\mathbf{k}.\mathbf{q}} \mathbf{q}, \tag{8.28}$$

with $\mathbf{q}$ summing over the three vectors pointing from an atom in the A sublattice to its neighbouring three B lattice atoms. I will furthermore use the matrix element, $M = \langle p_z(\mathbf{r}) \,|\, \nabla_z \,|\, p_z(\mathbf{r} - \mathbf{q}_z) \rangle$, with $\mathbf{q}_z$ being the vector between two neighbouring atoms such that the z-axis is aligned along $\mathbf{q}_z$. The value I will later use for this is

given by [186]

$$M = 2a\gamma_0 m_e/\hbar^2\sqrt{3}. \tag{8.29}$$

Each of the unit cells in the nanotube extends over a distance of $|\mathbf{T}| \approx 0.43\,\mathrm{nm}$ along the nanotube and approximately a nanometre across. This is much smaller than the light's wavelength and spatial variations. Therefore, I can assume that the electromagnetic field is constant across each of the nanotube's unit cells. There are N_L of these unit cells along the nanotube's length and in each one, labeled by an integer l, the field is given by $\mathbf{A}_l^+ = \mathbf{A}^+(l|\mathbf{T}| - L/2)$.

An expression for G can then be calculated and simplified into the form (see Appendix E)

$$G = \frac{1}{N_L}\mathbf{D}(\mathbf{k}', \mathbf{k}).\left[\sum_{l=1}^{N_L} \mathrm{e}^{\mathrm{i}(al\sqrt{3}-L/2)(k_{||}-k'_{||})}\mathbf{A}_l^+\right] \tag{8.30}$$

$$\approx \frac{1}{L}\mathbf{D}(\mathbf{k}', \mathbf{k}).\left[\int_{l=-L/2}^{L/2} dl \mathrm{e}^{\mathrm{i}l(k_{||}-k'_{||})}\mathbf{A}^+(l)\right], \tag{8.31}$$

where

$$\begin{aligned} D_z = \frac{M\sqrt{3}}{2an}\sum_{j=1}^{n}\Big[& c_A^{c*}(\mathbf{k}')c_B^v(\mathbf{k})\mathrm{e}^{-\mathrm{i}ja(k'_\perp - k_\perp)} \\ & (1+\mathrm{e}^{-\mathrm{i}a(\mathbf{k}'-\mathbf{k}).(\sqrt{3}/2,1/2)})v_z^A(\mathbf{k}) \\ & - c_B^{c*}(\mathbf{k}')c_A^v(\mathbf{k})\mathrm{e}^{-\mathrm{i}ja(k'_\perp - k_\perp)}\mathrm{e}^{-ia(k'_{||}-k_{||})/\sqrt{3}} \\ & (1+\mathrm{e}^{-\mathrm{i}a(\mathbf{k}'-\mathbf{k}).(\sqrt{3}/2,1/2)})v_z^A(\mathbf{k})^*\Big], \end{aligned} \tag{8.32}$$

and $D_{x,y}$ are given in Appendix E.

This result coincides with that of Ref. [179] when $\mathbf{A}_l^+$ is the same for all l. In Eq. (8.31) the $\mathbf{D}$ gives the selection rules for possible transitions between bands μ' and μ. In particular $D_z(\mathbf{k}', \mathbf{k})$ is negligible if $\mu' \neq \mu$ and for the other components

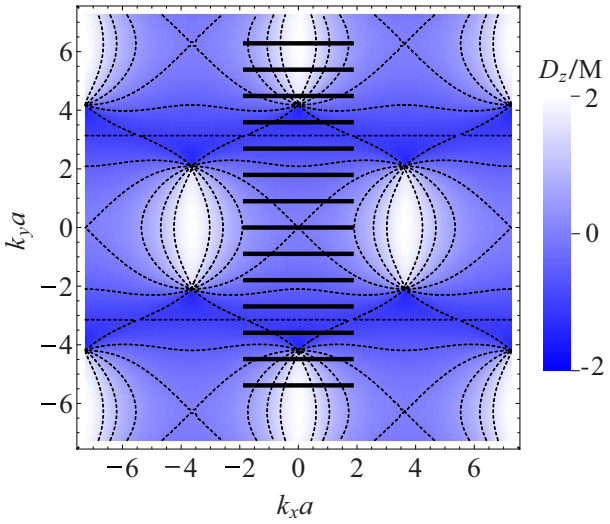

Figure 8.4: A density plot of $D_z(\mathbf{k}, \mathbf{k})$ for graphene is shown together with the nanotube's subband lines (black solid lines) and contours (dashed lines) for values of D_z/M equal to -1, -0.5, 0, 0.5, 1, and 1.5. It is given in terms of the constant M from Eq. (8.29).

of $\mathbf{D}(\mathbf{k}', \mathbf{k})$ to contribute it is required that $\mu' = \mu \pm 1$. For a uniform field across the nanotube these give the possible transitions for a field polarized parallel and perpendicular to the nanotube, respectively. In Fig. 8.4 I have plotted $D_z(\mathbf{k}, \mathbf{k})$, and in Fig. 8.5 $D_{x,z}$ is plotted. These expressions correspond to direct transitions, i.e, with $k'_{||} = k_{||}$, which is an approximation of momentum conservation and will be discussed later in this section.

Although the values of D_x and D_y show a transition, the induced local field creates a depolarization effect [208, 209, 210] that reduces D_x and D_y to give a negligible contribution to the absorption. This allows me to focus on the D_z term and simplify G to

$$G \approx \frac{1}{L} D_z(\mathbf{k}', \mathbf{k}) \left[\oint \mathbf{A}^+ . \mathbf{dr} e^{\mathrm{i}s(k_{||} - k'_{||})} \right], \tag{8.33}$$

with s denoting the length along the nanotube. This also restricts the transitions to those with $\mu' = \mu$.

It is the line integral in Eq. (8.33) that is responsible for momentum conservation

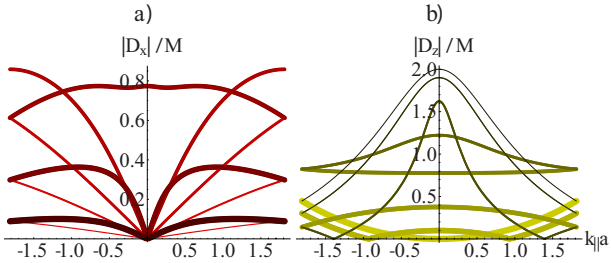

Figure 8.5: (a) D_x values for the different transitions that can occur when the electric field is perpendicular to the nanotube. M is given by Eq. (8.29). (b) D_z for transitions allowed with an electric field parallel to the nanotube. The thickness and colour for each transition has been made to match the arrows used in Fig. 8.3.

in the system. The photon momentum is much smaller than the crystal momentum and typically only direct transitions are considered; i.e., $k'_{||} \approx k_{||}$. Here I will make this assumption; however, the change in momentum cannot be completely neglected since any change can make a major difference to the line integral in Eq. (8.33). This is especially true when the field oscillates along the nanotube. The energy of a direct transition is given by $E_g(\mathbf{k}) = E^+(\mathbf{k}) - E^-(\mathbf{k})$. Since $D_z(\mathbf{k}', \mathbf{k}) \approx D_z(\mathbf{k}, \mathbf{k})$, when $k'_{||} \approx k_{||}$, I will make this substitution and further simplify $D_z(\mathbf{k}, \mathbf{k}) = D_z(\mathbf{k})$ to give

$$D_z(\mathbf{k}) = \frac{-M\sqrt{3}}{a} \mathrm{Re}\left(v_z^A(\mathbf{k}) \frac{\phi_{\mathbf{k}}^*}{|\phi_{\mathbf{k}}| \sqrt{1 - u^2 |\phi_{\mathbf{k}}|^2}} \right). \tag{8.34}$$

I define $A_{||}^+(s)ds = \mathbf{A}^+.\mathbf{dr}$ to be the field potential along the nanotube and use the discrete momentum values, $k_{||} = 2\pi j/L$ and $k'_{||} = 2\pi j'/L$, with integers j and j'. The line integral can then be expressed as

$$S(k_{||} - k'_{||}) = (1/L) \oint \mathbf{A}^+.\mathbf{dr} \mathrm{e}^{\mathrm{i}s(k_{||} - k'_{||})} \tag{8.35}$$

$$= (1/L) \int_{-L/2}^{L/2} ds A_{||}^+(s) \mathrm{e}^{\mathrm{i}s(k_{||} - k'_{||})} \tag{8.36}$$

$$= (1/L) \int_{-L/2}^{L/2} ds A_{||}^+(s) \mathrm{e}^{\mathrm{i}2\pi s(j - j')/L}. \tag{8.37}$$

This expression is simply the coefficient in the Fourier series for $A_{||}^{+}(s)$. Since the photon momentum is very small in comparison to the crystal momentum the only relevant coefficients will have very small values of $j' - j$ relative to N_L. Every electron transition in the nanotube then needs to be considered to calculate the overall absorption rate. This leads to a length dependence on the absorption. I initially consider discrete states and corresponding $k_{||}$ values. The transition rate given by Eq. (8.26) is summed over all possible initial and final states to give

$$w_L \approx \sum_{d_i} \sum_{\mu=-n+1}^{n} \sum_{k_{||}} \sum_{k'_{||}} \frac{2\pi\hbar e^2}{m_e^2} \left|D_z(\mathbf{k})\right|^2 \left|S(k_{||} - k'_{||})\right|^2 \delta(E_g(\mathbf{k}) - \hbar\omega_0). \tag{8.38}$$

In this equation d_i refer to the degeneracy of the initial state. For any value of $k_{||}$ the sum over $k'_{||}$ causes $k_{||} - k'_{||}$ to take all of the low values that are relevant. This sum is also independent of $k_{||}$ and allows me to define $Q = \sum_j \left|S(2\pi j/L)\right|^2$, which can be rewritten using Parseval's theorem to be

$$Q = (1/L) \int_{-L/2}^{L/2} ds \left|A_{||}^{+}(s)\right|^2. \tag{8.39}$$

The total absorption rate is then

$$w_L \approx \sum_{d_i} \sum_{\mu=-n+1}^{n} \sum_{k_{||}} \frac{2\pi\hbar e^2}{m_e^2} \left|D_z(\mathbf{k})\right|^2 Q\delta(E_g(\mathbf{k}) - \hbar\omega_0) \tag{8.40}$$

$$\approx U(\omega_0) \int_{-L/2}^{L/2} ds \left|A_{||}^{+}(s)\right|^2, \tag{8.41}$$

where I define

$$U(\omega_0) = \sum_{d_i} \sum_{\mu=-n+1}^{n} \int dk_{||} \frac{\hbar e^2}{m_e^2} \left| D_z(\mathbf{k}) \right|^2 \delta(E_g(\mathbf{k}) - \hbar\omega_0). \tag{8.42}$$

The field was defined to be a coherent state with a photon flux given by F photons per unit time. An estimate for the probability of one photon exciting a single electron can be obtained by dividing the transition rate, given in Eq. (8.41), by this flux. This expression gives a probability that increases linearly with nanotube length. This is certainly suitable up to the coherence length, L_c, however not for long nanotubes. So far I have considered the length of the nanotube to be smaller than the coherence length. For long nanotubes I can consider the whole nanotube to be composed of coherent segments. This leads to an exponential increase in the absorption with the nanotube length. Here, to calculate this quantity I find the probability of not exciting any electrons, which is the product of $(1 - w_{L_c}/F) \approx e^{-w_{L_c}/F}$ for each segment. Hence, the probability of exciting a single electron, in a nanotube of length L, with each photon can be estimated by the expression

$$\eta = 1 - \exp\left[\frac{-U(\omega_0)}{F} \int_{-L/2}^{L/2} \mathrm{d}s \left| A_{||}^{+}(s) \right|^2 \right]. \tag{8.43}$$

Note that this expression is actually independent of the coherence length.

Broadening effects can be included in this by substituting the Dirac delta function, from Eq. (8.42) with a Lorentzian function,

$$\delta(E_g - \hbar\omega) \to \frac{\Gamma}{\pi \left[(E_g - \hbar\omega)^2 + \Gamma^2 \right]}, \tag{8.44}$$

which has a broadening parameter, Γ. This parameter can include the broadening due to multiple effects, including the electronic state's decay. In carbon nanotubes the state decay occurs on a picosecond time scale [211]. If we take a range of 0.1ps

to 2ps the required broadening ranges from $\Gamma = 0.01$eV to $\Gamma = 0.001$eV. In order to compare my results with previous work [186, 212] I will choose in the following to use a parameter of $\Gamma = 0.01$eV.

So far I have assumed the light to be in a pure state consisting of one specific wavelength. Yet, a range of wavelengths is expected and to deal with this I assume the light is in a probabilistic mixture of coherent beams, each with a photon flux F. These are weighted by a lineshape $g(\omega)$, satisfying $\int d\omega g(\omega) = 1$. The light's state is then $\int d\omega g(\omega) \left|\, \alpha_\omega \right\rangle \left\langle \alpha_\omega \,\right|$ and the expected absorption probability is

$$\overline{\eta} = \int \mathrm{d}\omega g(\omega)\eta. \tag{8.45}$$

In the following I take g to be a uniform lineshape between two energy values. This is equivalent to taking $\overline{\eta}$ to be the average transition probability over a range of energies. My treatment is also approximately valid for coherent pulses over a short bandwidth.

8.4 Optical Nanofibre Photon Absorption into a Carbon Nanotube

I now extend the calculation for the absorption around optical fibres and particularly nanofibres [213, 214]. A review of these subwavelength diameter waveguides can be found in Refs. [215, 216, 217]. They are made of a silica core and have diameters as small as 50 nm. For fibres of this size a high proportion of the light field exists outside of the fibre's core. This means the field is easily accessible and I consider positioning the carbon nanotube near the nanofibre. The use of fibres allows the interaction to be enhanced due to the transverse confinement of the field. Altering the nanofibres properties also allows the field to be tailored. Fibres with a smaller

diameter have a larger evanescent field but also suffer from higher losses. I will consider a cylindrical nanofibre core with a radius of R and cladding provided by the vacuum, with refractive index $n_2 = 1$. The refractive index of the silica core is $n_1 = 1.45$ and the material absorption of the silica is negligible over the short distances being considered. Silica core fibres with subwavelength diameter are single mode fibres, i.e. the only mode present is the HE fundamental mode (see Ref. [217] for a general single mode condition). I make the assumption that the field can be described by the bare fibre mode. In order to validate this assumption I have shown that the nanotube's influence on the field is small. To do this I treated the nanotube as a dielectric cylinder, acting as a separate waveguide, and analysed the combined mode of the system, using methods based on those found in Ref. [218]. In the following I will adopt a scheme used in Refs. [195, 207] to quantize the field. The field potential operator for the nanofibre's fundamental mode is then

$$\hat{\mathbf{A}}_\omega^+ = \sum_{fp} \sqrt{\frac{\hbar\beta'}{4\pi\omega\epsilon_0 A}}\hat{a}_m \mathbf{e}^m(r,\varphi)\mathrm{e}^{\mathrm{i}(f\beta z + p\varphi)}. \tag{8.46}$$

This is given in terms of cylindrical coordinates, with z being the coordinate along the fibre and φ the azimuthal angle. The light's angular frequency is ω. Its propagation direction is labeled with $f = \pm 1$ and β refers to the longitudinal propagation constant. I found the value of β by numerically solving the fibre eigenvalue equation (see Eq. (D.1) in Appendix D). The derivative in Eq. (8.46), β', is taken with respect to ω, and $\hat{a}_m$ are the photon annihilation operators, with $m = (\omega, f, p)$ characterizing the separate modes. Furthermore, $\mathbf{e}^m$ are the electric field profiles of the guided mode that can be found by solving Maxwell's equations [219, 195] and A gives a normalization factor. The expressions for the mode profiles and A are given in Appendix D. The polarization can be right or left circular labeled by $p = \pm 1$.

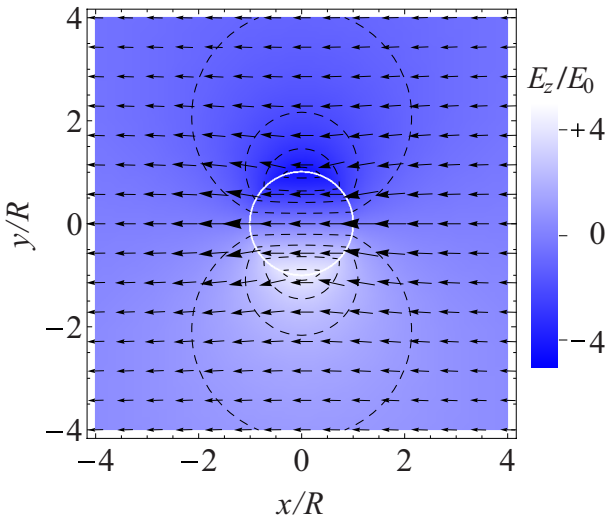

Figure 8.6: The electric field **E** of the circularly polarized HE mode taken for a constant z, to give a cross-section of the fibre. The colour gives E_z and the arrows represent the x and y components. The longer the arrow the stronger the field. The field has been divided by the constant $E_0 = \sqrt{F\omega_0\hbar\beta'/(2\epsilon_0 A)}$. Contours (dashed line) for values of E_z/E_0 equal to $\pm 4, \pm 3, \pm 2$ and ± 1 have been included. In this particular case the fibre diameter was taken to be 250nm and the light's wavelength as 868nm.

For a single mode of monochromatic coherent light with $m = (\omega_0, f, p)$ I have

$$\mathbf{A}^+ = \sqrt{\frac{F\hbar\beta'}{2\omega_0\epsilon_0 A}}\mathbf{e}^m(r,\varphi)\mathrm{e}^{\mathrm{i}(f\beta z + p\varphi)}. \tag{8.47}$$

Figure 8.6 provides a slice of the classical field at one instant in time. This field can be seen to extend far away from the nanofibre and vary dramatically with position.

This contrasts with the simpler case, that has previously been studied, of a plane linearly polarized light beam that is given by

$$\hat{\mathbf{A}}^+_\omega = \sqrt{\frac{\hbar}{4\pi\omega\epsilon_0 c A'}}\hat{a}_\omega \mathbf{e}_z, \tag{8.48}$$

across the whole nanotube, where the beam has a finite cross-sectional area of A'.

This gives

$$\mathbf{A}^{+} = \sqrt{\frac{F\hbar}{2\omega_0\epsilon_0 cA'}}\mathbf{e}_z. \tag{8.49}$$

For fibres larger than 100 nm in diameter the photon losses are small and can be ignored over short distances. In my calculations I will use nanofibres of diameter 250 nm. Furthermore, I will focus on the forward propagation and right polarized guided modes, *i. e.* $f = p = +1$. All other modes are related to my results by symmetry. The value of G is then highly dependent on the way the nanotube is orientated relative to the nanofibre and can be calculated to be

$$G = \sqrt{\frac{F\hbar\beta'}{2\omega_0\epsilon_0 A}} \langle \Psi^c(\mathbf{k}') \,|\, \mathbf{e}^m \exp^{\mathrm{i}(f\beta z + p\varphi)} . \nabla \,|\, \Psi^v(\mathbf{k}) \rangle \,. \tag{8.50}$$

Since the field strength drops off exponentially the highest value for the coupling will be achieved by having the nanotube as close as possible to the fibre. In my examples, the distance between the nanotube's centre and the surface of the nanofibre is chosen to be 1.25 nm. The nanotubes considered always have a radius less than 1 nm so this distance avoids any contact. This is so that surface interactions can be ignored. These interactions can influence the band structure, particularly by distorting the structure of the nanotube, and may change the nanotube's transport properties. The band structure would still experience a shift due to the Van der Waals interactions. However, even in the case of a nanotube placed directly on top of a substrate, with distortion, the bands are shifted by less than 100meV [220].

There are two orientations I will consider. The first is that of a straight nanotube, of length L, oriented at an angle ϕ relative to the nanofibre which includes parallel and perpendicular orientations as illustrated in Fig. 8.7. For 2μm nanotubes perpendicular to the fibre, the absorption probabilities as defined by Eq. (8.43) for different

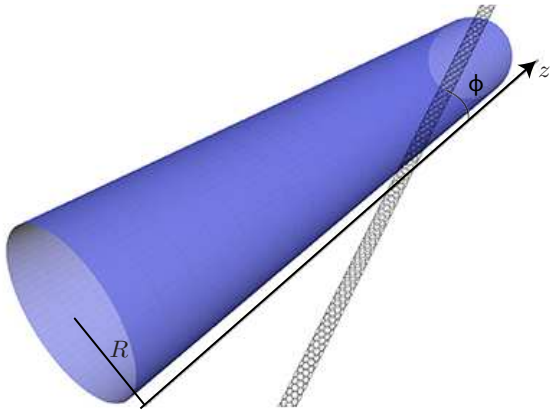

Figure 8.7: Possible orientations of a straight nanotube relative to a fibre of radius R and positioned parallel to the z axis. ϕ labels the angle between the nanofibre and nanotube.

wavelengths of light and different zigzag nanotubes are shown in Fig. 8.8. I do not consider the absorption of photons with energies greater than 6eV since these are not visible and require the addition of the higher energy σ orbitals for accurate results. Distinct absorption peaks are clearly visible and the largest absorption occurs for a (11,0) nanotube. The absorption for a nanotube in a linearly polarized coherent plane wave [see Eq. (8.48)] is also shown in Fig. 8.8. This beam has a cross-sectional area of $4\mu\text{m}^2$ and exhibits the same absorption peaks as the fibre, but varies less with the light's frequency. It can be seen that the (11,0) nanotube has its smallest energy transition dramatically reduced. This extra effect is caused due to larger evanescent fields, for an increasing wavelength relative to the fibre radius. This reduces the field intensity and absorption. The quantum efficiencies are a similar order of magnitude as those observed experimentally for plane waves [177, 210, 221]. The different nanotubes show shifted absorption peaks. These can be further adjusted with external fields or choosing other nanotubes [167, 168, 169]. The resonant energy values are unchanged with the orientation and this allows me to choose a range to average over as a general measure of absorption. I chose to calculate the mean absorption $\bar{\eta}$ over the (7,0) nanotube's lowest absorption energy, particularly

I chose a range of 1eV from 1.3eV (953nm) to 2.3eV (539nm). The resulting $\bar{\eta}$ is approximately independent of Γ in a range of $\Gamma = 0.01$eV to $\Gamma = 0.001$eV deviating only by a few percent.

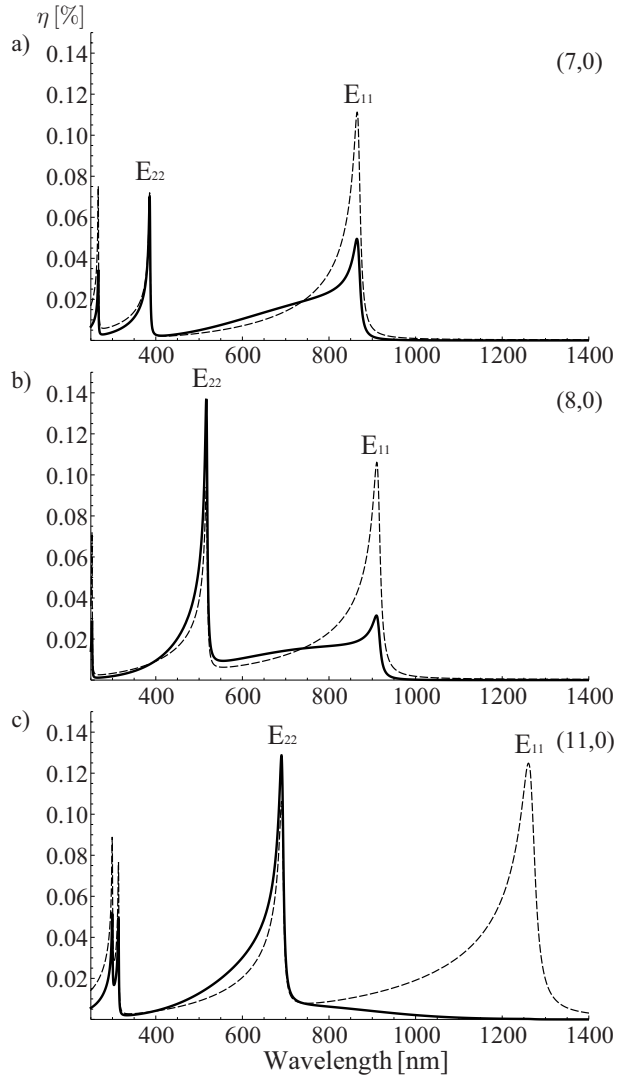

Figure 8.8: Photon absorption probabilities, η, for a $2\,\mu$m long nanotube, perpendicular to the fibre, at different photon energies. The nanotubes considered are (a) (7,0) (b) (8,0) and (c) (11,0). In each case the solid lines refer to the absorption of circularly polarized light guided by the nanofibre and the dashed lines represent the absorption for a plane coherent light beam (without a fibre) that is linearly polarized along the nanotube. The two lowest energy transitions, E_{11} and E_{22}, are indicated. A broadening parameter of $\Gamma = 0.01\,$eV was used.

The corresponding mean absorption against nanotube length, for the lowest en-

ergy transition, is shown in Fig. 8.9 for various angles between the straight nanotube and nanofibre. The results show that the absorption converges to a maximum value as the length is increased, unless the nanotube is parallel to the fibre. The nanotube perpendicular to the fibre has a very strong absorption for short lengths. In this situation we see the absorption increasing strongly with nanotube length which is due to the linear increase in electron number. As the length increases further this effect is counterbalanced by the fact that the field strength decreases exponentially away from the nanofibre. The absorption hardly increases at all after the nanotube exceeds approximately $2\,\mu$m. However, over these short distances the absorption of the perpendicular nanotube can be improved upon by shifting the nanotube slightly away from a perfectly perpendicular arrangement. The parallel orientation increases slowly but does not peak. This effect will be discussed later in this section and I will find that the probability can be enhanced by spiralling the nanotube to combine both effects. This can be qualitatively understood by noting that the evanescent field is elliptically polarized, however the plane containing the ellipse is not perpendicular to the fibre. Instead, it is inclined so the absorption is enhanced by aligning the nanotube such that it lies within the plane. If linear polarized light was used instead of circular polarized light the absorption could be twice as high depending on the nanotube's position in the nanofibre plane. We also see a difference between angles of $\pm\pi/32$, with the higher absorption being dependent on the light's polarization and propagation.

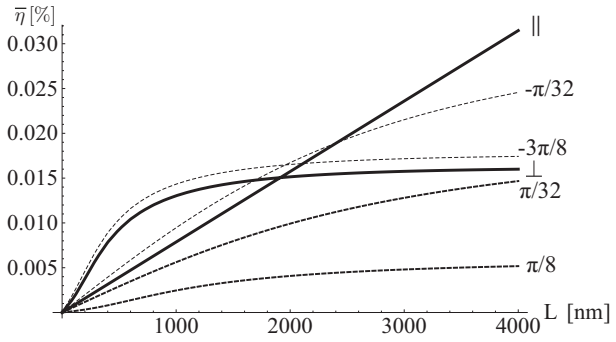

Figure 8.9: Average photon absorption probability, $\overline{\eta}$, for a straight (7,0) nanotube of length L. At $L = 4\mu$m the angles between nanotube and fibre are $\phi = 0$ (parallel), $-\pi/32$, $-3\pi/8$, $\pi/2$ (perpendicular), $\pi/32$, $\pi/8$. The mean absorption has been taken over a 1eV region, from 1.3eV to 2.3eV.

The strong absorption for a perpendicular nanotube is limited by the drop-off in field strength. However, this can be prevented by maintaining a constant distance between the nanotube and nanofibre centre, R_n. The nanotube can locally approximate a perpendicular nanotube by spiralling around the nanofibre, as illustrated in Fig. 8.10. Although this bending does alter the electronic and optical properties these effects are small and can be safely ignored here [222]. I define a "winding number", W, for the spiral as the number of loops per unit length along the z axis. This winding number is equal to $W = 1/d_{\mathrm{l}}$ where d_{l} is the z-distance for one loop. An angle is also formed between the spiralling nanotube and the nanofibre's direction, which is given by $\Phi_{\mathrm{s}} = \arctan(2\pi W R_n)$. Since these spiralling nanotubes can interact with the field over an arbitrary length their absorption's approach 100% given sufficient length and an allowed transition.

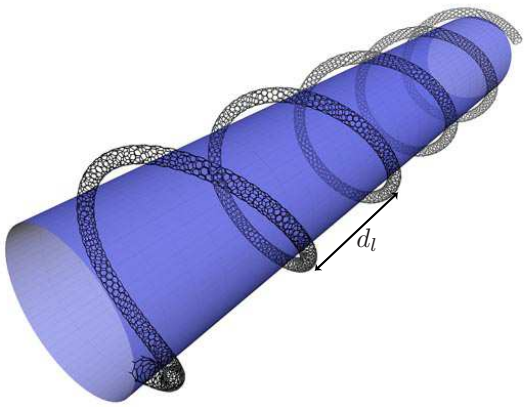

Figure 8.10: Nanotube spiralling around a nanofibre. The length of one loop, along the z axis, is labeled as d_l.

The average absorption probabilities in this case are plotted in Fig. 8.11 and show a steady increase in the absorption probability with nanotube length. The parallel nanotube is also shown. This demonstrates that the spiralling nanotubes can have higher absorption probabilities than the parallel configuration. In Fig. 8.12 I have plotted the average absorption probability against Φ_s for nanotubes of different lengths. An optimal spiralling rate to enhance the absorption can be seen. I found that the optimal value of this winding rate is $W_{\text{opt}} = e_\varphi^m/(2\pi R_n e_z^m)$. This was obtained by maximizing the alignment between the nanotube and $\mathbf{e}^m$. Note that W_{opt}, and hence the optimal Φ_s, is independent of the nanotube used. There is also another coil that lies perpendicular to the optimal one and has near zero absorption. Such nanotubes could have a variety of applications. For example, two semiconducting nanotubes could be prepared to give near zero absorption for different polarizations of light and then used to distinguish between these polarizations. They would also enable systems of nanotubes to be used as electrical conductors, around the nanofibre, without absorbing photons from the fibre and these could be used as contacts.

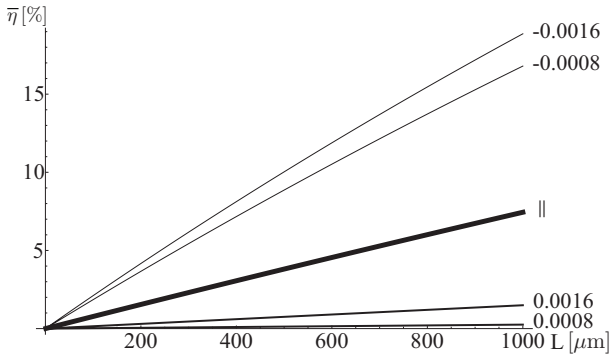

Figure 8.11: Average photon absorption probability, $\overline{\eta}$, for a (7,0) nanotube of length L coiled around the fibre. The average is taken from 1.3eV to 2.3eV. The winding numbers are $-0.0016\,\mathrm{nm}^{-1}$, $-0.0008\,\mathrm{nm}^{-1}$, $0\,\mathrm{nm}^{-1}$(Parallel), $0.0016\,\mathrm{nm}^{-1}$ and $0.0008\,\mathrm{nm}^{-1}$.

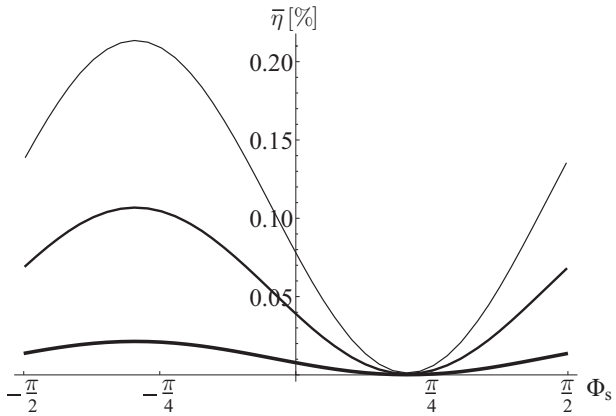

Figure 8.12: Average photon absorption probability, $\overline{\eta}$, for (7,0) nanotubes coiled around the fibre for different winding parameters. From top to bottom the nanotubes have lengths 10000nm, 5000nm and 1000nm. The average is taken from 1.3eV to 2.3eV.

8.5 Applications

The nanotube-nanofibre setups that I have introduced open up possibilities for a range of applications, particularly highly sensitive photodetectors. As we have seen, such photodetectors are essential for all entanglement distribution protocols including quantum repeaters. My system would detect light guided within a fibre and in this section I discuss these possibilities. Note that I have only considered the

quantum efficiency of the absorption and that detection of the charge excitations is still an area for further research. The full efficiency will be limited by our ability to detect the excitation before it disappears, despite noise, and any loss in the fibre. However, certain nanotube properties such as ballistic electron transport and low capacitance should be a great advantage for this detection. By designing the fibre taper it is also possible to adiabatically couple light from an ordinary optical fibre into the nanofibre with low loss (< 0.1dB/mm) [223, 215]. The bandgap of carbon nanotubes decreases with the nanotube size, so for optical and near infrared wavelengths small diameter nanotubes are required. This rules out the possibility of encasing a nanofibre within a nanotube. Instead, a practical setup is given by arranging N horizontal nanotubes in a parallel array and placing the nanofibre orthogonally on top of the array (see Fig. 8.13(a)).

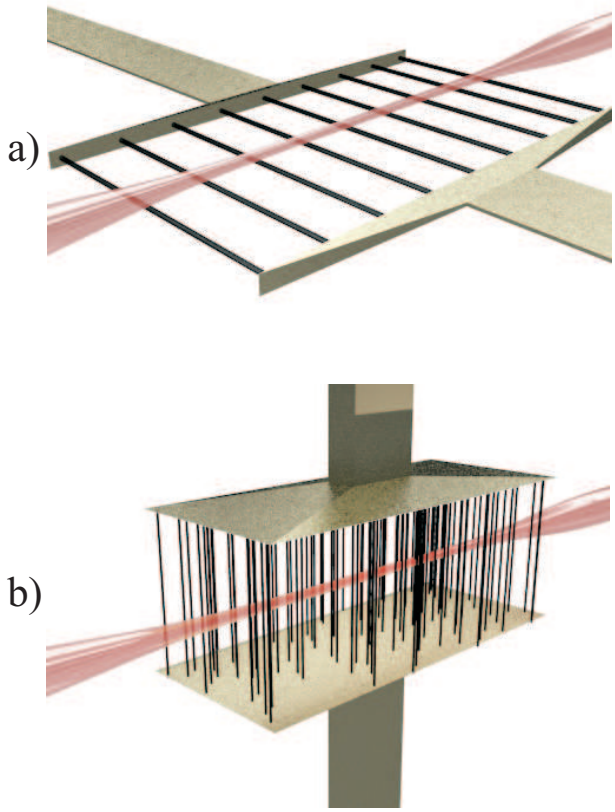

Figure 8.13: Illustrations of possible photodetectors. Once the light field excites an electron the resistance between the electrodes drops dramatically, which allows the photon to be recorded. (a) A horizontal array of aligned nanotubes (thick dark lines) are formed between two electrodes and the nanofibre is then laid perpendicular to these nanotubes. (b) Here a "forest" of aligned semiconducting nanotubes are grown between two electrodes. The nanofibre is positioned between these electrodes.

Based on current nanotube arrays, the density of nanotubes would be $1-100$ nanotubes per μm [224, 225, 226, 227, 228]. I will use $\overline{\eta}$ as a measure of the absorption probability for one nanotube. The photon absorption probability of each nanotube is then, in the case of a (7,0) nanotube, given in Fig. 8.9 and the overall absorption probability is

$$\eta_{\text{tot}} = 1 - (1 - \overline{\eta})^N. \tag{8.51}$$

Taking $\overline{\eta} = 0.00015$ (see Fig. 8.9) this leads to $\eta_{\text{tot}} > 95\%$ for $N > 20000$, a value greatly exceeding those of currently available APDs [113]. For $N > 40000$ the

efficiency exceeds 99% which can currently only be achieved by highly complex superconducting detectors [113]. The advantage of my setup is that it can be operated at room temperature. Each nanotube would require a length of 2μm and has to be connected at the ends by electrodes [229] which collect the excited electrons via an applied voltage. Although this should be possible in the near future, current technology cannot generate an array of unique nanotubes.

Aligned vertical nanotubes can also be grown on a conducting substrate, which can then serve as one electrode. The nanofibre can then be placed orthogonally to the nanotubes and the remaining ends of the nanotubes connected to an additional electrode (see Fig. 8.13(b)). The diameter of the nanotubes in this case can be in the range of 1 ± 0.5 nm [230, 231]. Recently, progress has been made in the generation of such semiconducting nanotube "forests", although a semiconducting nanotube purity of 100% has yet to be achieved reliably [232, 233, 234]. These nanotube systems typically have a density of $10 - 10000$ nanotubes per μm^2 [235, 236, 237, 238]. The nanotubes are distributed uniformly over a selected region and I assume that they are a uniform mix of semiconducting zigzag nanotubes with a diameter in the range 1 ± 0.5 nm. I calculated the overall absorption probability when with a forest that extends a distance of 500nm from the nanofibre and 15 μm along its length, with a density of 900 nanotubes per μm^2. The results for nanofibres that have diameters of 250 nm and 400 nm are shown in Fig. 8.14. These absorb light of a wide range of wavelengths, which can be selected by the nanotubes present and choice of nanofibre diameter. A typical absorption probability of $\eta_{tot} > 50\%$ can be seen, for 250 nm diameter fibres, and by extending the system's length from 15 μm to 50 μm this is increased to $\eta_{tot} > 95\%$. Nanotubes around a 400 nm fibre are also seen to absorb light at wavelengths that are typically used for optical communication. Due to the nanotube's bandgap dependence on external fields there is also the possibility of adjusting the absorption frequencies by using an external field.

An additional possible setup is given by arranging the nanofibre and the nanotube parallel to each other. Taking 100 nanotubes of length $L = 1\,\mathrm{mm}$ parallel to the fibre and using $\overline{\eta} = 0.07$ (see Fig. 8.11) I obtain an overall absorption probability of $\eta_{tot} > 99\%$ which again greatly exceeds that of standard APDs.

As a final setup I considered the coil geometry shown in Fig. 8.10 which has a high absorption probability of up to 100% for long nanotubes. However, producing such a setup in a laboratory is rather challenging with current technology. This setup also allows for further specification of the absorbed light's polarization or propagation direction with the choice of winding number. The winding also dramatically reduces the length of the system. For a nanotube with a winding number of $W = -0.1\,\mathrm{nm}^{-1}$, the average absorption between 1.5eV and 2.5eV exceeds 50% when the nanotube's length is 5 mm. For the 250 nm diameter fibre this only extends 64 μm along the fibre.

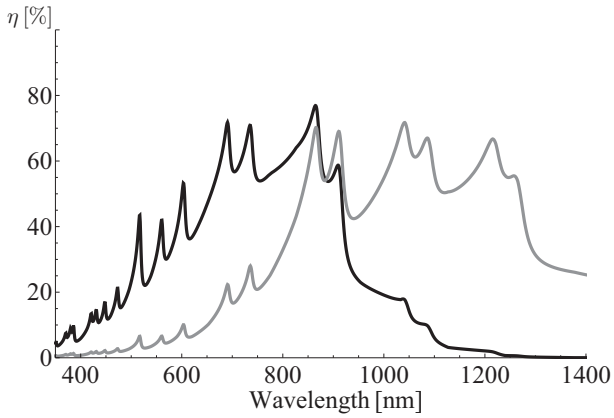

Figure 8.14: Absorption probability for a circularly polarized photon in a nanofibre laid inside a "forest" of nanotubes (see Fig. 8.13). This is given for 2 μm long vertically aligned nanotubes. The nanotubes are in a region that extends 500nm away from the fibre and 15μm along its length. The density of the array is taken as 900 nanotubes per $\mu\mathrm{m}^2$. The fibres diameter is taken to be either 250 nm (black line) or 400 nm (gray line). A broadening parameter of $\Gamma = 0.01\,\mathrm{eV}$ was used.

8.6 Chapter Summary

In this chapter I have calculated the probability of absorbing a photon with zigzag carbon nanotubes. The light field is allowed to vary along the nanotube, i.e. no dipole approximation is made, which has enabled me to treat the absorption of light from optical nanofibres. I found that there is a strong dependence on the system's geometry and have devised setups for high absorption. With a sufficiently long nanotube parallel to the nanofibre, I found that an absorption of circularly polarized light, arbitrarily close to 100% can be achieved. This can be further improved on if we spiral the nanotube around the fibre so that the required nanotube length is dramatically reduced. A coiled nanotube can also be engineered so that it does not absorb any light from the nanofibre. For straight nanotubes, that are not parallel to the fibre, I found that the absorption probability converges as the nanotube's length increases. However, if multiple perpendicular nanotubes are arranged parallel to the fibre arbitrary absorption can still be achieved. I have found a simple expression for the absorption probability, which is independent of the coherence length. Once excited, the radiative lifetimes of the excitations have been observed to range from 3 to 100 ns [189, 239]. The nonradiative decay seems to be much faster, of the order of a few picoseconds [211]. As a highly efficient photodetector that could operate at room temperature and over a broad frequency range, this proposed system would prove an important addition to implementations of entanglement distribution protocols. However, this is only a first step to demonstrating the application of the system to quantum processing. If the absorption process is coherent the system could be suitable as a quantum memory, which maps a photonic quantum state on to a coherent excitation of the nanotube. It has been suggested that carbon nanotube systems hold promise for applications in quantum optics and there have been studies in regards to performing coherent spintronics in nanotube systems [240, 241].

Chapter 9

Conclusion

The efficient distribution of entanglement is a key requirement for quantum information processing and specifically quantum communication. During this thesis I have outlined the basic concepts that aid in achieving this and given a short introduction to the favoured methods provided by quantum repeaters. Although promising, these methods still suffer many limitations and do not make use of any network structure.

It was shown by Acín et al that, with pure states, the extra connectivity present in networks could be used to give a fundamentally different resource scaling based on percolation procedures. However, this work did not address systems composed of mixed states that would come about from the prevalence of decoherence and dissipation in real world systems. In this thesis I have given the first example of an entanglement percolation algorithm that could be applied to a network of mixed states. This demonstrated that mixed states do not provide a clear limitation on long distance entanglement distribution. The protocol could only be applied on specific mixed states and assumed that the gate operations were noise free.

Following on from mixed state entanglement percolation other methods for long distance entanglement distribution within a square network were found to work [64].

These procedures were also restricted to rank-two states. I generalized the procedure found in Ref. [64] to be applied to any network geometry. This procedure uses loops in the network to correct errors. By allowing this to work on an arbitrary geometry I was able to apply it to a percolated network. Together with my previous entanglement distribution scheme this revealed that long distance entanglement distribution was possible with rank-three mixed states.

The restriction on the form of the mixed states can be addressed by using error correcting codes or decoherence free subspaces to reduce the errors that are not addressed by the network procedure. This results in a logarithmic scaling of the entanglement resources with distance between the target nodes. Although this is the same as the best repeater schemes the network procedures avoid the delays due to waiting for a heralded entangled state and allow greater freedom in the resulting entanglement. The resulting entangled states can link any two nodes in a network or be multipartite. Entanglement percolation also enables more than one entangled pair to be generated in each run.

My proposed mixed state long distance entanglement distribution schemes are not necessarily optimal. I have demonstrated that classical entanglement percolation can be improved upon for specific network structures in a similar way as to those shown for pure states. This means that it is not optimal for certain tasks. In doing this I have highlighted how these preprocessing manipulations are trading off properties. For pure states further schemes, including some multipartite strategies, have since been proposed [61].

For general networks, work on assisted entanglement has revealed results for calculating the capacity of entanglement distribution with almost unlimited local processing and entangled resources [54]. Yet, with limited resources, a complete understanding of the theoretical properties of entanglement distribution in quantum networks is still lacking and there are many unanswered questions. Optimal strate-

gies are only known for simple networks. Even for regular networks of pure states it is unknown whether there is a necessary amount of initial entanglement needed in the edges for long distance entanglement distribution.

Further work on demonstrating entanglement distribution in mixed state networks is also required to show when long distance entanglement distribution is indeed possible. I derived a fundamental restriction on the types of initial states that can be used to distribute a perfect singlet. This is an intriguing theoretical result although it does not rule out the generation of mixed entangled states that are almost indistinguishable from a perfect singlet. In this situation only a weak condition, based on the Lewenstein-Sanpera decomposition [151] and percolation, is known to restrict the necessary states suitable for long distance entanglement distribution.

Recently, more planar network protocols have been introduced and for higher dimensional networks it has been shown that full rank Werner states can be used for long distance entanglement distribution [242]. To allow this the surface code entanglement distribution found in Ref. [143] was used to create two entangled distant surface codes that could then be reduced to entanglement between nodes. If this procedure is projected to a square network the local resources must still scale logarithmically. Another scheme has also been introduced that allows for constant local resources but has a logarithmic temporal scaling with time [243]. Very recently, a proposal has been made to map the problem of entanglement distribution to that of fault tolerant quantum computing on a one dimensional array, with nearest neighbour interactions [244]. By doing this it is claimed that long distance entanglement distribution is possible on an infinite square network containing Werner states [245]. However, like fault-tolerant quantum computing the required initial state fidelities are restrictive. A review of recent progress can be found in Ref. [246].

The results obtained offer at least a logarithmic scaling with distance and high rates. Unfortunately, even the simplest quantum repeater has yet to be realized

experimentally. A means to store and process photonic qubits is the primary requirement of any entanglement distribution realization. A great deal of progress has been made in providing quantum memories. I have introduced a new coupling device that could help to realize photo-detectors and possibly quantum memories within quantum networks.

Appendix A

Proof of Singlet Distillation Requirement

In this appendix we give a concise proof for a necessary and sufficient condition to be able to create a singlet out of entangled mixed states using LOCC. We allow the states to be arbitrary two-qubit states which are shared between two nodes and all operations are LOCC. A similar proof, but partly restricted to identical states, was given in [148].

If a quantum state ρ_{ab} can be distilled to a pure state, $|\,\Psi\rangle$, then any state with the same range $R(\rho_{ab})$ is also distillable to this state with nonzero probability.

The general form of the state is

$$\rho_{ab} = \sum_{i=1}^{N} p_i \,|\,\psi_i\rangle\,\langle\psi_i\,|\,, \tag{A.1}$$

with $p_i > 0$, $\sum_i p_i = 1$ and $|\,\psi_i\rangle \in H_A \otimes H_B$. If the state is distillable to a pure state, $|\,\Psi\rangle$, there exist linear operators M_A and N_B, with $M_A M_A^\dagger \leq I, N_B N_B^\dagger \leq I$,

such that

$$M_A \otimes N_B \rho_{ab} M_A^\dagger \otimes N_B^\dagger = p \,|\, \Psi\rangle \langle \Psi \,| \tag{A.2}$$

$$\Rightarrow M_A \otimes N_B \,|\, \psi_i\rangle \langle \psi_i \,| \, M_A^\dagger \otimes N_B^\dagger \propto |\, \Psi\rangle \langle \Psi \,| \tag{A.3}$$

or

$$M_A \otimes N_B \,|\, \psi_i\rangle \langle \psi_i \,| \, M_A^\dagger \otimes N_B^\dagger = 0. \tag{A.4}$$

This can be summarized as

$$\Rightarrow M_A \otimes N_B \,|\, \psi_i\rangle = q_i \,|\, \Psi\rangle \,, \tag{A.5}$$

where at least one q_i is nonzero as otherwise the operator fails to distill ρ_{ab}. If this condition is satisfied the operation distills the mixed state into $|\, \Psi\rangle$. Now given another state $\tilde{\rho_{ab}}$ with the same range as ρ_{ab}. We have that

$$\tilde{\rho_{ab}} = \sum_{i=1}^{M} \tilde{p}_i \left| \tilde{\psi}_i \right\rangle \left\langle \tilde{\psi}_i \right| \tag{A.6}$$

with $\left| \tilde{\psi}_i \right\rangle = \sum_{j=0}^{N} a_{i,j} \,|\, \psi_j\rangle$ and $|\, \psi_i\rangle = \sum_{j=0}^{M} b_{i,j} \left| \tilde{\psi}_i \right\rangle$. This then gives

$$M_A \otimes N_B \left| \tilde{\psi}_i \right\rangle = M_A \otimes N_B \sum_{j=0}^{N} a_{i,j} \,|\, \psi_j\rangle \tag{A.7}$$

$$= \sum_{j=0}^{N} a_{i,j} q_j \,|\, \Psi\rangle = \tilde{q}_i \,|\, \Psi\rangle \,. \tag{A.8}$$

The value of one $\tilde{q}_i$ must be nonzero as otherwise all q_i are zero and this contradicts the fact that the operator distills ρ_{ab}. Hence, the protocol also distills $\tilde{\rho_{ab}}$.

For n two-qubit states to be distillable into a pure singlet at least two two-qubit states cannot have a range spanned by product states.

If a two-qubit state has a range that can be spanned by product states then a separable state with this range exists. If there are n states each with a range spanned by product states the system state would have a range equivalent to a separable state formed by all of these two-qubit separable states. Since it is impossible to distill a pure entangled state from any separable state it is impossible to distill a pure entangled state from n two qubit states each with a range spanned by product states. Similarly, if one of the two-qubit states does not have a range spanned by product states, but all of the other states do, the range is equivalent to the range formed from a separable state and one mixed two-qubit state. This can not be distilled into a pure two-qubit singlet as it would contradict the result in [149]. Hence, at least two states can not have a range spanned by product states to be able to distill a pure singlet.

We now need to look at the two qubit states that satisfy this property. The states with rank one are already pure and if they have rank four the range can be spanned by product states. Similarly, if the state has rank three it can also be spanned by product states. This can be seen by considering the subspace orthogonal to a general state $\sqrt{\alpha}\,|\,00\rangle + \sqrt{1-\alpha}\,|\,11\rangle$. This space is spanned by $\{|\,01\rangle\,,\,|\,10\rangle\,,\,(\sqrt{1-\alpha}\,|\,0\rangle - \sqrt{\alpha}\,|\,1\rangle)(|\,0\rangle + |\,1]\rangle)/\sqrt{2}\}$ and these are all product states. The last states to consider are those of rank two, which fall into two categories [247]. The range is either spanned by product states $\{|\,00\rangle\,,\,(\sqrt{\lambda}\,|\,0\rangle - \sqrt{1-\lambda}\,|\,1\rangle)(\sqrt{\mu}\,|\,0\rangle + \sqrt{1-\mu}\,|\,1\rangle)\}$ or $\{|\,00\rangle\,,\,(\sqrt{\alpha}\,|\,01\rangle + \sqrt{\beta}\,|\,10\rangle) + \sqrt{1-\beta-\alpha}\,|\,00\rangle)\}$. Hence, only states that have a range containing one product state are the mixed states satisfying the condition. All mixed rank two states of two qubits can be considered to be the mixed state formed by tracing out a third qubit from a pure three-qubit system. The classifications of these three-qubit systems is given in [248, 249, 250] and for the range of the mixed system to contain one product state the three-qubit state belongs to the W class.

This class can always be written as $\sqrt{\lambda}\,|\,\Phi\rangle\,|\,1\rangle + \sqrt{1-\lambda}\,|\,00\rangle\,|\,0\rangle$ with

$$|\,\Phi\rangle = \sqrt{\alpha}\,|\,01\rangle + \sqrt{\beta}\,|\,10\rangle + \sqrt{\gamma}\,|\,00\rangle\,,\ \alpha+\beta+\gamma = 1. \tag{A.9}$$

By tracing out one qubit and using local operations the two-qubit state that can not be spanned by product states has the form

$$\rho = \lambda\,|\,\psi\rangle\,\langle\psi\,| + (1-\lambda)\,|\,01\rangle\,\langle 01\,|), \tag{A.10}$$

where

$$|\,\psi\rangle = \sqrt{\alpha}\,|\,00\rangle + \sqrt{\beta}\,|\,11\rangle + \sqrt{\gamma}\,|\,01\rangle\,,\ \alpha+\beta+\gamma = 1. \tag{A.11}$$

So the only states that can be purified into a perfect singlet, given finite copies, are of this form.

If there are two states of this form we know that the system is distillable since the procedure given in Sec. 4.2 succeeds in the distillation.

Appendix B

Extensions for PMSs that have $\gamma \neq 0$

For the recycling distillation scheme introduced in chapter 5 if the initial states are allowed to be general PMSs, $\rho(\alpha, \gamma, \lambda)$, the quantities used in Eq. 5.10, to obtain the probability of successfully obtaining a singlet, change to

$$f_k = 2\lambda_k \left[1 - \gamma_k - \lambda_k(1+\gamma^2)\right], \tag{B.1}$$

$$c_k = 1 - 2\lambda_k + 2\gamma_k\lambda_k + \left[(1-\alpha_k-\gamma_k)^2 + \alpha_k^2 + (1-\gamma_k)^2\right]\lambda_k^2, \tag{B.2}$$

$$\alpha_k = \frac{\alpha_{k-1}^2}{\alpha_{k-1}^2 + (1-\alpha_{k-1}-\gamma_{k-1})^2 + \gamma_{k-1}^2}, \tag{B.3}$$

$$\gamma_k = \frac{\gamma_{k-1}^2}{\alpha_{k-1}^2 + (1-\alpha_{k-1}-\gamma_{k-1})^2 + \gamma_{k-1}^2}, \tag{B.4}$$

$$\lambda_k = \frac{\lambda_{k-1}^2(\alpha_{k-1}^2 + (1-\alpha_{k-1}-\gamma_{k-1})^2 + \gamma_{k-1}^2}{c_{k-1}}. \tag{B.5}$$

Similarly, in chapter 7 if the initial states used in the swapping procedures are allowed to be general PMSs, $\rho(\alpha, \gamma, \lambda)$ and $\rho(\beta, \delta, \nu)$, the formulas for Eq. 7.2, Eq. 7.4, Eq. 7.5 and Eq. 7.9 become

$$p_{CEP} = \left\{2\lambda\nu \min[\alpha(1-\beta-\delta), \beta(1-\alpha-\gamma)]\right\}^2, \tag{B.6}$$

$$p_{d^*} = 2\lambda^2\nu^2 \min(\alpha^2(1-\beta-\delta)^2, \beta^2(1-\alpha-\gamma)^2), \tag{B.7}$$

$$p_d = 2\lambda^2\nu^2\alpha\beta(1-\alpha-\gamma)(1-\beta-\delta), \tag{B.8}$$

and

$$\begin{aligned} p_h =& 2\lambda^2\nu^2[\alpha(1-\beta-\delta)+\beta(1-\alpha-\gamma)] \\ & \times \min[\alpha(1-\beta-\delta), \beta(1-\alpha-\gamma)]. \end{aligned} \tag{B.9}$$

Appendix C

The Distillable Subspace Scheme

To extend the DSS scheme to n PMSs, $\rho(\alpha, \lambda)$, we first need to describe the 2^n nonzero eigenvalues and their eigenvectors. These correspond to different combinations of $n-l$ $|\,\alpha\rangle$ terms and l $|\,01\rangle$ terms. Then taking the decimal representation of the local states we can label each of these eigenvectors by the decimal difference between the values at each location. This difference y in binary gives the location of the $|\,01\rangle$ terms. For example, in the case of two identical PMSs these are

$$\begin{aligned} y = 0 = 00: &\quad |\,\alpha\rangle\,|\,\alpha\rangle\,, \\ y = 2 = 10: &\quad |\,01\rangle\,|\,\alpha\rangle\,, \\ y = 1 = 01: &\quad |\,\alpha\rangle\,|\,01\rangle\,, \\ y = 3 = 11: &\quad |\,01\rangle\,|\,01\rangle \end{aligned} \tag{C.1}$$

and y takes all of the values from 0 to $2^n - 1$. Now we define $m(x)$ to be the number of 1s in the binary representation of x and $T_y = \{x : x \wedge y = 0,\, 0 \leq x < 2^n,\, x \in \mathbb{N}\}$ ('$\wedge$' is the bitwise AND operation).

Then $l = m(y)$ and all of the terms in a nonzero eigenvector are of the form

$$\sum_{x \in T_y} \sqrt{\alpha^{n-m(x)-l}(1-\alpha)^{m(x)}}\, |\, x\rangle_A^d\, |\, x+y\rangle_B^d\,, \tag{C.2}$$

with eigenvalue $\lambda^{n-l}(1-\lambda)^l$.

From this structure we can project out an entangled state if we measure the operator $(|\, c\rangle_A^d \langle c\,|_A^d + |\, d\rangle_A^d \langle d\,|_A^d)$ at A and then $(|\, c+y\rangle_B^d \langle c+y\,|_B^d + |\, d+y\rangle_B^d \langle d+y\,|_B^d)$ at B, when $c \in T_y$, $d \in T_y$, $d > c$ and as long as there are no other terms of the form $|\, c\rangle_A^d\, |\, d+y\rangle_B^d + |\, d\rangle_A^d\, |\, c+y\rangle_B^d$, $|\, c\rangle_A^d\, |\, d+y\rangle_B^d$ or $|\, d\rangle_A^d\, |\, c+y\rangle_B^d$ in any nonzero eigenstate.

The term $|\, c\rangle_A^d\, |\, d+y\rangle_B^d + |\, d\rangle_A^d\, |\, c+y\rangle_B^d$ can not appear in one eigenstate since all of the terms must have the same y value and this would require c to be equal to d. The state $|\, c\rangle_A^d\, |\, d+y\rangle_B^d$ lies in one if and only if $\exists w \in \mathbb{N}$, $0 \leq w \leq 2^n - 1$ such that $c + w = d + y$ and $c \in T_w$; similarly, for $|\, d\rangle_A^d\, |\, c+y\rangle_B^d$ but this case can not occur since $c \in T_y$ and $d \in T_y$ means that $w \geq y$ and $d + w > c + y$. If we assume that $\exists w \in \mathbb{N}$, $0 \leq w \leq 2^n - 1$ such that $c + w = d + y$ and $c \in T_w$ this would mean that $d = c + k$ and that $c \wedge k = 0$ for some $k > 0$. Both of these results then give that $k \wedge y = 0$ and $w = k + y$. So, if $w = y + k = d + y - c$ such that $c \wedge k = 0$ can not be satisfied we create a maximally entangled state.

Now we have a choice of ways of creating these measurements. One particular way involves the definition of sets $S_k = \{x : m(x) = k,\, 0 \leq x < 2^n,\, x \in \mathbb{N}\}$ and $J_{a,b} = \{x\colon\ x \wedge (a \text{ OR } b) = 0,\, 0 \leq x < 2^n, x \in \mathbb{N}\}$. Then the protocol consists of performing a POVM $P_{k,a,b} = C_k(|\, a\rangle_A^d \langle a\,|_A^d + |\, b\rangle_A^d \langle b\,|_A^d)$ at location A with $a,\, b \in S_k$, $a \neq b$, and $0 < k < n$. For $k = 0$ and n we define $P_{k,a,b} = \left|\, 2^k - 1\right\rangle_A^d \left\langle 2^k - 1\,\right|_A^d$ and when these outcomes occur the procedure has failed. Here C_k is a factor to ensure

that

$$\sum_{a,b\in S_k,k=0}^{k=n} P_{k,a,b} = I. \tag{C.3}$$

With this outcome at location A another POVM is done at location B given by the operators $Q_d = C_k(|\, a+d\rangle_B^d \langle a+d\,|_B^d + |\, b+d\rangle_B^d \langle b+d\,|_B^d)$ $(d \in J_{a,b})$ and $F = I - \sum_{d\in J_{a,b}} Q_d$. If the outcome here is F the protocol has failed; otherwise we have obtained a maximally entangled state. This protocol works since a, $b \in T_y$ for all $y \in J_{a,b}$ but there is no $w = k + y$ such that $k \wedge a = 0$ and $b + y = a + y + k$, since if there were we would have $b = a + k$ but $m(a + k) \neq m(b)$.

The probability of succeeding is given by Eq. (5.5) which comes from considering a particular eigenstate with parameter y. In this eigenstate there are

$$N_1 = \binom{n-m(y)}{k}\left(\binom{n-m(y)}{k} - 1\right)/2 \tag{C.4}$$

different pairing terms, $|\, a\rangle_A^d\, |\, a+y\rangle_B^d + |\, b\rangle_A^d\, |\, b+y\rangle_B^d$ with $a, b \in S_k$. The number of possible measured operators from this eigenstate is given by

$$N_2 = \binom{n-m(y)}{k}\left(\binom{n}{k} - 1\right). \tag{C.5}$$

Note that the pairings in the eigenstate are twice as likely to occur than the ones with just an overlap and these have been counted twice in this sum. The probability that starting with an eigenstate (parameter y) we succeed is then

$$\frac{2N_1}{N_2} = \frac{\binom{n-m(y)}{k} - 1}{\binom{n}{k} - 1}, \tag{C.6}$$

given that we have measured the operator S_k and the probability of this was

$$P_k = \binom{n-m(y)}{k}\alpha^{n-m(y)-k}(1-\alpha)^k. \tag{C.7}$$

By summing over these we have, given we start with an eigenstate with $m(y) = m$, the probability of succeeding to be

$$\sum_{k=1}^{n-m-1} \frac{\alpha^{n-m-k}(1-\alpha)^k \binom{n-m}{k}\left(\binom{n-m}{k}-1\right)}{\binom{n}{k}-1} \tag{C.8}$$

and these eigenstates occur with probability,

$$\lambda^{n-m}(1-\lambda)^m \binom{n}{m}. \tag{C.9}$$

We have not counted $k = 0, n-m$ since they never contribute to the success probability. Then by summing over all of these we get the result in Eq. (5.5).

Appendix D

Classical Nanofiber Field Modes

For light of wavelength, λ, and $k = 2\pi/\lambda$, the field parameters must satisfy the fiber eigenvalue equation [219]

$$\begin{aligned}\frac{J_0(hR)}{hRJ_1(hR)} = &-\frac{n_1^2+n_2^2}{2n_1^2}\frac{K_1'(qR)}{qRK_1(qR)} + \frac{1}{h^2R^2} \\ &- \left[\left(\frac{n_1^2-n_2^2}{2n_1^2}\frac{K_1'(qR)}{qRK_1(qR)}\right)^2 \right. \\ &\left. + \frac{\beta^2}{n_1^2k^2}\left(\frac{1}{q^2R^2}+\frac{1}{h^2R^2}\right)^2\right]^{1/2}, \end{aligned} \tag{D.1}$$

with J_ν referring to the Bessel function of the first kind and K_ν being the modified Bessel function of the second kind. By numerically solving Eq. (D.1) the value of the propagation constant β is determined. We also define the parameters $h = (n_1^2k^2 - \beta^2)^{1/2}$, $q = (\beta^2 - n_2^2k^2)^{1/2}$, and

$$g = \left(\frac{1}{q^2R^2}+\frac{1}{h^2R^2}\right) / \left(\frac{J_1'(hR)}{hRJ_1(hR)} + \frac{K_1'(qR)}{qRK_1(qR)}\right). \tag{D.2}$$

Inside the fiber ($0 < r < R$) the guided mode, $m = (f, p)$, has the form

$$e_r^m = \mathrm{i}\frac{qK_1(R)}{hJ_1(hR)}[(1-g)J_0(hr) - (1+g)J_2(hr)], \tag{D.3}$$

$$e_\varphi^m = -p\frac{qK_1(qR)}{hJ_1(hR)}[(1-g)J_0(hr) + (1+g)J_2(hr)], \tag{D.4}$$

$$e_z^m = f\frac{2qK_1(qR)}{\beta J_1(hR)}J_1(hr), \tag{D.5}$$

and outside $r > R$

$$e_r^m = \mathrm{i}[(1-g)K_0(qr) + (1+g)K_2(qr)], \tag{D.6}$$

$$e_\varphi^m = -p[(1-g)K_0(qr) - (1+g)K_2(qr)], \tag{D.7}$$

$$e_z^m = f\frac{2q}{\beta}K_1(qr), \tag{D.8}$$

These are normalized with a factor given by

$$\int_0^{2\pi}\int_0^R n_1^2 \left|\mathbf{e}\right|^2 r\mathrm{d}r\mathrm{d}\varphi + \int_0^{2\pi}\int_R^\infty n_2^2 \left|\mathbf{e}\right|^2 r\mathrm{d}r\mathrm{d}\varphi = A. \tag{D.9}$$

Appendix E

The Carbon Nanotube's Optical Matrix Element

The matrix element for the interaction between can be found by substituting in the wavefunctions to give

$$\begin{aligned} G &= \langle \Psi^c(\mathbf{k}') \,|\, \mathbf{A}^+.\nabla \,|\, \Psi^v(\mathbf{k}) \rangle \\ &= \sum_{s,t=A,B} c_s^{c*}(\mathbf{k}') c_t^v(\mathbf{k}) \left\langle \tilde{p}_z^s(\mathbf{k}') \,|\, \mathbf{A}^+.\nabla \,\middle|\, \tilde{p}_z^t(\mathbf{k}) \right\rangle \\ &= \frac{1}{N_{cells}} \sum_{s,t=A,B} c_s^{c*}(\mathbf{k}') c_t^v(\mathbf{k}) \\ &\quad \sum_{\mathbf{r}_1 \in \mathbf{R}_s, \mathbf{r}_2 \in \mathbf{R}_t} \mathrm{e}^{\mathrm{i}\mathbf{k}.\mathbf{r}_2 - \mathrm{i}\mathbf{k}'.\mathbf{r}_1} \left\langle p_z(\mathbf{r} - \mathbf{r}_1) \,|\, \mathbf{A}^+.\nabla \,|\, p_z(\mathbf{r} - \mathbf{r}_2) \right\rangle . \end{aligned} \tag{E.1}$$

This can then be further simplified to give

$$
\begin{aligned}
G = & \frac{1}{N_G N_L} \sum_{\mathbf{r}_1 \in \mathbf{R}_A, \mathbf{r}_2 \in \mathbf{R}_B} \\
& c_A^{c*}(\mathbf{k}') c_B^v(\mathbf{k}) \mathrm{e}^{\mathrm{i}\mathbf{k}.\mathbf{r}_2 - \mathrm{i}\mathbf{k}'.\mathbf{r}_1} \\
& \qquad \langle p_z(\mathbf{r} - \mathbf{r}_1) \,|\, \mathbf{A}^+ . \nabla \,|\, p_z(\mathbf{r} - \mathbf{r}_2) \rangle \\
& + c_B^{c*}(\mathbf{k}') c_A^v(\mathbf{k}) \mathrm{e}^{\mathrm{i}\mathbf{k}.\mathbf{r}_1 - \mathrm{i}\mathbf{k}'.\mathbf{r}_2} \\
& \qquad \langle p_z(\mathbf{r} - \mathbf{r}_2) \,|\, \mathbf{A}^+ . \nabla \,|\, p_z(\mathbf{r} - \mathbf{r}_1) \rangle \\
= & \frac{M\sqrt{3}}{a N_G N_L} \Bigg[c_A^{c*}(\mathbf{k}') c_B^v(\mathbf{k}) \\
& \qquad \sum_{\mathbf{r}_1 \in \mathbf{R}_A} \mathrm{e}^{-\mathrm{i}(\mathbf{k}' - \mathbf{k}).\mathbf{r}_1} \mathbf{A}^+(\mathbf{r}_1) . \mathbf{v}^A(\mathbf{k}) \\
& + c_B^{c*}(\mathbf{k}') c_A^v(\mathbf{k}) \\
& \qquad \sum_{\mathbf{r}_2 \in R_B} \mathrm{e}^{-\mathrm{i}(\mathbf{k}' - \mathbf{k}).\mathbf{r}_2} \mathbf{A}^+(\mathbf{r}_2) . \mathbf{v}^B(\mathbf{k}) \Bigg] .
\end{aligned}
\tag{E.2}
$$

Here we have assumed that the orbitals are symmetric and that $\mathbf{A}^+$ is constant across each of the nanotube's unit cells. This ignores any effect that the curvature has on the bond form. This approximation is reasonable for nanotubes that have a diameter greater than 1nm [188]. The expression for G can then be split into

separate unit cells and directions:

$$G = G_x + G_y + G_z \tag{E.3}$$

$$\begin{aligned}
G_z = \frac{M\sqrt{3}}{2anN_L} \Bigg[& \sum_{l=1}^{N_L} \mathrm{e}^{\mathrm{i}\left\{al\sqrt{3}-(L/2)\right\}(k_{||}-k'_{||})} \\
& A_z^+(la\sqrt{3}-(L/2)) \Bigg] \\
& \sum_{j=1}^{n} \Bigg[c_A^{c*}(\mathbf{k}') c_B^v(\mathbf{k}) \mathrm{e}^{-\mathrm{i}ja(k'_\perp - k_\perp)} \\
& \left\{ 1 + \mathrm{e}^{-\mathrm{i}a(\mathbf{k}'-\mathbf{k}).(\sqrt{3}/2,1/2)} \right\} v_z^A(\mathbf{k}) \\
& - c_B^{c*}(\mathbf{k}') c_A^v(\mathbf{k}) \mathrm{e}^{-\mathrm{i}ja(k'_\perp - k_\perp)} \mathrm{e}^{\mathrm{i}a(k_{||}-k'_{||})/\sqrt{3}} \\
& \left\{ 1 + \mathrm{e}^{-\mathrm{i}a(\mathbf{k}'-\mathbf{k}).(\sqrt{3}/2,1/2)} \right\} v_z^A(\mathbf{k})^* \Bigg] \\
= \frac{1}{N_L} D_z \Bigg[& \sum_{l=1}^{N_L} \mathrm{e}^{\mathrm{i}(k_{||}-k'_{||})\left\{la\sqrt{3}-(L/2)\right\}} \\
& A_z^+(la\sqrt{3}-(L/2)) \Bigg].
\end{aligned} \tag{E.4}$$

In order to calculate G_x and G_y we must calculate the contribution of each rotated bond around the nanotube and sum these up. To do this we use the method

from Ref. [179] and introduce the parameters

$$v_{\pm}^{A_0} = \mathrm{e}^{\mathrm{i}a\mathbf{k}.(-1/(2\sqrt{3}),-1/2)}(\mathrm{e}^{\mp 2\pi\mathrm{i}/2n} - 1) + \mathrm{e}^{\mathrm{i}a\mathbf{k}.-1/(2\sqrt{3},1/2)}(\mathrm{e}^{\pm 2\pi\mathrm{i}/2n} - 1) \tag{E.5}$$

$$v_{\pm}^{B_0} = \mathrm{e}^{\mathrm{i}a\mathbf{k}.(1/(2\sqrt{3}),-1/2)}(\mathrm{e}^{\mp 2\pi\mathrm{i}/2n} - 1) + \mathrm{e}^{\mathrm{i}a\mathbf{k}.(1/(2\sqrt{3}),1/2)}(\mathrm{e}^{\pm 2\pi\mathrm{i}/2n} - 1) \tag{E.6}$$

$$v_{x(\theta)}^{A}(\mathbf{k}) = R_t \frac{\mathrm{e}^{\mathrm{i}\theta} v_{+}^{A_0} + \mathrm{e}^{-\mathrm{i}\theta} v_{-}^{A_0}}{2} \tag{E.7}$$

$$v_{x(\theta)}^{B}(\mathbf{k}) = R_t \frac{\mathrm{e}^{\mathrm{i}\theta} v_{+}^{B_0} + \mathrm{e}^{-\mathrm{i}\theta} v_{-}^{B_0}}{2} \tag{E.8}$$

$$v_{y(\theta)}^{A}(\mathbf{k}) = R_t \frac{\mathrm{e}^{\mathrm{i}\theta} v_{+}^{A_0} + \mathrm{e}^{-\mathrm{i}\theta} v_{-}^{A_0}}{2\mathrm{i}} \tag{E.9}$$

$$v_{y(\theta)}^{B}(\mathbf{k}) = R_t \frac{\mathrm{e}^{\mathrm{i}\theta} v_{+}^{B_0} + \mathrm{e}^{-\mathrm{i}\theta} v_{-}^{B_0}}{2\mathrm{i}}. \tag{E.10}$$

These use rotations in the complex plain to calculate the contributions in the plain perpendicular to the nanotube. From these we calculate $G_{d=x,y}$ to be

$$
\begin{aligned}
G_d = \frac{M\sqrt{3}}{2anN_L}\Bigg[& \sum_{l=1}^{N_L} \mathrm{e}^{\mathrm{i}(k_{||}-k'_{||})(la\sqrt{3}-(L/2))} \\
& A_d^+(la\sqrt{3}-(L/2))\Bigg] \\
& \sum_{j=1}^{n} c_A^{c*}(\mathbf{k}')c_B^v(\mathbf{k})\Bigg[v^A_{d(2\pi j/n)}(\mathbf{k})\mathrm{e}^{-\mathrm{i}ja(k'_\perp-k_\perp)}+ \\
& + v^A_{d(2\pi(j+1/2)/n)}(\mathbf{k})\mathrm{e}^{-\mathrm{i}ja(k'_\perp-k_\perp)}\mathrm{e}^{-\mathrm{i}a\mathbf{k}'.(1/(2\sqrt{3}),1/2)}\Bigg] \\
& - c_B^{c*}(\mathbf{k}')c_A^v(\mathbf{k})\Bigg[v^B_{d(2\pi j/n)}(\mathbf{k})\mathrm{e}^{-\mathrm{i}ja(k'_\perp-k_\perp)}\mathrm{e}^{-\mathrm{i}ak'_{||}/\sqrt{3}} \\
& + v^B_{d(2\pi(j+1/2)/n)}(\mathbf{k})\mathrm{e}^{-\mathrm{i}ja(k'_\perp-k_\perp)}\mathrm{e}^{-\mathrm{i}a\mathbf{k}'.(5/(2\sqrt{3}),1/2)}\Bigg] \\
= \frac{1}{N_L}\mathbf{D}_d\Bigg[& \sum_{l=1}^{N_L} \mathrm{e}^{\mathrm{i}(k_{||}-k'_{||})(la\sqrt{3}-(L/2))} \\
& A_d^+(la\sqrt{3}-(L/2))\Bigg]. \qquad \text{(E.11)}
\end{aligned}
$$

Hence, we obtain

$$
G = \frac{1}{N_L}\mathbf{D}\sum_{l=1}^{N_L} \mathrm{e}^{\mathrm{i}(k_{||}-k'_{||})(la\sqrt{3}-(L/2))}\mathbf{A}^+(la\sqrt{3}-(L/2)). \qquad \text{(E.12)}
$$

Acknowledgements

There are many people and organizations that I must thank and without which this thesis would not exist. Foremost of these is my supervisor, Prof. Dieter Jaksch, whose continuous guidance and advice have been a source of constant support throughout my doctoral research. His insight and breadth of knowledge has always been inspiring. As a DPhil student I can not overstate the importance of these qualities and will always be indebted. I heartily thank all of my colleagues and especially, Dr. Uwe Dorner. Working together has been a cheerful and engaging experience that has helped to enhance every aspect of my work. The Oxford Physics department has been an excellent place to study and have provided me with everything I could need and more. St John's College has provided me with a pleasant home in Oxford. My thanks must also be extended to all of those at Oxford and Cambridge who have stimulated and inspired my interest in Quantum information theory and theoretical physics. Particularly Malcolm Perry, Adrian Kent, Alastair Kay and Nilanjana Datta. Personal thanks must of course go to all of my friends. Many of whom have completed doctorates. I can only hope that I gave them at least a fraction of the support that they have shown me. Of course, none of this would be possible without the generous funding provided by EPSRC. Finally, I can only attempt to put into words the thanks I owe to my family. Together my sisters and parents have helped me in every way possible. Their affection and advice has supported me throughout my student life. Hopefully one day I will make it up to them.

Bibliography

[1] A. Einstein, B. Podolsky, and N Rosen. Can quantum mechanical description of phyical reality be considered complete? *Phys. Rev.* **47**(10), 777–780 May (1935).

[2] A. Einstein. *The Born-Einstein Letters; Correspondence between Albert Einstein and Max and Hedwig Born from 1916 to 1955*. Walker, New York, (1971).

[3] J. S. Bell. On the einstein-podolsky-rosen paradox. *Physics* **1**(3) (1964).

[4] S. Popescu and D. Rohrlich. Generic quantum nonlocality. *Physics Letters A* **166**, 293–297 (1992).

[5] S. J. Freedman and J. F. Clauser. Experimental test of local hidden-variable theories. *Phys. Rev. Lett.* **28**, 938 (1972).

[6] E. S. Fry and R. C. Thompson. Experimental test of local hidden-variable theories. *Phys. Rev. Lett.* **37**, 465–468 Aug (1976).

[7] A. Aspect, P. Grangier, and G. Roger. Experimental tests of realistic local theories via bells theorem. *Phys. Rev. Lett.* **47**, 460–463 (1981).

[8] A. Aspect, J. Dalibard, and G. Roger. Experimental test of bell inequalities using time-varying analyzers. *Phys. Rev. Lett.* **49**, 1804–1807 (1982).

[9] D. M. Greenberger, M. A. Horne, and A. Zeilinger. Going beyond bell's theorem. *Bell's Theorem, Quantum Theory, and Conceptions of the Universe, M. Kafatos (Ed.), Kluwer, Dordrecht* , 69–72 (1989).

[10] D. Bouwmeester, J-W. Pan, M. Daniell, H. Weinfurter, and A. Zeilinger. Observation of three-photon greenberger-horne-zeilinger entanglement. *Phys. Rev. Lett.* **82**, 1345–1349 Feb (1999).

[11] C. H. Bennett, G. Brassard, C. Crépeau, R. Jozsa, A. Peres, and W. K. Wootters. Teleporting an unknown quantum state via dual classical and einstein-podolsky-rosen channels. *Phys. Rev. Lett.* **70**(13), 1895–1899 Mar (1993).

[12] J. I. Cirac, A. K. Ekert, S. F. Huelga, and C. Macchiavello. Distributed quantum computation over noisy channels. *Phys. Rev. A* **59**(6), 4249–4254 Jun (1999).

[13] C. H. Bennett and S. J. Wiesner. Communication via one-particle and 2-particle operators on einstein-podolsky-rosen states. *Phys. Rev. Lett.* **69**, 2881–2884 (1992).

[14] S. Wiesner. Conjugate coding. *SIGACT News* **15**(1), 78–88 Jan (1983).

[15] C. H. Bennett and G. Brassard. Quantum cryptography: Public key distribution and coin tossing. *Proceedings of the IEEE International Conference on Computers, Systems, and Signal Processing, Bangalore* , 175 (1984).

[16] A. K. Ekert. Quantum cryptography based on bell's theorem. *Phys. Rev. Lett.* **67**(6), 661–663 Aug (1991).

[17] M. A. Nielsen and I. L. Chuang. *Quantum Computation and Quantum Information*. Cambridge University Press, Cambridge, (2000).

[18] R. Horodecki, M. Horodecki, and K. Horodecki. Quantum entanglement. *Rev. Mod. Phys.* **81**(2), 865–942 Jun (2009).

[19] S. F. Huelga, C. Macchiavello, T. Pellizzari, A. K. Ekert, M. B. Plenio, and J. I. Cirac. Improvement of frequency standards with quantum entanglement. *Phys. Rev. Lett.* **79**, 3865–3868 (1997).

[20] V. Giovannetti, S. Lloyd, and L. Maccone. Quantum-enhanced measurements: Beating the standard quantum limit. *Science* **306**, 1330–1336 (2004).

[21] H. Buhrman, R. Cleve, and W. Van Dam. Quantum entanglement and communication complexity. *Siam Journal on Computing* **30**, 1829–1841 (2001).

[22] C. Brukner, M. Zukowski, J. W. Pan, and A. Zeilinger. Bell's inequalities and quantum communication complexity. *Phys. Rev. Lett.* **92**, 127901 (2004).

[23] V. M. Kendon and W. J. Munro. Entanglement and its role in shor's algorithm. *Quant. Inf. Comp.* **6**, 630–640 (2006).

[24] R. Raussendorf and H. J. Briegel. A one-way quantum computer. *Phys. Rev. Lett.* **86**(22), 5188–5191 (2001).

[25] R. Raussendorf, D. E. Browne, and H. J. Briegel. Measurement-based quantum computation on cluster states. *Phys. Rev. A* **68**, 022312 (2003).

[26] R. Raussendorf and J. Harrington. Fault-tolerant quantum computation with high threshold in two dimensions. *Phys. Rev. Lett.* **98**, 190504 (2007).

[27] T. M. Stace, S. D. Barrett, and A. C. Doherty. Thresholds for topological codes in the presence of loss. *Phys. Rev. Lett.* **102**(20) (2009).

[28] T. M. Stace and S. D. Barrett. Error correction and degeneracy in surface codes suffering loss. *Phys. Rev. A* **81**, 022317 (2010).

[29] A. Kay. Basics of perfect communication through quantum networks. *Phys. Rev. A* **84**, 022337 (2011).

[30] J. I. Cirac, P. Zoller, H. J. Kimble, and H. Mabuchi. Quantum state transfer and entanglement distribution among distant nodes in a quantum network. *Phys. Rev. Lett.* **78**, 3221–3224 (1997).

[31] H. J. Kimble. The quantum internet. *Nature* **453**, 1023–1030 Jun 19 (2008).

[32] T. Schmitt-Manderbach, H. Weier, M. Fürst, R. Ursin, F. Tiefenbacher, T. Scheidl, J. Perdigues, Z. Sodnik, C. Kurtsiefer, J. G. Rarity, A. Zeilinger,

and H. Weinfurter. Experimental demonstration of free-space decoy-state quantum key distribution over 144 km. *Phys. Rev. Lett.* **98**, 010504 Jan (2007).

[33] A. Poppe, M. Peev, and O. Maurhart. Outline of the secoqc quantum-key-distribution network in vienna. *International Journal of Quantum Information* **06**(02), 209–218 (2008).

[34] M. Sasaki, M. Fujiwara, H. Ishizuka, W. Klaus, K. Wakui, M. Takeoka, S. Miki, T. Yamashita, Z. Wang, A. Tanaka, K. Yoshino, Y. Nambu, S. Takahashi, A. Tajima, A. Tomita, T. Domeki, T. Hasegawa, Y. Sakai, H. Kobayashi, T. Asai, K. Shimizu, T. Tokura, T. Tsurumaru, M. Matsui, T. Honjo, K. Tamaki, H. Takesue, Y. Tokura, J. F. Dynes, A. R. Dixon, A. W. Sharpe, Z. L. Yuan, A. J. Shields, S. Uchikoga, M. Legré, S. Robyr, P. Trinkler, L. Monat, J.-B. Page, G. Ribordy, A. Poppe, A. Allacher, O. Maurhart, T. Länger, M. Peev, and A. Zeilinger. Field test of quantum key distribution in the tokyo qkd network. *Opt. Express* **19**(11), 10387–10409 May (2011).

[35] C. Bonato, A. Tomaello, V. Da Deppo, G. Naletto, and P. Villoresi. Feasibility of satellite quantum key distribution. *New Journal of Physics* **11**, 045017 (2009).

[36] C. Z. Peng, T. Yang, X. H. Bao, J. Zhang, X. M. Jin, F. Y. Feng, B. Yang, J. Yang, J. Yin, Q. Zhang, N. Li, B. L. Tian, and J. W. Pan. Experimental free-space distribution of entangled photon pairs over 13 km: Towards satellite-based global quantum communication. *Phys. Rev. Lett.* **94**, 150501 (2005).

[37] P. Villoresi, T. Jennewein, F. Tamburini, M. Aspelmeyer, C. Bonato, R. Ursin, C. Pernechele, V. Luceri, G. Bianco, A. Zeilinger, and C. Barbieri. Experimental verification of the feasibility of a quantum channel between space and earth. *New Journal of Physics* **10**(3), 033038 (2008).

[38] A. Steane. Multiple-particle interference and quantum error correction. *Proceedings of the Royal Society of London Series a-Mathematical Physical and Engineering Sciences* **452**, 2551–2577 (1996).

[39] A. M. Steane. Error correcting codes in quantum theory. *Phys. Rev. Lett.* **77**, 793–797 (1996).

[40] A. M. Steane. Simple quantum error-correcting codes. *Phys. Rev. A* **54**, 4741–4751 (1996).

[41] A. M. Steane. Introduction to quantum error correction. *Philosophical Transactions of the Royal Society a-Mathematical Physical and Engineering Sciences* **356**, 1739–1757 (1998).

[42] C. H. Bennett, G. Brassard, S. Popescu, B. Schumacher, J. A. Smolin, and W. K. Wootters. Purification of noisy entanglement and faithful teleportation via noisy channels. *Phys. Rev. Lett.* **76**, 722 (1996).

[43] D. Deutsch, A. Ekert, R. Jozsa, C. Macchiavello, S. Popescu, and A. Sanpera. Quantum privacy amplification and the security of quantum cryptography over noisy channels. *Phys. Rev. Lett.* **77**, 2818 (1996).

[44] B. Yurke and D. Stoler. Bells-inequality experiments using independent-particle sources. *Phys. Rev. A* **46**, 2229–2234 (1992).

[45] M. Zukowski, A. Zeilinger, M. A. Horne, and A. K. Ekert. Event-ready-detectors bell experiment via entanglement swapping. *Phys. Rev. Lett.* **71**, 4287–4290 (1993).

[46] S. Bose, V. Vedral, and P. L. Knight. Purification via entanglement swapping and conserved entanglement. *Phys. Rev. A* **60**(1), 194 (1999).

[47] H.-J. Briegel, W. Dür, J. I. Cirac, and P. Zoller. Quantum repeaters: The role of imperfect local operations in quantum communication. *Phys. Rev. Lett.* **81**, 5932 (1998).

[48] W. Dür, H.-J. Briegel, J. I. Cirac, and P. Zoller. Quantum repeaters based on entanglement purification. *Phys. Rev. A* **59**, 169 (1999).

[49] L.-M. Duan, M. D. Lukin, J. I. Cirac, and P. Zoller. Long-distance quantum communication with atomic ensembles and linear optics. *Nature* **414**, 413 (2001).

[50] L. Childress, J. M. Taylor, A. S. Sorensen, and M. D. Lukin. Fault-tolerant quantum repeaters with minimal physical resources and implementations based on single-photon emitters. *Phys. Rev. A* **72**, 052330 (2005).

[51] L. Hartmann, B. Kraus, H.-J. Briegel, and W. Dür. Role of memory errors in quantum repeaters. *Phys. Rev. A* **75**, 032310 (2007).

[52] U. Dorner, A. Klein, and D. Jaksch. A quantum repeater based on decoherence free subspaces. *Quant. Inf. Comp.* **8**, 0468 (2008).

[53] L. Jiang, J. M. Taylor, K. Nemoto, W. J. Munro, R. Van Meter, and M. D. Lukin. Quantum repeater with encoding. *Phys. Rev. A* **79**(3), 032325 Mar (2009).

[54] N. Dutil and P. Hayden. Assisted entanglement distillation. *Quant. Inf. Comp.* **11**, 496–520 (2011).

[55] M. Popp, F. Verstraete, M. A. Martin-Delgado, and J. I. Cirac. Localizable entanglement. *Phys. Rev. A* **71**, 042306 Apr (2005).

[56] F. Verstraete, M. Popp, and J. I. Cirac. Entanglement versus correlations in spin systems. *Phys. Rev. Lett.* **92**, 027901 Jan (2004).

[57] A. Acín, J. I. Cirac, and M. Lewenstein. Entanglement percolation in quantum networks. *Nature Physics* **3**, 256 (2007).

[58] S. Perseguers, J. I. Cirac, A. Acín, M. Lewenstein, and J. Wehr. Entanglement distribution in pure-state quantum networks. *Phys. Rev. A* **77**, 022308 (2008).

[59] G. J. Lapeyre Jr., J. Wehr, and M. Lewenstein. Enhancement of entanglement percolation in quantum networks via lattice transformations. *Phys. Rev. A* **79**, 042324 (2009).

[60] M. Cuquet and J. Calsamiglia. Entanglement percolation in quantum complex networks. *Phys. Rev. Lett.* **103**(24), 240503 Dec (2009).

[61] S. Perseguers, D. Cavalcanti, G. J. Lapeyre, M. Lewenstein, and A. Acín. Multipartite entanglement percolation. *Phys. Rev. A* **81**(3), 032327 Mar (2010).

[62] K. Kieling and J. Eisert. *Quantum and Semi-classical Percolation and Breakdown in Disordered Solids*, volume 762 of *Lecture Notes in Physics*, chapter Percolation in quantum computation and communication, 287–319. Springer, Berlin (2009). Also available at arXiv [quant-ph] 0712.1836.

[63] S. D. Barrett, S. D. Bartlett, A. C. Doherty, D. Jennings, and T. Rudolph. Transitions in the computational power of thermal states for measurement-based quantum computation. *Phys. Rev. A* **80**, 062328 Dec (2009).

[64] S. Perseguers, L. Jiang, N. Schuch, F. Verstraete, M. D. Lukin, J. I. Cirac, and K. G. H. Vollbrecht. One-shot entanglement generation over long distances in noisy quantum networks. *Phys. Rev. A* **78**(6), 062324 (2008).

[65] S. Broadfoot, U. Dorner, and D. Jaksch. Entanglement percolation with bipartite mixed states. *EPL (Europhysics Letters)* **88**(5), 50002 (2009).

[66] S. Broadfoot, U. Dorner, and D. Jaksch. Singlet generation in mixed-state quantum networks. *Phys. Rev. A* **81**(4), 042316 Apr (2010).

[67] S. Broadfoot, U. Dorner, and D. Jaksch. Long-distance entanglement generation in two-dimensional networks. *Phys. Rev. A* **82**, 042326 Oct (2010).

[68] S. Broadfoot, U. Dorner, and D. Jaksch. Optical excitation of zigzag carbon nanotubes with photons guided in nanofibers. *Phys. Rev. B* **85**, 195455 May (2012).

[69] H. Ollivier and W. H. Zurek. Quantum discord: A measure of the quantumness of correlations. *Phys. Rev. Lett.* **88**, 017901 Dec (2001).

[70] B. Dakić, V. Vedral, and C. Brukner. Necessary and sufficient condition for nonzero quantum discord. *Phys. Rev. Lett.* **105**, 190502 Nov (2010).

[71] C. H. Bennett, D. P. DiVincenzo, C. A. Fuchs, T. Mor, E. Rains, P. W. Shor, J. A. Smolin, and W. K. Wootters. Quantum nonlocality without entanglement. *Phys. Rev. A* **59**, 1070–1091 Feb (1999).

[72] V. Vedral and M. B. Plenio. Entanglement measures and purification procedures. *Phys. Rev. A* **57**, 1619–1633 Mar (1998).

[73] L. Masanes, Y.-C. Liang, and A. C. Doherty. All bipartite entangled states display some hidden nonlocality. *Phys. Rev. Lett.* **100**, 090403 Mar (2008).

[74] H. Barnum and N. Linden. Monotones and invariants for multi-particle quantum states. *Journal of Physics a-Mathematical and General* **34**, 6787–6805 (2001).

[75] J. Eisert and H. J. Briegel. Schmidt measure as a tool for quantifying multiparticle entanglement. *Phys. Rev. A* **64**, 022306 (2001).

[76] V. Coffman, J. Kundu, and W. K. Wootters. Distributed entanglement. *Phys. Rev. A* **61**, 052306 (2000).

[77] A. Miyake. Classification of multipartite entangled states by multidimensional determinants. *Phys. Rev. A* **67**, 012108 (2003).

[78] F. Verstraete, J. Dehaene, and B. De Moor. Normal forms and entanglement measures for multipartite quantum states. *Phys. Rev. A* **68**, 012103 (2003).

[79] K. G. H. Vollbrecht and R. F. Werner. Entanglement measures under symmetry. *Phys. Rev. A* **64**(6), 062307 Nov (2001).

[80] R. F. Werner. Quantum states with einstein-podolsky-rosen correlations admitting a hidden-variable model. *Phys. Rev. A* **40**(8), 4277–4281 Oct (1989).

[81] W. K. Wootters. Entanglement of formation of an arbitrary state of two qubits. *Phys. Rev. Lett.* **80**, 2245–2248 (1998).

[82] A. M. Steane. Error correcting codes in quantum theory. *Phys. Rev. Lett.* **77**(5), 793–797 (1996).

[83] A. M. Steane. Efficient fault-tolerant quantum computing. *Nature* **399**(6732), 124–126 (1999).

[84] P. W. Shor. Scheme for reducing decoherence in quantum computer memory. *Phys. Rev. A* **52**, R2493–R2496 Oct (1995).

[85] A. R. Calderbank and P. W. Shor. Good quantum error-correcting codes exist. *Phys. Rev. A* **54**, 1098–1105 Aug (1996).

[86] A. Y. Kitaev. Quantum error correction with imperfect gates. *Quantum Communication, Computing, and Measurement* , 181–188 (1997). Hirota, O Holevo, AS Caves, CM 3rd International Conference on Quantum Communication and Measurement Sep 25-30, 1996 Shizuoka, Japan.

[87] A. Y. Kitaev. Fault-tolerant quantum computation by anyons. *Annals of Physics* **303**(1), 2–30 (2003).

[88] E. Dennis, A. Kitaev, A. Landahl, and J. Preskill. Topological quantum memory. *Journal of Mathematical Physics* **43**(9), 4452–4505 (2002).

[89] W. Dur and H. J. Briegel. Entanglement purification and quantum error correction. *Reports on Progress in Physics* **70**(8), 1381 (2007).

[90] C. H. Bennett, D. P. DiVincenzo, J. A. Smolin, and W. K. Wootters. Mixed-state entanglement and quantum error correction. *Phys. Rev. A* **54**, 3824–3851 (1996).

[91] M. Nielsen and G. Vidal. Majorization and the interconversion of bipartite states. *Quant. Inf. Comp.* **1**, 76 (2001).

[92] G. Vidal. Entanglement of pure states for a single copy. *Phys. Rev. Lett.* **83**, 1046 (1999).

[93] A. Kent. Entangled mixed states and local purification. *Phys. Rev. Lett.* **81**(14), 2839–2841 (1998).

[94] N. Linden, S. Massar, and S. Popescu. Purifying noisy entanglement requires collective measurements. *Phys. Rev. Lett.* **81**(15), 3279–3282 (1998).

[95] W. Dur, H. J. Briegel, J. I. Cirac, and P. Zoller. Quantum repeaters based on entanglement purification. *Phys. Rev. A* **59**(1), 169–181 (1999).

[96] J. Modlawska and A. Grudka. Increasing singlet fraction with entanglement swapping. *Phys. Rev. A* **78**(3) (2008).

[97] G. Gour and B. C. Sanders. Remote preparation and distribution of bipartite entangled states. *Phys. Rev. Lett.* **93** (2004).

[98] S. Lee. Bound on remote preparation of entanglement from isotropic states. *Phys. Rev. A* **85**, 052311 (2012).

[99] M. Newman. *Networks: An Introduction.* Oxford University Press, Oxford, (2010).

[100] B. Bollobás and O. Riordan. *Percolation.* Cambridge University Press, Cambridge, (2006).

[101] S. N. Dorogovtsev, A. V. Goltsev, and J. F. F. Mendes. Critical phenomena in complex networks. *Rev. Mod. Phys.* **80**, 1275–1335 Oct (2008).

[102] R. Cohen and S. Havlin. Scale-free networks are ultrasmall. *Phys. Rev. Lett.* **90**, 058701 Feb (2003).

[103] G. J. Lapeyre, S. Perseguers, M. Lewenstein, and A. Acín. Distribution of entanglement in networks of bi-partite full-rank mixed states. *arXiv:1108.5833 [quant-ph]* (2012).

[104] A. G. Fowler, D. S. Wang, C. D. Hill, T. D. Ladd, R. Van Meter, and L. C. L. Hollenberg. Surface code quantum communication. *Phys. Rev. Lett.* **104**, 180503 May (2010).

[105] K. G. H. Vollbrecht, C. A. Muschik, and J. I. Cirac. Entanglement distillation by dissipation and continuous quantum repeaters. *Phys. Rev. Lett.* **107**, 120502 (2011).

[106] M. Zwerger, W. Dür, and H. J. Briegel. Measurement-based quantum repeaters. *Phys. Rev. A* **85**, 062326 Jun (2012).

[107] L. Childress, J. M. Taylor, A. S. Sørensen, and M. D. Lukin. Fault-tolerant quantum communication based on solid-state photon emitters. *Phys. Rev. Lett.* **96**, 070504 Feb (2006).

[108] D. C. Burnham and D. L. Weinberg. Observation of simultaneity in parametric production of optical photon pairs. *Phys. Rev. Lett.* **25**, 84 (1970).

[109] C. K. Hong and L. Mandel. Theory of parametric frequency down conversion of light. *Phys. Rev. A* **31**, 2409–2418 (1985).

[110] L. A. Wu, H. J. Kimble, J. L. Hall, and H. F. Wu. Generation of squeezed states by parametric down conversion. *Phys. Rev. Lett.* **57**, 2520–2523 (1986).

[111] A. Fedrizzi, R. Ursin, T. Herbst, M. Nespoli, R. Prevedel, T. Scheidl, F. Tiefenbacher, T. Jennewein, and A. Zeilinger. High-fidelity transmission of entanglement over a high-loss free-space channel. *Nature Physics* **5**, 389 (2009).

[112] N. Gisin, G. G. Ribordy, W. Tittel, and H. Zbinden. Quantum cryptography. *Rev. Mod. Phys.* **74**, 145–195 (2002).

[113] R. H. Hadfield. Single-photon detectors for optical quantum information applications. *Nature Photonics* **3**(12), 696–705 Dec (2009).

[114] N. Sangouard, C. Simon, H. de Riedmatten, and N. Gisin. Quantum repeaters based on atomic ensembles and linear optics. *Rev. Mod. Phys.* **83**, 33–80 (2011).

[115] A. Kuzmich, W. P. Bowen, A. D. Boozer, A. Boca, C. W. Chou, L. M. Duan, and H. J. Kimble. Generation of nonclassical photon pairs for scalable quantum communication with atomic ensembles. *Nature* **423**, 731–734 Jun 12 (2003).

[116] C. H. van der Wal, M. D. Eisaman, A. Andre, R. L. Walsworth, D. F. Phillips, A. S. Zibrov, and M. D. Lukin. Atomic memory for correlated photon states. *Science* **301**, 196–200 (2003).

[117] Z.-S. Yuan, Y.-A. Chen, B. Zhao, S. Chen, J. Schmiedmayer, and J.-W. Pan. Experimental demonstration of a bdcz quantum repeater node. *Nature* **454**, 1098–1101 Aug 28 (2008).

[118] C.-W. Chou, J. Laurat, H. Deng, K. S. Choi, H. de Riedmatten, D. Felinto, and H. J. Kimble. Functional quantum nodes for entanglement distribution over scalable quantum networks. *Science* **316**, 1316–1320 (2007).

[119] C. Simon, M. Afzelius, J. Appel, A. Boyer de la Giroday, S. J. Dewhurst, N. Gisin, C. Y. Hu, F. Jelezko, S. Kroll, J. H. Muller, J. Nunn, E. S. Polzik, J. G. Rarity, H. De Riedmatten, W. Rosenfeld, A. J. Shields, N. Skold,

R. M. Stevenson, R. Thew, I. A. Walmsley, M. C. Weber, H. Weinfurter, J. Wrachtrup, and R. J. Young. Quantum memories. *The European Physical Journal D* **58**, 1–22 (2010).

[120] A. E. Kozhekin, K. Molmer, and E. Polzik. Quantum memory for light. *Phys. Rev. A* **62**, 033809 (2000).

[121] A. V. Gorshkov, A. Andre, M. Fleischhauer, A. S. Sorensen, and M. D. Lukin. Universal approach to optimal photon storage in atomic media. *Phys. Rev. Lett.* **98**, 123601 (2007).

[122] J. Nunn, I. A. Walmsley, M. G. Raymer, K. Surmacz, F. C. Waldermann, Z. Wang, and D. Jaksch. Mapping broadband single-photon wave packets into an atomic memory. *Phys. Rev. A* **75**, 011401 (2007).

[123] K. F. Reim, J. Nunn, V. O. Lorenz, B. J. Sussman, K. C. Lee, N. K. Langford, D. Jaksch, and I. A. Walmsley. Towards high-speed optical quantum memories. *Nature Photonics* **4**, 218–221 (2010).

[124] K. C. Lee, M. R. Sprague, B. J. Sussman, J. Nunn, N. K. Langford, X.-M. Jin, T. Champion, P. Michelberger, K. F. Reim, D. England, D. Jaksch, and I. A. Walmsley. Entangling macroscopic diamonds at room temperature. *Science* **334**(6060), 1253–1256 (2011).

[125] M. Fleischhauer and M. D. Lukin. Dark-state polaritons in electromagnetically induced transparency. *Phys. Rev. Lett.* **84**, 5094–5097 (2000).

[126] M. Fleischhauer, A. Imamoglu, and J. P. Marangos. Electromagnetically induced transparency: Optics in coherent media. *Rev. Mod. Phys.* **77**, 633–673 (2005).

[127] M. D. Eisaman, A. Andre, F. Massou, M. Fleischhauer, A. S. Zibrov, and M. D. Lukin. Electromagnetically induced transparency with tunable single-photon

pulses. *Nature* **438**, 837–841 Dec 8 (2005).

[128] A. L. Alexander, J. J. Longdell, M. J. Sellars, and N. B. Manson. Photon echoes produced by switching electric fields. *Phys. Rev. Lett.* **96**, 043602 Feb (2006).

[129] W. Tittel, M. Afzelius, T. Chaneliere, R. L. Cone, S. Kroll, S. A. Moiseev, and M. Sellars. Photon-echo quantum memory in solid state systems. *Laser & Photonics Reviews* **4**, 244–267 (2010).

[130] S. A. Moiseev and S. Kröll. Complete reconstruction of the quantum state of a single-photon wave packet absorbed by a doppler-broadened transition. *Phys. Rev. Lett.* **87**, 173601 Oct (2001).

[131] B. Kraus, W. Tittel, N. Gisin, M. Nilsson, S. Kröll, and J. I. Cirac. Quantum memory for nonstationary light fields based on controlled reversible inhomogeneous broadening. *Phys. Rev. A* **73**, 020302 Feb (2006).

[132] M. Nilsson and S. Kroll. Solid state quantum memory using complete absorption and re-emission of photons by tailored and externally controlled inhomogeneous absorption profiles. *Optics Communications* **247**, 393–403 (2005).

[133] A. L. Alexander, J. J. Longdell, M. J. Sellars, and N. B. Manson. Coherent information storage with photon echoes produced by switching electric fields. *Journal of Luminescence* **127**, 94–97 (2007).

[134] M. Afzelius, C. Simon, H. de Riedmatten, and N. Gisin. Multimode quantum memory based on atomic frequency combs. *Phys. Rev. A* **79**, 052329 (2009).

[135] D. L. Moehring, P. Maunz, S. Olmschenk, K. C. Younge, D. N. Matsukevich, L. M. Duan, and C. Monroe. Entanglement of single-atom quantum bits at a distance. *Nature* **449**, 68 Sep 6 (2007).

[136] N. Mizuochi, P. Neumann, F. Rempp, J. Beck, V. Jacques, P. Siyushev, K. Nakamura, D. J. Twitchen, H. Watanabe, S. Yamasaki, F. Jelezko, and J. Wrachtrup. Coherence of single spins coupled to a nuclear spin bath of varying density. *Phys. Rev. B* **80**, 041201 Jul (2009).

[137] P. Cappellaro, L. Jiang, J. S. Hodges, and M. D. Lukin. Coherence and control of quantum registers based on electronic spin in a nuclear spin bath. *Phys. Rev. Lett.* **102**, 210502 May (2009).

[138] M. Kroutvar, Y. Ducommun, D. Heiss, M. Bichler, D. Schuh, G. Abstreiter, and J. J. Finley. Optically programmable electron spin memory using semiconductor quantum dots. *Nature* **432**, 81–84 Nov 4 (2004).

[139] N. Sangouard, R. Dubessy, and C. Simon. Quantum repeaters based on single trapped ions. *Phys. Rev. A* **79**, 042340 (2009).

[140] T. Wilk, S. C. Webster, A. Kuhn, and G. Rempe. Single-atom single-photon quantum interface. *Science* **317**, 488–490 (2007).

[141] B. Weber, H. P. Specht, T. Müller, J. Bochmann, M. Mücke, D. L. Moehring, and G. Rempe. Photon-photon entanglement with a single trapped atom. *Phys. Rev. Lett.* **102**, 030501 Jan (2009).

[142] E. Knill and R. Laflamme. Concatenated quantum codes. *arXiv:9608012 [quant-ph]* (1996).

[143] R. Raussendorf, S. Bravyi, and J. Harrington. Long-range quantum entanglement in noisy cluster states. *Phys. Rev. A* **71**, 062313 (2005).

[144] E. W. Dijkstra. A note on two problems in connexion with graphs. *Numer. Math.* **1**, 269–271 (1959).

[145] C. Di Franco and D. Ballester. Optimal path for a quantum teleportation protocol in entangled networks. *Phys. Rev. A* **85**, 010303 Jan (2012).

[146] M. Cuquet and J. Calsamiglia. Limited-path-length entanglement percolation in quantum complex networks. *Phys. Rev. A* **83**, 032319 Mar (2011).

[147] D. P. DiVincenzo, C. A. Fuchs, H. Mabuchi, J. A. Smolin, A. Thapliyal, and A. Uhlmann. Entanglement of assistance. *arXiv:9803033 [quant-ph]* (1998).

[148] E. Jané. Purification of two-qubit mixed states. *Quant. Inf. Comp.* **2**, 348 (2002).

[149] A. Kent. Entangled mixed states and local purification. *Phys. Rev. Lett.* **81**, 2839 (1998).

[150] M. Horodecki, J. Oppenheim, and A. Winter. Partial quantum information. *Nature* **436**, 673–676 Aug 4 (2005).

[151] M. Lewenstein and A. Sanpera. Separability and entanglement of composite quantum systems. *Phys. Rev. Lett.* **80**, 2261–2264 Mar (1998).

[152] L. Wu and S. Q. Zhu. Entanglement percolation on a quantum internet with scale-free and clustering characters. *Phys. Rev. A* **84**, 052304 (2011).

[153] C. D. Lorenz and R. M. Ziff. Precise determination of the bond percolation thresholds and finite-size scaling corrections for the sc, fcc, and bcc lattices. *Phys. Rev. E* **57**, 230 (1998).

[154] P. X. Chen, L. M. Liang, C. Z. Li, and M. Q. Huang. Necessary and sufficient condition for distillability with unit fidelity from finite copies of a mixed state: The most efficient purification protocol. *Phys. Rev. A* **66**, 022309 (2002).

[155] P. E. Hart, N. J. Nilsson, and B. Raphael. A formal basis for the heuristic determination of minimum cost paths. *IEEE Trans. Syst. Sci. Cybern.* **4**(2), 100–107 (1968).

[156] H. J. Herrmann, D. C. Hong, and H. E. Stanley. Backbone and elastic backbone of percolation clusters obtained by the new method of 'burning'. *J. Phys. A* **17**, L261 (1984).

[157] J. Edmonds. Paths trees and flowers. *Canadian Journal of Mathematics* **17**(3), 449 (1965).

[158] P. W. Shor. Scheme for reducing decoherence in quantum computer memory. *Phys. Rev. A* **52**(4), R2493–R2496 (1995).

[159] S. Kirkpatrick. Percolation and conduction. *Rev. Mod. Phys.* **45**(4), 574–588 Oct (1973).

[160] H. L. Frisch, J. M. Hammersley, and D. J. A. Welsh. Monte carlo estimates of percolation probabilities for various lattices. *Phys. Rev.* **126**(3), 949–951 May (1962).

[161] N. L. Biggs, E. K. Lloyd, and R. J. Wilson. *Graph Theory, 1736-1936*. Oxford University Press, (1976).

[162] J.-C. Charlier, X. Blase, and S. Roche. Electronic and transport properties of nanotubes. *Rev. Mod. Phys.* **79**(2), 677–732 May (2007).

[163] T. Ando. Theory of electronic states and transport in carbon nanotubes. *Journal of the Physical Society of Japan* **74**(3), 777–817 (2005).

[164] R. Saito, G. Dresselhaus, and M.S. Dresselhaus. *Physical properties of carbon nanotubes*. Imperial College Press, (1998).

[165] X. Wang, Q. Li, J. Xie, Z. Jin, J. Wang, Y. Li, K. Jiang, and S. Fan. Fabrication of ultralong and electrically uniform single-walled carbon nanotubes on clean substrates. *Nano Letters* **9**(9), 3137–3141 (2009).

[166] C. T. White and T. N. Todorov. Carbon nanotubes as long ballistic conductors. *Nature* **393**(6682), 240–242 May 21 (1998).

[167] J. Klinovaja, M. J. Schmidt, B. Braunecker, and D. Loss. Helical modes in carbon nanotubes generated by strong electric fields. *Phys. Rev. Lett.* **106**(15), 156809 Apr (2011).

[168] Y.-H. Kim and K. J. Chang. Subband mixing rules in circumferentially perturbed carbon nanotubes: Effects of transverse electric fields. *Phys. Rev. B* **64**(15), 153404 Sep (2001).

[169] M. Pacheco, Z. Barticevic, C. G. Rocha, and A. Latge. Electric field effects on the energy spectrum of carbon nanotubes. *Journal of Physics: Condensed Matter* **17**(37), 5839 (2005).

[170] I. Takesue, J. Haruyama, N. Kobayashi, S. Chiashi, S. Maruyama, T. Sugai, and H. Shinohara. Superconductivity in entirely end-bonded multiwalled carbon nanotubes. *Phys. Rev. Lett.* **96**(5), 057001 Feb (2006).

[171] J. Noffsinger and M. L. Cohen. Electron-phonon coupling and superconductivity in double-walled carbon nanotubes. *Phys. Rev. B* **83**(16), 165420 Apr (2011).

[172] A. Y. Kasumov, R. Deblock, M. Kociak, B. Reulet, H. Bouchiat, I. I. Khodos, Yu. B. Gorbatov, V. T. Volkov, C. Journet, and M. Burghard. Supercurrents through single-walled carbon nanotubes. *Science* **284**(5419), 1508–1511 (1999).

[173] A. F. Morpurgo, J. Kong, C. M. Marcus, and H. Dai. Gate-controlled superconducting proximity effect in carbon nanotubes. *Science* **286**(5438), 263–265 (1999).

[174] K. Uchida and S. Okada. Electronic properties of a carbon nanotube in a field-effect transistor structure: A first-principles study. *Phys. Rev. B* **79**(8), 085402 Feb (2009).

[175] E. S. Snow, F. K. Perkins, E. J. Houser, S. C. Badescu, and T. L. Reinecke. Chemical detection with a single-walled carbon nanotube capacitor. *Science* **307**(5717), 1942–1945 (2005).

[176] X. Tang, S. Bansaruntip, N. Nakayama, E. Yenilmez, Y.-l. Chang, and Q. Wang. Carbon nanotube dna sensor and sensing mechanism. *Nano Letters* **6**(8), 1632–1636 (2006).

[177] M. Freitag, Y. Martin, J. A. Misewich, R. Martel, and P. Avouris. Photoconductivity of single carbon nanotubes. *Nano Letters* **3**(8), 1067–1071 (2003).

[178] C. D. Spataru, S. Ismail-Beigi, L. X. Benedict, and S. G. Louie. Excitonic effects and optical spectra of single-walled carbon nanotubes. *Phys. Rev. Lett.* **92**(7), 077402 Feb (2004).

[179] J. Jiang, R. Saito, A. Grneis, G. Dresselhaus, and M.S. Dresselhaus. Optical absorption matrix elements in single-wall carbon nanotubes. *Carbon* **42**(15), 3169 – 3176 (2004).

[180] S. Motavas, A. Ivanov, and A. Nojeh. Optical transitions in semiconducting zigzag carbon nanotubes with small diameters: A first-principles broad-range study. *Phys. Rev. B* **82**(8), 085442 Aug (2010).

[181] A. Zarifi and T. G. Pedersen. Universal analytic expression of electric-dipole matrix elements for carbon nanotubes. *Phys. Rev. B* **80**(19), 195422 Nov (2009).

[182] S. V. Goupalov, A. Zarifi, and T. G. Pedersen. Calculation of optical matrix elements in carbon nanotubes. *Phys. Rev. B* **81**(15), 153402 Apr (2010).

[183] S. V. Goupalov. Optical transitions in carbon nanotubes. *Phys. Rev. B* **72**(19), 195403 Nov (2005).

[184] S. Berciaud, C. Voisin, H. Yan, B. Chandra, R. Caldwell, Y. Shan, L. E. Brus, J. Hone, and T. F. Heinz. Excitons and high-order optical transitions in individual carbon nanotubes: A rayleigh scattering spectroscopy study. *Phys. Rev. B* **81**(4), 041414 Jan (2010).

[185] Y. Takagi and S. Okada. Theoretical calculation for the ultraviolet optical properties of single-walled carbon nanotubes. *Phys. Rev. B* **79**(23), 233406 Jun (2009).

[186] A. Zarifi and T. G. Pedersen. Analytic approach to the linear susceptibility of zigzag carbon nanotubes. *Phys. Rev. B* **74**(15), 155434 Oct (2006).

[187] E. Malić, M. Hirtschulz, F. Milde, A. Knorr, and S. Reich. Analytical approach to optical absorption in carbon nanotubes. *Phys. Rev. B* **74**(19), 195431 Nov (2006).

[188] R. Saito, A. Gruneis, Ge. G. Samsonidze, G. Dresselhaus, M. S. Dresselhaus, A. Jorio, L. G. Cancado, M. A. Pimenta, and A. G. Souza. Optical absorption of graphite and single-wall carbon nanotubes. *Applied Physics A - Materials Science & Processing* **78**(8), 1099–1105 May (2004).

[189] Y. Miyauchi, H. Hirori, K. Matsuda, and Y. Kanemitsu. Radiative lifetimes and coherence lengths of one-dimensional excitons in single-walled carbon nanotubes. *Phys. Rev. B* **80**(8), 081410 Aug (2009).

[190] S. Roche, J. Jiang, F. Triozon, and R. Saito. Quantum dephasing in carbon nanotubes due to electron-phonon coupling. *Phys. Rev. Lett.* **95**(7), 076803 Aug (2005).

[191] S. J. Tans, M. H. Devoret, H. J. Dai, A. Thess, R. E. Smalley, L. J. Geerligs, and C. Dekker. Individual single-wall carbon nanotubes as quantum wires. *Nature* **386**(6624), 474–477 Apr 3 (1997).

[192] S. Roche, J. Jiang, F. Triozon, and R. Saito. Conductance and coherence lengths in disordered carbon nanotubes: Role of lattice defects and phonon vibrations. *Phys. Rev. B* **72**(11), 113410 Sep (2005).

[193] V. Perebeinos, J. Tersoff, and P. Avouris. Electron-phonon interaction and transport in semiconducting carbon nanotubes. *Phys. Rev. Lett.* **94**(8), 086802 Mar (2005).

[194] J. Bures and R. Ghosh. Power density of the evanescent field in the vicinity of a tapered fiber. *J. Opt. Soc. Am. A* **16**(8), 1992–1996 Aug (1999).

[195] F. Le Kien, S. D. Gupta, K. P. Nayak, and K. Hakuta. Nanofiber-mediated radiative transfer between two distant atoms. *Phys. Rev. A* **72**(6), 063815 Dec (2005).

[196] G. Sagué, E. Vetsch, W. Alt, D. Meschede, and A. Rauschenbeutel. Cold-atom physics using ultrathin optical fibers: Light-induced dipole forces and surface interactions. *Phys. Rev. Lett.* **99**, 163602 Oct (2007).

[197] E. Vetsch, D. Reitz, G. Sagué, R. Schmidt, S. T. Dawkins, and A. Rauschenbeutel. Optical interface created by laser-cooled atoms trapped in the evanescent field surrounding an optical nanofiber. *Phys. Rev. Lett.* **104**(20), 203603 May (2010).

[198] A. Liao, Y. Zhao, and E. Pop. Avalanche-induced current enhancement in semiconducting carbon nanotubes. *Phys. Rev. Lett.* **101**(25), 256804 Dec (2008).

[199] M. S. Dresselhaus, G. Dresselhaus, R. Saito, and A. Jorio. Exciton photophysics of carbon nanotubes. *Annual Review of Physical Chemistry* **58**(1), 719–747 (2007).

[200] J. E. Bunder and J. M. Hill. Zigzag carbon nanotubes with generic electron-electron interactions. *Phys. Rev. B* **80**(15), 153406 Oct (2009).

[201] A. D. Mohite, P. Gopinath, H. M. Shah, and B. W. Alphenaar. Exciton dissociation and stark effect in the carbon nanotube photocurrent spectrum. *Nano Letters* **8**(1), 142–146 (2008).

[202] M. Ichida, S. Mizuno, Y. Tani, Y. Saito, and A. Nakamura. Exciton effects of optical transitions in single-wall carbon nanotubes. *Journal of the Physical Society of Japan* **68**(10), 3131–3133 (1999).

[203] D. S. L. Abergel, V. Apalkov, J. Berashevich, K. Ziegler, and T. Chakraborty. Properties of graphene: a theoretical perspective. *Advances in Physics* **59**(4), 261–482 (2010).

[204] A. Grüneis, R. Saito, Ge. G. Samsonidze, T. Kimura, M. A. Pimenta, A. Jorio, A. G. Souza Filho, G. Dresselhaus, and M. S. Dresselhaus. Inhomogeneous optical absorption around the k point in graphite and carbon nanotubes. *Phys. Rev. B* **67**(16), 165402 Apr (2003).

[205] R. Saito, G. Dresselhaus, and M. S. Dresselhaus. Trigonal warping effect of carbon nanotubes. *Phys. Rev. B* **61**(4), 2981–2990 Jan (2000).

[206] A. V. Nikolaev, A. V. Bibikov, A. V. Avdeenkov, I. V. Bodrenko, and E. V. Tkalya. Electronic and transport properties of rectangular graphene macromolecules and zigzag carbon nanotubes of finite length. *Phys. Rev. B* **79**(4), 045418 Jan (2009).

[207] K. J. Blow, R. Loudon, S. J. D. Phoenix, and T. J. Shepherd. Continuum fields in quantum optics. *Phys. Rev. A* **42**(7), 4102–4114 Oct (1990).

[208] S. Tasaki, K. Maekawa, and T. Yamabe. π-band contribution to the optical properties of carbon nanotubes: Effects of chirality. *Phys. Rev. B* **57**(15),

9301–9318 Apr (1998).

[209] H. Ajiki and T. Ando. Aharonov-bohm effect in carbon nanotubes. *Physica B: Condensed Matter* **201**, 349 – 352 (1994).

[210] M. F. Islam, D. E. Milkie, C. L. Kane, A. G. Yodh, and J. M. Kikkawa. Direct measurement of the polarized optical absorption cross section of single-wall carbon nanotubes. *Phys. Rev. Lett.* **93**(3), 037404 Jul (2004).

[211] J-S. Lauret, C. Voisin, G. Cassabois, C. Delalande, P. Roussignol, O. Jost, and L. Capes. Ultrafast carrier dynamics in single-wall carbon nanotubes. *Phys. Rev. Lett.* **90**(5), 057404 Feb (2003).

[212] M. F. Lin. Optical spectra of single-wall carbon nanotube bundles. *Phys. Rev. B* **62**(19), 13153–13159 Nov (2000).

[213] L. M. Tong, R. R. Gattass, J. B. Ashcom, S. L. He, J. Y. Lou, M. Y. Shen, I. Maxwell, and E. Mazur. Subwavelength-diameter silica wires for low-loss optical wave guiding. *Nature* **426**(6968), 816–819 Dec 18 (2003).

[214] L. Tong and E. Mazur. Glass nanofibers for micro- and nano-scale photonic devices. *Journal of Non-Crystalline Solids* **354**(12-13), 1240 – 1244 (2008). Proceedings of the 2005 International Conference on Glass - In conjunction with the Annual Meeting of the International Commission on Glass.

[215] G. Brambilla, V. Finazzi, and D. Richardson. Ultra-low-loss optical fiber nanotapers. *Opt. Express* **12**(10), 2258–2263 May (2004).

[216] L. Tong. Brief introduction to optical microfibers and nanofibers. *Frontiers of Optoelectronics in China* **3**, 54–60 (2010).

[217] L. M. Tong, J. Y. Lou, and E. Mazur. Single-mode guiding properties of subwavelength-diameter silica and silicon wire waveguides. *Opt. Express* **12**(6), 1025–1035 MAR 22 (2004).

[218] A. W. Snyder and W. R. Young. Modes of optical waveguides. *J. Opt. Soc. Am.* **68**(3), 297–309 Mar (1978).

[219] A. W. Snyder and J. D. Love. *Optical waveguide theory.* Science paperbacks. Chapman and Hall, (1983).

[220] J. S. Soares and A. Jorio. Study of carbon nanotube-substrate interaction. *Journal of Nanotechnology* **2012**, 512738 (2012).

[221] S. Berciaud, L. Cognet, and B. Lounis. Luminescence decay and the absorption cross section of individual single-walled carbon nanotubes. *Phys. Rev. Lett.* **101**(7), 077402 Aug (2008).

[222] P. Koskinen. Electronic and optical properties of carbon nanotubes under pure bending. *Phys. Rev. B* **82**(19), 193409 Nov (2010).

[223] A. M. Clohessy, N. Healy, D. F. Murphy, and C. D. Hussey. Short low-loss nanowire tapers on singlemode fibres. *Electronics Letters* **41**(17), 954 – 955 Aug (2005).

[224] L. Ding, A. Tselev, J. Wang, D. Yuan, H. Chu, T. P. McNicholas, Y. Li, and J. Liu. Selective growth of well-aligned semiconducting single-walled carbon nanotubes. *Nano Letters* **9**(2), 800–805 (2009). PMID: 19159186.

[225] C. Wang, K. Ryu, L. De Arco, A. Badmaev, J. Zhang, X. Lin, Y. Che, and C. Zhou. Synthesis and device applications of high-density aligned carbon nanotubes using low-pressure chemical vapor deposition and stacked multiple transfer. *Nano Research* **3**, 831–842 (2010).

[226] B. K. Sarker, S. Shekhar, and S. I. Khondaker. Semiconducting enriched carbon nanotube aligned arrays of tunable density and their electrical transport properties. *ACS Nano* **5**(8), 6297–6305 (2011).

[227] S. W. Hong, T. Banks, and J. A. Rogers. Improved density in aligned arrays of single-walled carbon nanotubes by sequential chemical vapor deposition on quartz. *Advanced Materials* **22**(16), 1826–1830 (2010).

[228] S. Shekhar, P. Stokes, and S. I. Khondaker. Ultrahigh density alignment of carbon nanotube arrays by dielectrophoresis. *ACS Nano* **5**(3), 1739–1746 (2011).

[229] H. Wang, J. Luo, F. Schäffel, M. H. Rümmeli, G. A. D. Briggs, and J. H. Warner. Carbon nanotube nanoelectronic devices compatible with transmission electron microscopy. *Nanotechnology* **22**(24), 245305 (2011).

[230] Y.-Q. Xu, E. Flor, M. J. Kim, B. Hamadani, H. Schmidt, R. E. Smalley, and R. H. Hauge. Vertical array growth of small diameter single-walled carbon nanotubes. *Journal of the American Chemical Society* **128**(20), 6560–6561 (2006).

[231] M. G. Hahm, Y.-K. Kwon, E. Lee, C. W. Ahn, and Y. J. Jung. Diameter selective growth of vertically aligned single walled carbon nanotubes and study on their growth mechanism. *The Journal of Physical Chemistry C* **112**(44), 17143–17147 (2008).

[232] P. Li and J. Zhang. Sorting out semiconducting single-walled carbon nanotube arrays by preferential destruction of metallic tubes using water. *J. Mater. Chem.* **21**, 11815–11821 (2011).

[233] L. Qu, F. Du, and L. Dai. Preferential syntheses of semiconducting vertically aligned single-walled carbon nanotubes for direct use in fets. *Nano Letters* **8**(9), 2682–2687 (2008). PMID: 18665651.

[234] P. G. Collins, M. S. Arnold, and P. Avouris. Engineering carbon nanotubes and nanotube circuits using electrical breakdown. *Science* **292**(5517), 706–709 (2001).

[235] G. F. Zhong, T. Iwasaki, and H. Kawarada. Semi-quantitative study on the fabrication of densely packed and vertically aligned single-walled carbon nanotubes. *Carbon* **44**(10), 2009 – 2014 (2006).

[236] Y. Murakami, S. Chiashi, Y. Miyauchi, M. Hu, M. Ogura, T. Okubo, and S. Maruyama. Growth of vertically aligned single-walled carbon nanotube films on quartz substrates and their optical anisotropy. *Chemical Physics Letters* **385**(3-4), 298 – 303 (2004).

[237] S. Esconjauregui, M. Fouquet, B. C. Bayer, C. Ducati, R. Smajda, S. Hofmann, and J. Robertson. Growth of ultrahigh density vertically aligned carbon nanotube forests for interconnects. *ACS Nano* **4**(12), 7431–7436 (2010).

[238] I. Ibrahim, A. Bachmatiuk, F. Börrnert, J. Blüher, U. Wolff, J. H. Warner, B. Büchner, G. Cuniberti, and M. H. Rümmeli. Optimizing substrate surface and catalyst conditions for high yield chemical vapor deposition grown epitaxially aligned single-walled carbon nanotubes. *Carbon* **49**(15), 5029 – 5037 (2011).

[239] F. Wang, G. Dukovic, L. E. Brus, and T. F. Heinz. Time-resolved fluorescence of carbon nanotubes and its implication for radiative lifetimes. *Phys. Rev. Lett.* **92**(17), 177401 Apr (2004).

[240] C. Galland and A. Imamoğlu. All-optical manipulation of electron spins in carbon-nanotube quantum dots. *Phys. Rev. Lett.* **101**(15), 157404 Oct (2008).

[241] F. Kuemmeth, H. O. H. Churchill, P. K. Herring, and C. M. Marcus. Carbon nanotubes for coherent spintronics. *Materials Today* **13**(3), 18–26 Mar (2010).

[242] S. Perseguers. Fidelity threshold for long-range entanglement in quantum networks. *Phys. Rev. A* **81**(1), 012310 Jan (2010).

[243] Y. Li, D. Cavalcanti, and L. C. Kwek. Long-distance entanglement generation with scalable and robust two-dimensional quantum network. *Phys. Rev. A* **85**, 062330 Jun (2012).

[244] A. M. Stephens, A. G. Fowler, and L. C. L. Hollenberg. Universal fault tolerant quantum computation on bilinear nearest neighbor arrays. *Quant. Inf. Comp.* **8**(3), 330–344 March (2008).

[245] A. Grudka, M. Horodecki, P. Horodecki, P. Mazurek, L. Pankowski, and A. Przysiezna. Long distance quantum communication over noisy networks. *arXiv:1202.1016 [quant-ph]* (2012).

[246] S. Perseguers, G. J. Lapeyre, D. Cavalcanti, M. Lewenstein, and A. Acin. Distribution of entanglement in quantum networks. arXiv:quant-ph/1209.5303, (2012).

[247] A. Sanpera, R. Tarrach, and G. Vidal. Local description of quantum inseparability. *Phys. Rev. A* **58**(2), 826–830 (1998).

[248] A. Acin, A. Andrianov, L. Costa, E. Jane, J. I. Latorre, and R. Tarrach. Generalized schmidt decomposition and classification of three-quantum-bit states. *Phys. Rev. Lett.* **85**(7), 1560–1563 (2000).

[249] W. Dur, G. Vidal, and J. I. Cirac. Three qubits can be entangled in two inequivalent ways. *Phys. Rev. A* **62**(6), 062314 (2000).

[250] A. Acin, A. Andrianov, E. Jane, and R. Tarrach. Three-qubit pure-state canonical forms. *J. Phys. A* **34**(35), 6725–6739 (2001).